Cancer Cell

Article

Identification of cycling regulatory T cell precursors as conductors of immune escape during breast carcinoma progression

Graphical abstract

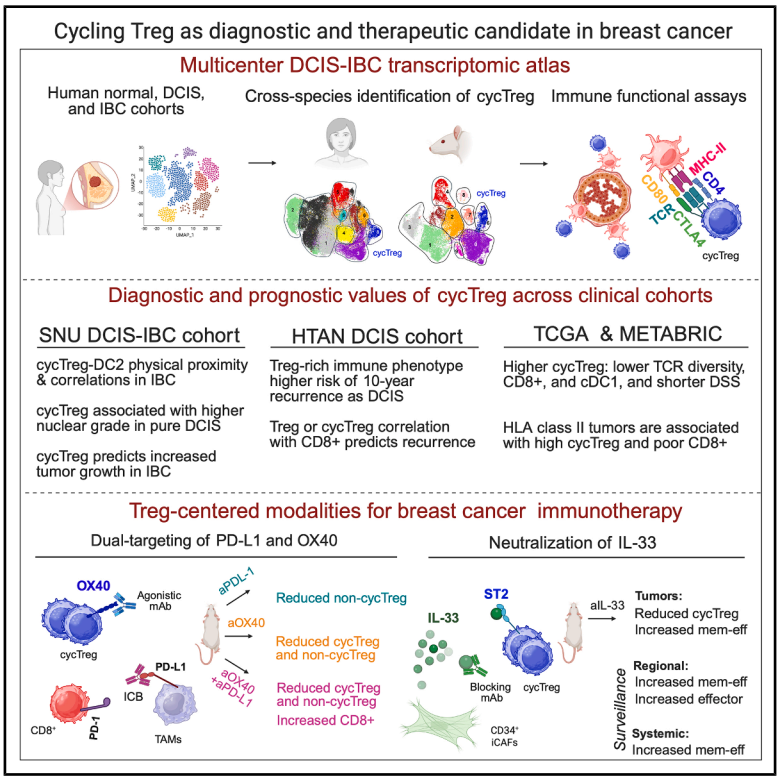

Highlights

- Single-cell transcriptomic landscape of breast *in situ*-to-invasive carcinoma transition
- Cycling Treg accumulation driven by type 2 dendritic cells drives immune suppression
- Rat model of breast cancer reproduces immune evasive mechanisms
- OX40 and IL-33 as therapeutic targets to enhance anti-tumor immunosurveillance

Authors

Triet Minh Bui, Ernesto Rojas Jimenez, Zheqi Li, ..., E. Shelley Hwang, Simona Cristea, Kornelia Polyak

Correspondence

kornelia_polyak@dfci.harvard.edu

In brief

Bui et al. map immune escape from DCIS to IBC by using single-cell transcriptomic profiling of large clinical cohorts, identifying cycTreg as key IL-33-driven immune suppressors supported by heightened MHC class II presentation from cDC2. A rat model recapitulating human disease confirms the functional relevance of these pathways during breast cancer progression.

Bui et al., 2026, Cancer Cell *44*, 1–22
June 8, 2026
https://doi.org/10.1016/j.ccell.2026.03.015

CellPress

Cancer Cell

CellPress
OPEN ACCESS

Article

Identification of cycling regulatory T cell precursors as conductors of immune escape during breast carcinoma progression

Triet Minh Bui,[1,2,3] Ernesto Rojas Jimenez,[1,2,3] Zheqi Li,[1,2,3] Pierre Foidart,[1,2,3] Julieann Puleo,[1,2,3] Pengze Yan,[1,2,3] Aashna Jhaveri,[4,5] Lin Yang,[4,5] Jun Nishida,[1,2,3] Marco Seehawer,[1,2,3] Xinran Cai,[1,2,3] Kimberly Ann Parker,[1,2,3] Xiaodi Qin,[6] Oyku Ece Sumer,[1] Xiao-Yun Huang,[1] Ashka Patel,[1,2] Deborah Dillon,[7] Charles H. McDonnell III,[8] Ron Rowberry,[8] Shinedeep Jhajj,[8] Catherine Baker,[8] Daniel D. Brown,[9] Siri H. Strand,[10] Jeffrey R. Marks,[11] Graham A. Colditz,[12] So Yeon Park,[13] Adrian V. Lee,[9,14] Michael Angelo,[10] Priscilla F. McAuliffe,[14] Kristie Bobolis,[8] Robert West,[10] Glenn Dranoff,[1] E. Shelley Hwang,[11] Simona Cristea,[4,5] and Kornelia Polyak[1,2,3,15,*]

[1]Department of Medical Oncology, Dana-Farber Cancer Institute, Boston, MA 02215, USA
[2]Department of Medicine, Brigham and Women's Hospital, Boston, MA 02115, USA
[3]Department of Medicine, Harvard Medical School, Boston, MA 02115, USA
[4]Department of Data Science, Dana-Farber Cancer Institute, Boston, MA 02215, USA
[5]Department of Biostatistics, Harvard T. H. Chan School of Public Health, Boston, MA 02115, USA
[6]Duke Cancer Institute, Duke University School of Medicine, Durham, NC 27705, USA
[7]Department of Pathology, Brigham and Women's Hospital, Boston, MA 02115, USA
[8]Sutter Institute for Medical Research, Roseville, CA 95661, USA
[9]Institute for Precision Medicine, University of Pittsburgh, Pittsburgh, PA 15260, USA
[10]Department of Pathology, Stanford University School of Medicine, Stanford, CA 94305, USA
[11]Department of Surgery, Duke University School of Medicine, Durham, NC 27708, USA
[12]Department of Surgery, Washington University School of Medicine, St. Louis, MO 63108, USA
[13]Department of Pathology, Seoul National University Bundang Hospital, Seongnam, Gyeonggi, Republic of Korea
[14]UPMC Hillman Cancer Center, Pittsburgh, PA 15213, USA
[15]Lead contact
*Correspondence: kornelia_polyak@dfci.harvard.edu
https://doi.org/10.1016/j.ccell.2026.03.015

SUMMARY

Immune escape during the ductal carcinoma *in situ* (DCIS)-to-invasive breast cancer (IBC) transition shapes tumor evolution. Through transcriptomic mapping of the immune landscapes of normal breast, DCIS, and IBC from large patient cohorts, we identified T and myeloid cells as the primary distinguishing features between DCIS and IBC. We discovered cycling regulatory T cells (cycTreg) as an orchestrator of immunosuppression in IBC. cycTreg frequency predicts cytotoxic CD8$^+$, TCR diversity, disease-specific survival in IBC, and recurrence in DCIS. In a rat model of breast cancer, we demonstrated that cycTreg act as precursors to mature Treg and are inducible by tumor-localized type 2 dendritic cells. Profiling of tumors subjected to αOX40 and αPD-L1 therapies revealed an IL-33-mediated fibroblast-cycTreg signaling loop, the disruption of which enhances intratumoral antigen-experienced CD8$^+$ effectors and systemic immunosurveillance. Our study defines cycTreg as critical inducers of immune escape and promising immuno-oncology targets in breast cancer.

INTRODUCTION

Ductal carcinoma *in situ* (DCIS) is a preinvasive tumor and a non-obligate precursor of invasive breast carcinoma (IBC).[1] We previously characterized the DCIS-to-IBC transition as an evolutionary bottleneck marked by immune escape, including reduced cytotoxic CD8$^+$ T cells and enhanced immunosuppression.[2,3] Nitroso-N-methylurea (NMU)-induced mammary tumors in outbred Sprague-Dawley (SD) rats recapitulate these features of human breast cancer (BC), and SD rats display heterogeneous response to αPD-L1 and TGF-β receptor inhibition.[4] Molecular diversity, immune dynamics, and therapeutic variability of SD rat tumors make this model a powerful platform for mechanistic studies of BC immunobiology.

Tumor-infiltrating T lymphocytes (TILs) are crucial determinants of immunotherapeutic sensitivity across solid tumors, including BC.[5,6] Their phenotypes vary widely across tumor subtypes, disease stages, and treatment contexts.[5,7] Hormone receptor-positive (HR$^+$) tumors are generally immune cold, whereas HER2-positive (HER2$^+$) and triple-negative BC (TNBC)

Please cite this article in press as: Bui et al., Identification of cycling regulatory T cell precursors as conductors of immune escape during breast carcinoma progression, Cancer Cell (2026), https://doi.org/10.1016/j.ccell.2026.03.015

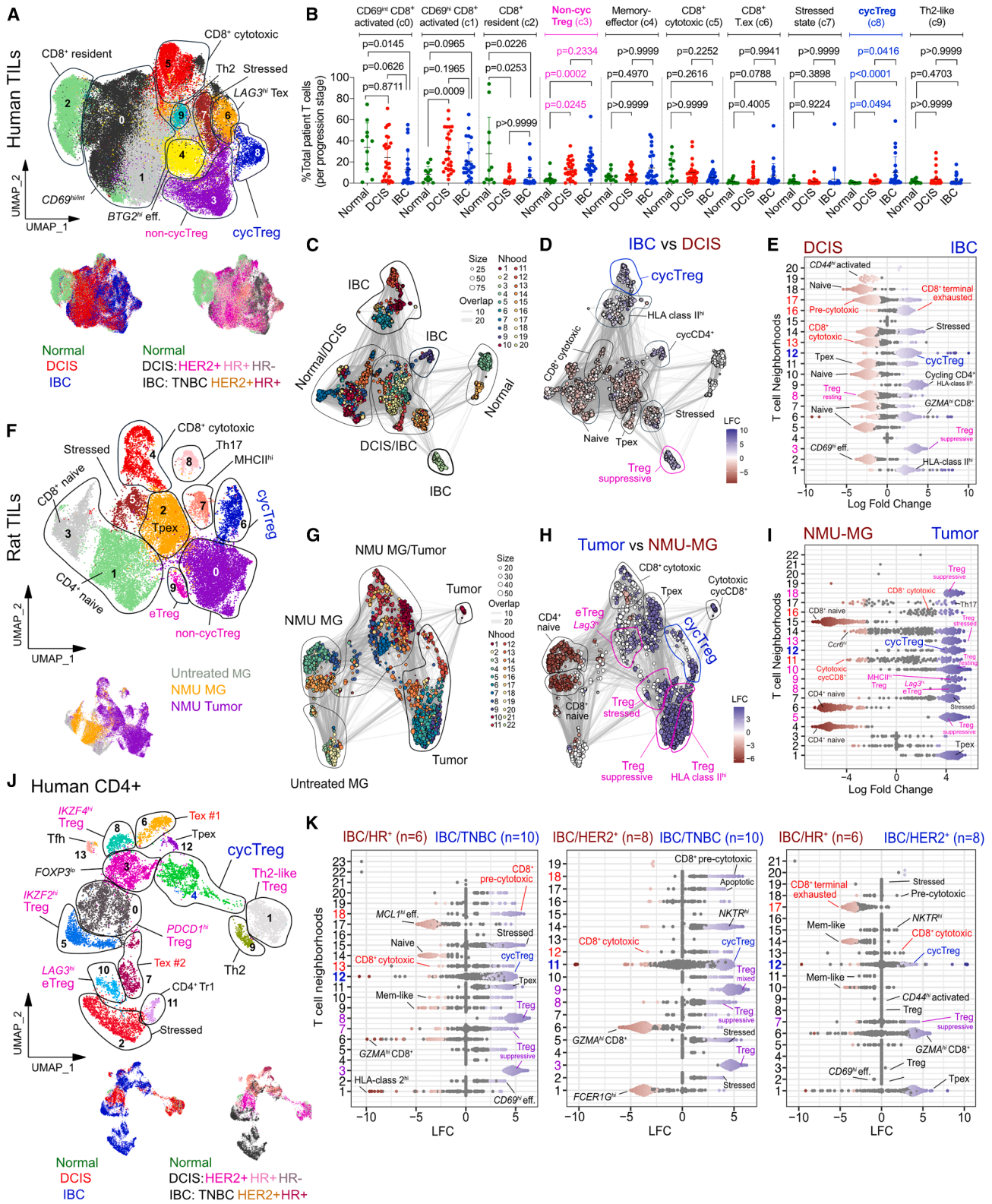

Figure 1. Single-cell transcriptomes of human and rat mammary tissues

(A) UMAP plots of human T cells (n = 64) showing stage- and subtype-specific grouping (insets).

(B) Quantification of T cell subsets (normal: n = 11; DCIS: n = 29; IBC: n = 24). Patients with <100 T cells were excluded. Unadjusted significance values were computed by Kruskal-Wallis test and Tukey's multiple comparison.

(legend continued on next page)

exhibits higher immune infiltration. However, whether TIL heterogeneity evolves directly during the DCIS-to-IBC transition, and which mechanisms shape the enrichment of specific TIL states at each disease stage remain unresolved.

We conducted single-cell transcriptomic profiling of a multicenter clinical dataset, spanning normal breast tissues, DCIS, and IBC. Comparative analyses with SD rats revealed highly diverse and stage-specific T cell states conserved across species. A previously unrecognized regulatory T cell (Treg) precursor termed cycling Treg (*FOXP3*^{int} *IKZF2/4*^{int} *MKI67*^{hi}, cycTreg) emerged in DCIS and drastically expanded in IBC. cycTreg abundance correlated positively with type 2 dendritic cells (cDC2) and with tumors exhibiting high human leukocyte antigen (HLA) class II expression. *Ex vivo* co-culture studies demonstrated that tumor-resident cDC2, but not cDC1 or peripheral monocyte-derived DCs (moDCs), robustly induced immune synapse-dependent cycTreg expansion, supporting a functional cDC2-cycTreg axis.

To assess therapeutic relevance, we tested cycTreg inhibitory strategies in SD rats. Dual targeting of PD-L1 and OX40 or single-agent αIL-33 markedly reduced cycTreg frequency and Treg heterogeneity, leading to tumor regression. These findings position cycTreg as a key orchestrator of BC immune escape, with potential diagnostic values for patient stratification, and as a promising immuno-oncology target in both DCIS and IBC.

RESULTS

Single-cell landscape of mammary tumor immune microenvironment (TIME) in human and rat tissues

A combination of single-cell and spatial transcriptomic analysis of human and rat mammary tissues revealed conserved cellular architectures across normal, preinvasive, and invasive cancer states. In patients, profiling of normal breast (n = 3), DCIS (n = 10), and invasive TNBC (n = 7) identified major immune, epithelial, endothelial cells (ECs), and other stromal lineages (Figure S1A and Table S1). Concurrent characterization of untreated (n = 3) and NMU-treated rat mammary glands (MGs, n = 3) and tumors (n = 7) demonstrated a highly similar TIME composed of T cells, B cells, myeloid cells, and diverse luminal epithelial states (Figure S1B, DEGs in Table S2). Spatial mapping showed that untreated rat MGs were enriched for myofibroblasts and luminal progenitors (LPs), whereas NMU-treated MGs developed DCIS-like microlesions marked by myoepithelial layer and TIL infiltration. Fully developed tumors contained immune niches populated by TILs and tumor-associated macrophages (TAMs), interspersed with luminal cancer regions and cancer-associated fibroblasts (CAFs) (Table S3).

A longitudinal study in the NMU model demonstrated that DCIS-like microlesions arise early and persist through tumor evolution. Microlesions were present at nearly all time points, from 2 to 14 weeks post-NMU, while macroscopic tumors appeared between weeks 6 and 10 (Figure S1C). Both lesion types consistently retained an intact αSMA$^+$ myoepithelium, closely mirroring human DCIS architecture (Figure S1D). scRNA-seq profiling from early to late stages revealed that macroscopic tumors shifted from LP-like toward more differentiated epithelial phenotypes (Figure S1E).

To build a comprehensive DCIS-IBC atlas, scRNA-seq datasets from the HTAN-DFCI cohort were integrated with three published datasets,[8–10] yielding 348,988 high-quality cells from 72 patients of normal tissues (n = 11), DCIS (n = 30), and IBC (n = 31) across HR$^+$, HER2$^+$, and TNBC subtypes (Figure S1F). Unsupervised clustering identified 15 major immune, epithelial, and stromal lineages, each distinctly segregating progression stage and BC molecular subtypes. Across both species, T cells emerged as the most abundant immune population (Figures S1B and S1F).

T cell heterogeneity and a cycling Treg state in BC TIMEs

T cells were the most abundant immune lineage across human breast tissues, yet their frequencies and phenotypic compositions varied markedly by the progression stage and tumor subtype (Figure S1G). Besides 8 cases with minimal TIL presence, most DCIS and IBC samples exhibited moderate-to-high TIL abundance. Louvain re-clustering resolved 10 transcriptionally distinct T cell states that segregated normal from malignant tissues and further stratified tumor subtypes (Figure 1A). Normal breast was enriched for CD8$^+$ tissue-resident T cells, which were considerably diminished in DCIS and IBC. Tumors instead contained diverse activated and dysfunctional states, including effector, Th2-like, cytotoxic CD8$^+$, exhausted (Tex), and stressed T cells[11] (Figure 1B). A mature FOXP3$^+$ Treg cluster was significantly expanded in tumors relative to normal tissue. Notably, a proliferative "cycling" Treg population (cycTreg: *FOXP3*^{int}, *MKI67*^{hi}, and *IKZF2/4*^{hi}) was absent in normal breast, present at low levels in DCIS, and strongly enriched in IBC (~4%–55% TILs, Figure 1B).

Because discrete clustering may obscure transitional and mixed states,[12,13] Milo analysis was applied to resolve 20 overlapping TIL neighborhoods,[12] which showed significant differential abundance (DA) between DCIS and IBC (Figures 1C and 1D). Milo detected IBC-skewed gradients of cycTreg, suppressive non-cycTreg, and activated CD4$^+$ states, consistent with a progression-driven shift toward CD4$^+$ and Treg dominance (Figure 1E). Rat mammary tissues

(C–E) Milo neighborhoods of human T cells (C) and DAs (Differential Abundances) in IBC vs. DCIS as shown by UMAP plot (D) or beeswarm plot (E).
(F) UMAP plots of SD rat T cells (n = 13) showing condition-specific grouping (inset).
(G–I) Milo neighborhoods of rat T cells (G), enrichment in NMU-treated tumors vs. MGs (H), or beeswarm plot (I). Node size denotes cell numbers, and edges denote cells shared between connected neighborhoods. Beeswarm plots show LFC distribution at FDR 10% of neighborhoods between IBC vs. DCIS (E) or rat NMU-treated tumors vs. MGs (I).
(J) UMAP plots of human CD4$^+$ T cells.
(K) Beeswarm plots of T cell neighborhoods and LFC distribution for pairwise comparisons between three IBC subtypes (IBC/HR$^+$: n = 6; IBC/TNBC: n = 10; IBC/HER2$^+$: n = 8).
UMAP, uniform manifold approximation projection; DAs, ; LCF, log fold-change.
See also Figure S1 and Table S1.

Please cite this article in press as: Bui et al., Identification of cycling regulatory T cell precursors as conductors of immune escape during breast carcinoma progression, Cancer Cell (2026), https://doi.org/10.1016/j.ccell.2026.03.015

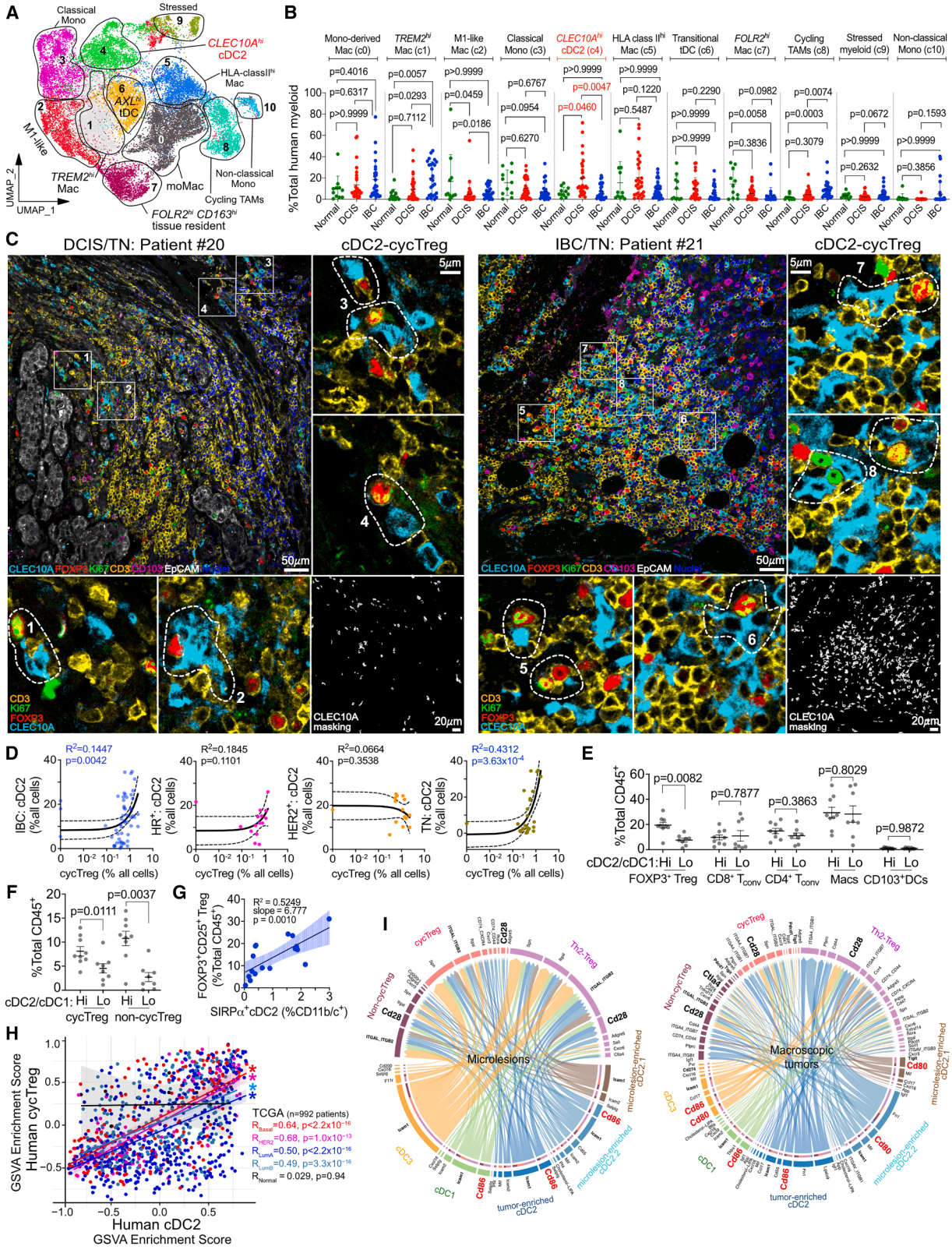

Figure 2. Myeloid heterogeneity and cDC2-mediated antigen presentation in DCIS and IBC

(A and B) UMAP plot (A) and quantification (B) of human myeloid cell states (normal: $n = 11$; DCIS: $n = 29$; IBC: $n = 26$). Patients with <100 myeloid cells were excluded. Unadjusted significance values were computed by Kruskal-Wallis test and Tukey's multiple comparison.

(legend continued on next page)

Please cite this article in press as: Bui et al., Identification of cycling regulatory T cell precursors as conductors of immune escape during breast carcinoma progression, Cancer Cell (2026), https://doi.org/10.1016/j.ccell.2026.03.015

exhibited 10 T cell states dominated by dysfunctional phenotypes, including Tpex (Progenitor Exhausted T cells), stressed T cells, and cycTreg (Figures 1F and S1H). Milo identified tumor-skewed neighborhoods of cycTreg and multiple non-cycTreg subsets (Figures 1G–1I). Projection of human and rat datasets onto a pan-cancer TIL atlas[14] supported a conserved transition from $CD8^+$ naïve-like states in early lesions to $CD4^+$-enriched TIMEs in both species (Figures S1I–S1K). In rats, this shift was observed across time points, with microlesions enriched for naïve-like $CD8^+$ and macroscopic tumors dominated by $CD4^+$ Treg, including cycTreg (Figures S1L–S1O).

Human $CD4^+$ TILs were resolved into 14 substates (Figure 1J). *FOXP3*$^+$ Tregs comprised six distinct populations, including cycTreg, *LAG3*^{hi} and *PDCD1*^{hi} eTreg (Effector Treg), Th2-like Treg, and mature *IKZF2*^{hi} and *IKZF4*^{hi} Treg. $CD4^+$ conventional T cells ($CD4^+$ Tconv) included Tr1 cells (*GZMK* and *PRF1*), Th2 (*GATA3*), and stressed and exhausted TILs (Figures S1P and S1Q). Milo analyses within $HER2^+/HR^-$ and $HR^+/HER2^-$ subtypes revealed that DCIS harbored more diverse $CD8^+$ neighborhoods, including effector and cytotoxic states, than subtype-matched IBC (Figure S1R). DCIS cases with low cycTreg abundance showed subtype-specific patterns. HR^+ DCIS favored naive T cells, whereas $HER2^+$ DCIS exhibited cytotoxic $CD8^+$ and Tpex enrichment, indicating a more immune-reactive TIME (Figure S1S). $CD8^+$ clustering confirmed skewed distribution of $CD8^+$ states in normal and DCIS tissues, especially within $HER2^+$ and HR^+ subtypes (Figure S1T).

In invasive tumors, HR^+ IBC displayed the least diverse TIL neighborhoods, dominated by memory-like and terminally exhausted $CD8^+$. $HER2^+$ IBC was enriched for cytotoxic and effector $CD8^+$ T cells, whereas TNBC exhibited strong Treg representation, including cycTreg and mature Treg, resulting in the highest cycTreg abundance among BC subtypes (Figure 1K). Rat $CD4^+$ T cells mirrored human diversity, with multiple Treg and dysfunctional subsets enriched in tumors, whereas naïve-like T cells were restricted to normal MGs (Figure S1U). Rat $CD8^+$ naive cells were confined to normal tissue, while cytotoxic and Tex states were exclusive to tumor TIMEs (Figure S1V).

Differential modes of type 2 antigen presentation

Profiling of human myeloid lineages identified 11 macrophage, DC, and monocyte states (Figures 2A, S2A, and S2B). M1-like TAMs were reduced in DCIS, while *FOLR2*^{hi} tissue-resident TAMs were diminished in IBC. In contrast, *TREM2*^{hi} and cycling TAMs were enriched in IBC. Among DC subsets, *CLEC10A*^{hi} cDC2 were the only myeloid population significantly elevated in DCIS (15%–65% of total myeloid), suggesting a unique role in early disease and DCIS-to-IBC transition (Figure 2B). On protein level, $CLEC10A^+$ cDC2 were abundantly observed across all DCIS and IBC subtypes and were frequently observed in physical contact with both cycling and non-cycling Treg (Figure 2C). In shared tumor regions, cDC2 abundance positively correlated with cycTreg levels in IBC, driven primarily by TNBC, whereas $CD103^+$ $CLEC10A^-$ DCs showed no such association (Figures 2D and S2C). Because cycTreg were rare or absent in many pure DCIS samples, the phenotypic cDC2-cycTreg relationship in early lesions remains unresolved (Figure S2D).

Given the role of HLA class II in $CD4^+$ priming,[15] antigen presentation was evaluated across antigen-presenting cell (APC) classes. Professional APCs (myeloid, B cells, plasma cells, and plasmacytoid DCs/pDCs) displayed the highest HLA class II expression in DCIS (Figure S2E). Parallel scRNA-seq profiling in rats revealed tumor enrichment of TAMs and multiple cDC1/cDC2 subsets (Figures S2F and S2G). Rat cDC2 states expressed the highest levels of DC-specific class II genes (*Rt-Doa* and *Rt-Dob*) (Figure S2H). Comparison of rat microlesions and macroscopic tumors showed a shift from *Folr2*^{hi} tissue TAMs in microlesions to tumor-specific cDC2 and M2-like TAMs in tumors (Figures S2I and S2J), accompanied by increased cDC2 and MHC-II^{hi} TAM abundance, when immunophenotypically assessed (Figure S2K).

To assess non-canonical APCs, epithelial compartments from humans and rats were resolved into 31 and 12 subclusters, respectively, spanning normal luminal, basal, and myoepithelial lineages as well as cancer epithelium (Figures S2L and S2M). Based on HLA class I and II expression, epithelial clusters were categorized into class II-positive, class I-high, and class I-low/neg groups (Figure S2N). When aggregated, human DCIS epithelium exhibited significantly elevated HLA class II and class I expressions, indicating enhanced APC potential (Figure S2O). Rat HR^+ luminal and LP clusters showed enriched class II expression (Figure S2P). C2TA, the master regulator of HLA class II, was highly expressed in myeloid cells in DCIS, particularly in *CLEC10A*^{hi} cDC2, peaking in DCIS and declining in IBC, whereas TAMs maintained high *CIITA* expression in IBC (Figure S2Q). Several cancer epithelial clusters also expressed CIITA, consistent with increased class II and class I epithelia in IBC (Figure S2R).

(C) Representative 7-plexed confocal images of triple-negative DCIS and IBC tumors. Insets display magnified 4-channel regions of interest (ROIs), highlighting $CLEC10A$ cDC2$^+$ and cycTreg. Dotted contours mark regions of cDC2-Treg proximity. CLEC10A masking denotes automated cDC2 detection. Scale bars: 50 μm (main panels), 20 μm (mask), and 5μm (ROIs).

(D) Pearson correlation analyses of cDC2 and cycTreg frequencies in spatially matched IBC regions (blue; $n = 55$ regions from 11 patients, five 5×5 stitched FOVs/patient) and stratified by molecular subtypes (HR^+: $n = 15$; $HER2^+$: $n = 15$; TN: $n = 25$). The x axis is in log-scale due to low cycTreg frequency. Bold lines represent mean regression trends, and dotted lines denote 95% confidence interval (CI).

(E and F) Quantification of T cell and myeloid cell types (E) and cycTreg vs. non-cycTreg (F) in cDC2-Hi vs. cDC2-Lo tumors (Hi: >1.5, $n = 9$; Lo: <0.75, $n = 8$ tumors). Significance was computed by Kruskal-Wallis test and Tukey's multiple comparison.

(G) Linear regression of cDC2 and total Treg burden.

(H) Linear regression of cycTreg and cDC2 estimated scores in TCGA ($n = 992$), as stratified by PAM50 subtypes.

(I) Chord diagrams depicting outgoing signaling from cDC subsets to Treg in microlesions (left) and macroscopic tumors (right). Inferred Cd80/Cd86-Cd28 co-stimulatory interactions are shown.

In (D), (G), and (H), Pearson's best-fit parameters including R (or R^2), significance values, and 95% CI are shown.

See also Figure S2; Tables S1 and S3.

Please cite this article in press as: Bui et al., Identification of cycling regulatory T cell precursors as conductors of immune escape during breast carcinoma progression, Cancer Cell (2026), https://doi.org/10.1016/j.ccell.2026.03.015

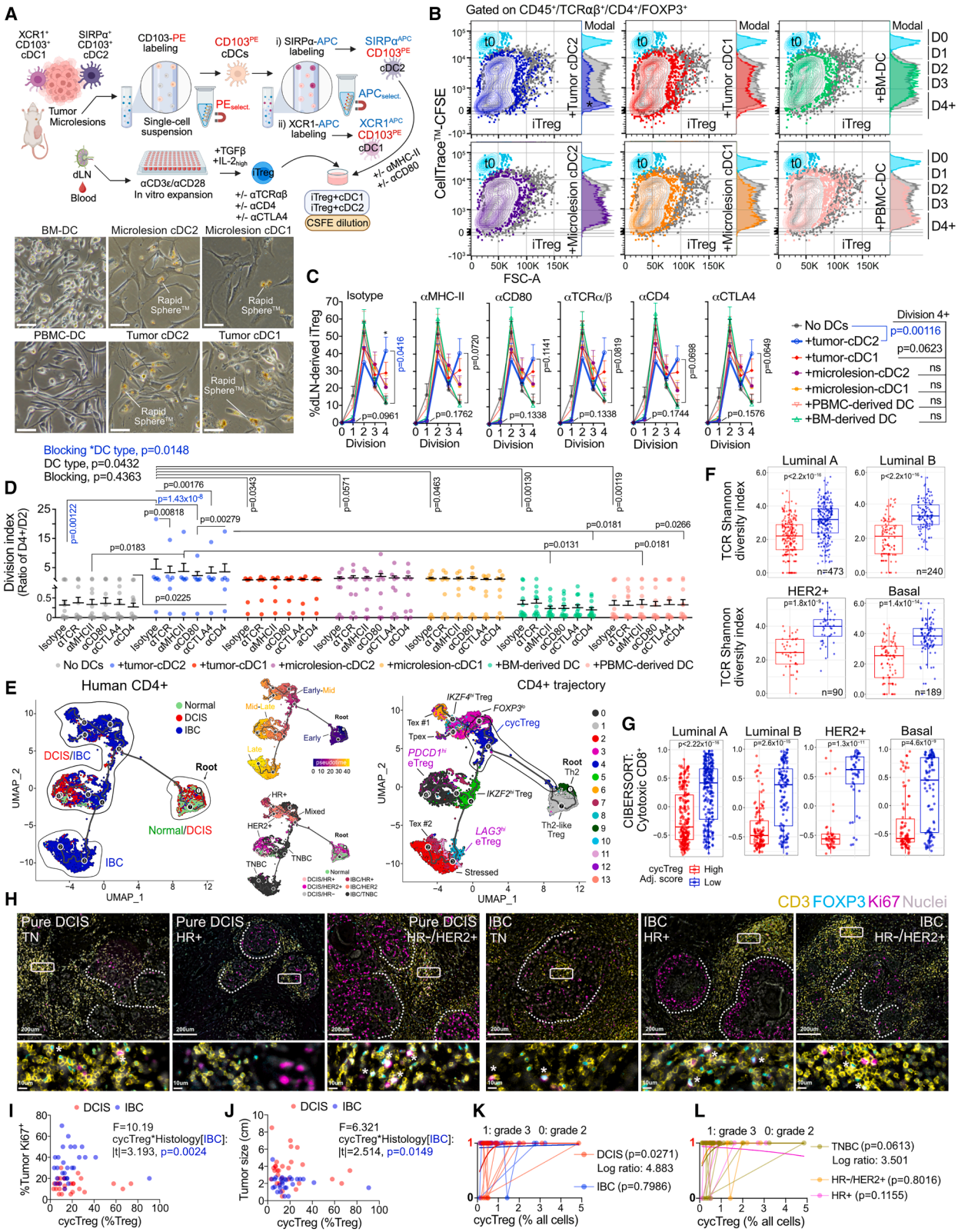

(legend on next page)

Please cite this article in press as: Bui et al., Identification of cycling regulatory T cell precursors as conductors of immune escape during breast carcinoma progression, Cancer Cell (2026), https://doi.org/10.1016/j.ccell.2026.03.015

cDC2 track cycTreg levels in rat and TCGA breast tumors

cDC2-Treg relationship was investigated in SD rats to determine how DC subtype imbalance shapes intratumoral Treg expansion. cDC2 were more proliferative than cDC1 or TAMs and expressed higher levels of the co-stimulatory ligand CD86 (Figures S2S and S2T), indicating enhanced activation and antigen-presenting capacity. Because selective DC depletion is not feasible in rats, tumors were stratified into the cDC2-high and cDC2-low groups, using the SIRPα/XCR1 ratio (Figure S2U). Tumors in the cDC2-high stratum exhibited significantly elevated FOXP3$^+$ Treg burden, including both cycTreg and non-cycTreg (Figures 2E and 2F). Correlative analyses confirmed strong associations between cDC2 abundance and FOXP3$^+$ Treg (Figure 2G) and CD4$^+$ Tconv, but not CD8$^+$ Tconv (Figures S2V, left, and S2W). Analyses in the TCGA BC cohort[16] showed robust positive associations between cDC2 and cycTreg across basal, HER2$^+$, and luminal A and B subtypes (Figure 2H; n = 992 patients). In contrast, cDC1 correlated only with CD4$^+$ Tconv (Figures S2W, right and S2X) and showed no relationships with Treg or CD8$^+$ Tconv. These findings support a model in which cycTreg expansion in both human and rat tumors is tightly linked to increased HLA class II availability and intratumoral cDC2 frequency.

To test whether cDC2 directly drive cycTreg proliferation, CellChat analysis was used for quantifying outgoing signaling from cDC subsets in rat microlesions and tumors. Beyond integrin-mediated adhesion pathways, the dominant cDC2-cycTreg interactions involved immune-synapse formation through Treg-expressed CD28/CTLA4 and DC-expressed CD80/CD86 (Figure 2I). This suggested that direct cDC2-to-Treg contact elicits cycTreg expansion. To functionally validate this, paired isolations of T cells from tumor-draining lymph nodes (dLNs) and peripheral blood, along with cDC1 and cDC2 from microlesions or tumors, were performed (enrichment efficiency shown in Figure S3A). T cells were polarized into inducible Treg (iTreg) (Figure S3B) before (CSFE) carboxyfluorescein diacetate succinimidyl ester-based cycling assays in 5-day co-cultures with autologous DC subsets (Figure 3A).

Only tumor-localized cDC2 induced rapid and robust expansion of dLN-derived iTreg, yielding a high proportion of cells reaching division 4 and beyond (D4+) (Figures 3B and 3C). Microlesion-derived cDC2 failed to induce expansion, and tumor-localized cDC1 elicited a weak, non-significant effect. These results indicate that both the identity of cDC2 and their conditioning within the tumor microenvironment are required for the expansion of cycTreg. Disruption of the cDC2-Treg immune synapse via blockade of major histocompatibility class II (MHC class II) or CD80 on DCs, or αTCRα/β, αCTLA4, and αCD4 on iTreg significantly impaired cDC2-driven expansion (Figure 3C). Division indices (D4+/D2) were the highest in tumor-derived cDC2 co-cultures and were markedly reduced by TCR or MHC class II blockade, establishing dependency on antigen-specific synapse formation (Figure 3D). cDC2-mediated expansion occurred only in iTreg derived from tumor-dLNs, not from systemic peripheral blood mononuclear cells (PBMCs) (Figure S3C), demonstrating that local tumor proximity is essential for Treg responsiveness to cDC2.

Trajectorial inference identifies cycTreg at DCIS-IBC junction

Trajectorial inference using Monocle3[17] revealed a continuum of CD4$^+$ TIL states across normal breast, DCIS, and IBC. Pseudotime was rooted in normal breast T cells and progressed toward a DCIS-IBC junction, followed by an IBC-specific domain enriched for mature Treg, eTreg, and dysfunctional CD4$^+$ states (Figure 3E). The transition from normal-DCIS region occupied by Th2 and Th2-like Treg to DCIS-IBC junction was bridged by cycTreg cluster. This location indicates that cycTreg function as a regulatory checkpoint that enabled mature Treg phenotypes in IBC. Supporting this, CD4$^+$ TILs exhibited the highest number of decision branches at the DCIS-IBC junction, whereas CD8$^+$

Figure 3. Tumor-derived cDC2 elicits Treg expansion predicting adverse immune and tumor outcomes

(A) Schematic of *ex vivo* iTreg-DC co-culture. Bright-field images of dendriform morphologies typical of DCs. Scale bars, 10 μm.

(B) Contour plots depicting CellTrace-CSFE dilution in dLN-derived iTreg following co-cultures with cDC1 or cDC2 derived from macroscopic tumors or microlesions, or with BM- or PBMC-derived moDCs. T_0 baseline (cyan) and iTreg monoculture (gray) are included. CSFE signal is visualized as contour overlays and as mode-normalized histogram. Asterisk indicates significant D4+ division shift in co-cultures with tumor-derived cDC2 (blue).

(C) Line plots showing the proportions of dLN-derived iTreg entering division states D0-D4+ in monoculture or co-cultures with DC subsets, with/without blockade of immune synapse components (10 μg/mL per mAb) (across treatments: no DCs, n = 12; +tumor-cDC1 or cDC2, n = 6; +microlesion-cDC1 or cDC2, n = 9; +BM- or PBMC-derived DC, n = 12). Significance for each treatment was computed by two-way repeated-measures (RM) ANOVA and Dunnett's multiple comparisons, with p values reported for D1 and D4+ states. Pooled-variance two-way ANOVA was applied for D4+ states to evaluate cross-treatment differences among DC subtypes.

(D) The division index calculated as the peak-to-trough ratio of iTreg in D4+ relative to D2. Individual or interaction effects of DC co-culture and blockade conditions were assessed by two-way RM ANOVA. Tukey's post-hoc analysis was used for TCR/MHC-II blockade in tumor-derived cDC2 co-cultures.

(E) Trajectorial inference of human CD4$^+$ grouped by progression stage (left) and Seurat clusters (right). Pseudotime values and molecular subtype are shown as insets.

(F and G) TCR Shannon's diversity index (F) and cytotoxic CD8$^+$ scores (G) of primary breast tumors among PAM50 subtypes from the TCGA cohort (luminal A: n = 473; luminal B: n = 240; HER2$^+$: n = 90; basal: n = 189). Stratification was based on median cutoff of adjusted cycTreg score. Significance was computed using Wilcoxon rank-sum test.

(H) cycTreg and non-cycTreg in pure DCIS (left) and IBC (right) classified as TN, HR$^+$/HER2$^-$, and HR$^-$/HER2$^+$ (DCIS: TN, n = 13; HR$^+$, n = 9; HR$^-$/HER2$^+$, n = 6; IBC/DCIS: TN, n = 12; HR$^+$, n = 11; HR$^-$/HER2$^+$, n = 5). Dotted lines demarcate tumor-stroma borders. Rectangles denote magnified ROIs. Asterisks denote cycTreg. Scale bars, 250 μm and 10 μm (insets).

(I and J) Multivariable linear regression of cycTreg stratified by DCIS or IBC, with tumor Ki67$^+$ (I) and tumor size (J) as predicted outcomes. Covariate interactions were evaluated by least-square regression.

(K and L) Logistic regression by nuclear grade outcomes (1: high vs. 0: low) based on cycTreg, with patients stratified by DCIS or IBC (K) or histologic subtypes (L). See also Figure S3; Tables S1 and S3.

Please cite this article in press as: Bui et al., Identification of cycling regulatory T cell precursors as conductors of immune escape during breast carcinoma progression, Cancer Cell (2026), https://doi.org/10.1016/j.ccell.2026.03.015

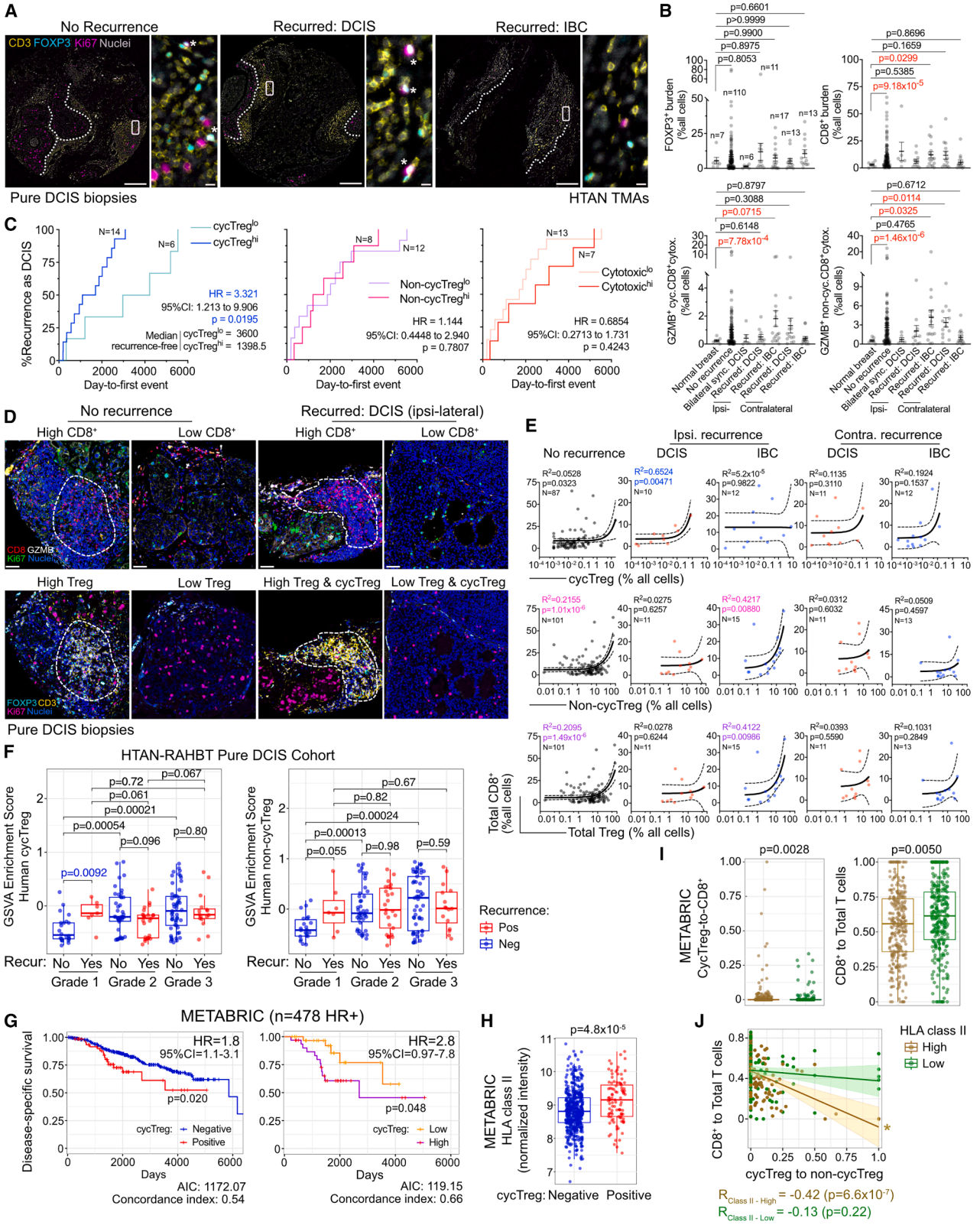

Figure 4. Treg-rich microenvironment predicts recurrence in HTAN DCIS cohorts

(A) Representative images of pure DCIS lesions with/without recurrence as DCIS or IBC. Insets display enlarged TIL-rich regions with/without cycTreg (asterisks). Scale bars, 250 μm and 10 μm.

(legend continued on next page)

branching was distributed more evenly across normal, normal-DCIS, and DCIS-IBC regions (Figure S3D, top). Myeloid branching was uniform, underscoring the temporal specificity of $CD4^+$ lineage remodeling during progression (Figure S3D, bottom). Examination of myeloid gene expression along pseudotime revealed early upregulation of HLA class II genes including DC-specific *HLA-DPB1* and *HLA-DQB1* in DCIS (Figure S3E), aligning with cDC2-mediated antigen presentation during DCIS-to-IBC transition.

TNFRSF4 as a biomarker to distinguish proliferation of human Treg

To identify regulators of Treg proliferation, high-dimension weighted gene co-expression network analysis was applied to cycTreg and non-cycTreg (Figure S3F). *TNFRSF4* (OX40) emerged as a major hub gene within cycTreg (M4) and non-cycTreg (M3), embedded in a *TNFRSF4/18/25/1B* network linked to core Treg genes (*IKZF2*, *BATF*, *ICOS*, *CTLA4*, and *IL2RA*) (Figure S3G). Gene Ontology (GO) analysis showed TNFRSF4-associated modules enriched for pathways related to "positive regulation of lymphocyte proliferation," reinforcing its relevance to Treg expansion (Figure S3H). A cycTreg-specific module was constructed using *FOXP3*, cycling genes (*MKI67*, *TOP2A*, and *CDK1*), and highly expressed receptors (*TNFRSF4*, *LAG3*, and *PDCD1*), which was normalized to core Treg program. Projection of this module onto rat Visium maps revealed a progressive increase in cycTreg signatures from MGs to tumors. Because cycTreg expansion was likely driven by antigen presentation by cDC2, a rat HLA class II module was also projected onto Visium map, showing a corresponding increase in class II expression in tumors. Class II expression was spatially localized contrary to the uniform class I distribution (Figure S3I; Visium expression spots in Table S3).

CycTreg as a predictor of immune dynamics and tumor outcomes

The cycTreg program showed strong clinical relevance and emerged as a marker of impaired anti-tumor immunity and more aggressive disease biology. We applied an adjusted cycTreg score to stroma-deconvoluted TCGA breast tumors (Figure S3J). Tumors enriched for the cycTreg signature consistently exhibited a lower immune score and Shannon TCR diversity, as well as markedly diminished immune-reactive cell types, including total lymphocytes, cytotoxic and naive $CD8^+$ TILs, and cDC1 (Figures 3F, 3G, and S3K–S3M). These features reflected a tumor niche with weakened T cell integrity and suppressed immune dynamics. Tumor mutation burden did not differ between cycTreg-high and cycTreg-low groups, indicating that the immune deficits were not attributable to mutational load but instead aligned with the presence or absence of cycTreg (Figure S3N).

To evaluate clinical associations, cycTreg frequency and overall Treg burden were examined across three additional cohorts: (1) a pure DCIS and IBC cohort ($n = 56$), (2) the RAHBT cohort and four HTAN microarrays ($n = 165$ and 177, respectively),[18] and (3) the METABRIC imaging mass cytometry cohort ($n = 610$).[19] In the pure DCIS/IBC cohort, TN DCIS exhibited the highest Treg burden driven largely by mature non-cycTreg (Figures 3H and S3O). Because cycTreg abundance varied widely across patients, multivariable and logistic regression models were used to assess prognostic relationships. In IBC, cycTreg frequency showed significant interactions with tumor histology, predicting higher tumor $Ki67^+$ proliferation and larger tumor size (Figures 3I and 3J), whereas subtype-based regression did not reveal similar associations (Figures S3P and S3Q). Logistic regression demonstrated that increased cycTreg in DCIS was associated with a higher likelihood of grade 3 DCIS, with TN DCIS cases showing a similar trend toward higher nuclear grade when cycTreg levels were elevated (Figures 3K and 3L). Across all cohorts, TIL heterogeneity was substantial in both DCIS and IBC, but cycTreg consistently aligned with features of poor immunity and more aggressive tumor phenotype.

$FOXP3^+$ Treg are associated with DCIS recurrence risk

We subsequently investigated whether variations in cycTreg and non-cycTreg in pure DCIS are associated with recurrence risk. In pure DCIS, cycTreg were detectable but generally rare (<1%) and did not differ significantly across outcome groups (Figures 4A and S4A), consistent with the low-grade composition of the HTAN DCIS cohort. Total Treg and non-cycTreg levels were heterogeneous (Figures 4B and S4A). Pure DCIS cases without recurrence showed significant enrichment of total $CD8^+$ TILs and both cycling and non-cycling $GZMB^+$ cytotoxic $CD8^+$ TILs relative to normal breast (Figure 4B). Patients who

(B) Quantification of total $FOXP3^+$ Treg and $CD8^+$ TILs, as well as cycling and non-cycling cytotoxic $CD8^+$ T cells in normal breast and in pure DCIS patients with different outcomes. TMA501-504 cohorts, $n = 177$; no recurrence, $n = 110$; ipsilateral recurrence as DCIS or IBC, $n = 10$ and 17, respectively; contralateral recurrence as DCIS or IBC ($n = 13$); bilateral synchronous DCIS, $n = 6$; and normal breast, $n = 7$.
(C) Log rank Mantel-Cox tests of time to first DCIS recurrence as stratified by cycTreg, non-cycTreg, and cytotoxic $CD8^+$ T cells. Hazard ratios with CI were derived using the Mantel-Haenszel method. DCIS patients with no T cell infiltration ($n = 4$) were excluded from analyses.
(D) Immunofluorescence of spatial co-localized non-cycTreg and total infiltrating $CD8^+$ T cells in DCIS without recurrence (left), or cycTreg and $CD8^+$ in patients with DCIS recurrence (right). Dotted outlines mark regions of co-occupancy. Scale bars, 50 μm.
(E) Pearson correlation analyses of cycTreg (top), non-cycTreg (middle), and total Treg (bottom) with total infiltrating $CD8^+$ T cells in DCIS patients with different outcomes. Patients with no cycTreg or non-cycTreg detected were excluded. The *x* axis is displayed in log-scale due to low Treg frequency.
(F) GSVA enrichment of non-cycTreg and cycTreg modules with or without recurrence in RAHBT DCIS cohort (grade 1, no: $n = 22$; yes: $n = 7$; grade 2, no: $n = 42$, yes = 25; grade 3: no = 53, yes = 16). Significance was computed using Kruskal-Wallis test.
(G) Cox proportional hazard analyses of disease-specific survival of patients with HR^+ tumors ($n = 478$), tumors with positive vs. no cycTreg signal (top), or between high vs. low cycTreg stratum, using two-tailed log-rank test.
(H and I) Total HLA class II expression stratified by cycTreg detection (H), cycTreg-to-$CD8^+$ ratio (I, left), and $CD8^+$-to-total T cell ratio (I, right) stratified by high vs. low HLA class II scores within the METABRIC cohort (positive/negative, $n = 610$). Significance was computed using non-parametric Wilcoxon rank-sum test.
(J) Linear regression analysis of $CD8^+$-to-total T cells and cyc-to-non-cycTreg ratios based on HLA class II scores.
In (E) and (J), best-fit Pearson coefficients, confidence bands, and *p* values are reported.
See also Figure S4; Tables S1 and S3.

Please cite this article in press as: Bui et al., Identification of cycling regulatory T cell precursors as conductors of immune escape during breast carcinoma progression, Cancer Cell (2026), https://doi.org/10.1016/j.ccell.2026.03.015

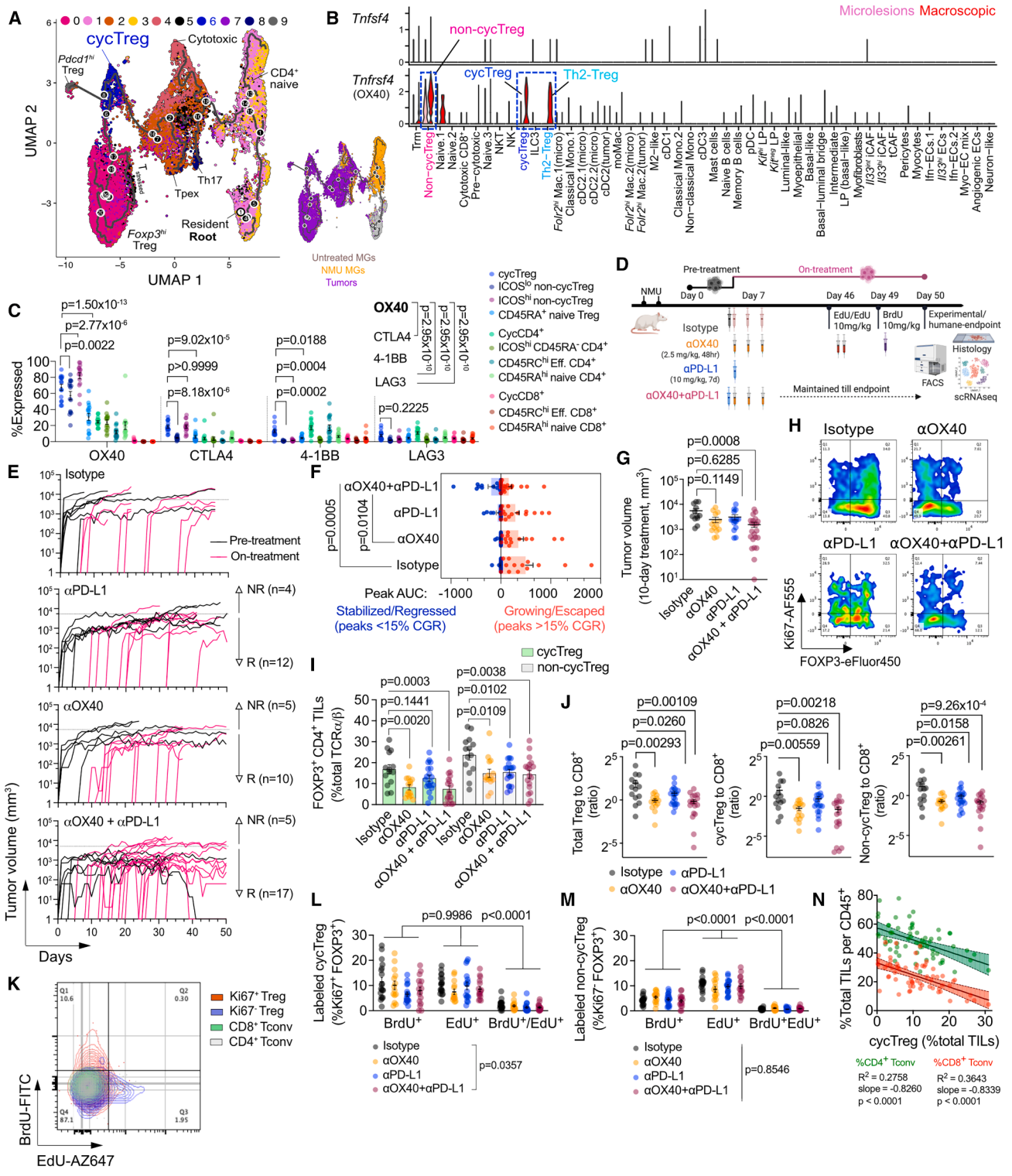

Figure 5. OX40^{hi} cycTreg is cycling precursors sustaining Treg pool and immune escape

(A) Pseudotime trajectory of rat T cells.

(B) OX40 ligand-receptor expression across cell types within rat macroscopic tumors and microlesions.

(C) % TIL subtypes with OX40, CTLA4, 4-1BB, and LAG3 positivity (n = 15 tumors).

(D) Schematic of rat immunotherapy study coupled with EdU/BrdU dual pulse chase.

(E) Spaghetti plots of individual tumor growth curves (isotype: n = 16; αOX40: n = 15; αPD-L1: n = 16; combo: n = 23).

(F) Derivative distribution of the growth rate of individual tumors quantified as negative (blue) or positive (red) peak area-under-curve (AUC).

(legend continued on next page)

later developed ipsilateral IBC also showed elevated CD8$^+$ and cytotoxic TIL infiltration, a pattern not observed in those who recurred with ipsilateral DCIS (Figure 4B).

Time-to-event analyses revealed that only high cycTreg abundance predicted significantly shorter time to DCIS recurrence (HR = 3.321), whereas non-cycTreg and cytotoxic CD8$^+$ levels did not stratify recurrence intervals (Figures 4C and S4B). No T cell-based stratification predicted time to ipsilateral IBC. Correlative analyses between Treg subsets and CD8$^+$ TILs identified three distinct patterns. In patients who later developed ipsilateral DCIS, total CD8$^+$ TILs correlated positively with cycTreg but not non-cycTreg, suggesting preferential recruitment or expansion of cycTreg in lesions with ipsilateral DCIS recurrence (Figures 4D and 4E, top). In contrast, patients without recurrence and those who progressed to ipsilateral IBC both showed strong correlations between CD8$^+$ TILs and non-cycTreg or total Treg burden (Figure 4E, middle and bottom). Only the non-recurrent group exhibited additional correlations between both Treg subsets and GZMB$^+$ cytotoxic CD8$^+$ TILs, indicating that effective coupling between Treg and cytotoxic TILs may contribute to immune protection, whereas its absence may underlie progression to IBC (Figure S4C).

To overcome the scarcity of cycTreg in tissue sections, cycTreg and non-cycTreg scores were projected onto stromal bulk RNA-seq from 165 pure DCIS cases.[18] Both modules increased with nuclear grade. Among grade 1 DCIS, recurrent cases had significantly higher cycTreg scores than non-recurrent cases (Figure 4F). Individual cycTreg genes did not stratify recurrence (Figure S4D), and both CD8$^+$ naive and cytotoxic modules showed no differences (Figure S4E). Multivariable regression confirmed that a high cycTreg score predicted recurrence only in grade 1 DCIS (Figure S4F). Treatment modality did not alter predictive value (Figure S4G).

In IBC, mass cytometry imaging from the METABRIC cohort[19] showed that cycTreg presence or enrichment, as defined by Ki67 threshold (Figures S4H and S4I), strongly predicted shorter disease-specific survival (Figure 4G). cycTreg-positive tumors had significantly lower CD8$^+$ TIL representation (Figure S4J) and markedly higher HLA class II scores (Figure 4H). Stratification by HLA class II revealed that class II-high tumors had higher cycTreg-to-CD8$^+$ ratios and reduced CD8$^+$ infiltration (Figure 4I). A strong inverse correlation between cycTreg and CD8$^+$ abundance in class II-high tumors (Figure 4J) again underscored the link between type 2 antigen presentation and cycTreg expansion. When compared with other diagnostic parameters, cycTreg presence was found to be the strongest predictor of poor disease-specific survival (Figure S4K). These findings demonstrated that cycTreg and non-cycTreg patterns serve as predictors of recurrence in DCIS and as indicators of immune suppression and poor prognosis in IBC.

CycTreg sustain Treg-dependent immune escape and are targetable via OX40 agonism

Rat T cell trajectory demonstrated that cycTreg occupy a pivotal transitional position in shaping the Treg-dominant TIMEs of mammary tumors (Figure 5A). Resembling human BC, rat T cells were ordered from naive T cells in untreated MGs and progressed to cytotoxic and Tpex in microlesions and mammary tumors (Figure 5A). Terminal domains were dominated by *Foxp3*^{hi} non-cycTreg, immediately preceded by *Foxp3*^{int} cycTreg (Figure 5A). This placement mirrors human TIL trajectories and indicates that cycTreg act as a precursor bridging early immune activation to mature, suppressive Treg states.

Rat *Tnfrsf4* (OX40) was strongly associated with "positive regulation of lymphocyte proliferation" (Figure S3H), and ligand-receptor analysis confirmed that OX40 expression was restricted to Treg populations (Figure 5B). *Tnfrsf4* expression was elevated in non-cycTreg and Th2-Treg within macroscopic tumors and was detectable only in tumor-localizing cycTreg, and not in microlesions (Figure 5B). Flow cytometry showed that ~74% of cycTreg were OX40$^+$ compared to 58% of non-cycTreg, 32% of naive Treg, 17%–22% of CD4$^+$ Tconv, and 0% of CD8$^+$. Only ICOS^{hi} effector-like Treg exceeded cycTreg in OX40 abundance. cycTreg also expressed higher levels of CTLA4 and 4-1BB than other TIL subsets, whereas LAG3 did not differ (Figure 5C). OX40^{hi} cycTreg and OX40^{hi} effector-like Treg were 3–4 times more abundant than CTLA4^{hi}, 4-1BB^{hi}, or LAG3^{hi} Treg, prioritizing OX40 as a strong therapeutic target.

An *in vivo* study was performed to evaluate the immune effects of αOX40 agonist (clone OX-86[20]), αPD-L1, and their combination on cycTreg (Figure 5D). The experiment was enhanced by the employment of EdU/BrdU dual pulse-chase system to track the proliferation kinetics of cycTreg and non-cycTreg with mature phenotypes. To assess tumor kinetics, their volumes were monitored, and the cumulative growth rate (CGR)[21] was calculated based on treatment duration, enabling classification of the response phenotype of individual tumors (Figures S5A–S5C). Most rats developed additional tumors during treatment, and, thus, tumors were categorized as pre-treatment or on-treatment (Figure 5E). αPD-L1 or αOX40 monotherapy stabilized <50% of tumors, whereas dual αOX40/αPDL-1 therapy stabilized or regressed 75% tumors, significantly outperforming monotherapies (Figures 5E and S5D–S5G). Tumor volumes, CGRs, net change from baseline, and tumor weights all

(G) Tumor volumes at 10-day post initial treatment.
(H and I) Flow diagram of cycTreg density (H) and frequency of cycTreg and non-cycTreg (I).
(J) Ratios of total Treg, cycTreg, and non-cycTreg to total infiltrated CD8$^+$ T cells.
(K) EdU/BrdU contours of TILs. Quadrants denote EdU$^+$/BrdU$^+$ distribution.
(L and M) Frequency of BrdU$^+$, EdU$^+$, or double-labeled cycTreg (L) and non-cycTreg (M). Significance was computed by two-way ANOVA and Dunnet's multiple comparison relative to BrdU-labeling.
(N) Linear regression of cycTreg with CD8$^+$ Tconv (red) and CD4$^+$ Tconv (green). Dots in each color represent individual tumors (n = 64). Pearson's best-fit parameters including R^2, slope, and significance, and 95% CI are shown.
In (C) and (F), significance was computed by two-way ANOVA and Dunn's multiple comparison. In (E), values are shown in $\log_{10}$ scale to show very small tumors in responding groups. Pre- or on-treatment tumors are specified. In (J), values are shown in $\log_2$ scale to show tumors with low Treg infiltration.
See also Figure S5 and Table S3.

Please cite this article in press as: Bui et al., Identification of cycling regulatory T cell precursors as conductors of immune escape during breast carcinoma progression, Cancer Cell (2026), https://doi.org/10.1016/j.ccell.2026.03.015

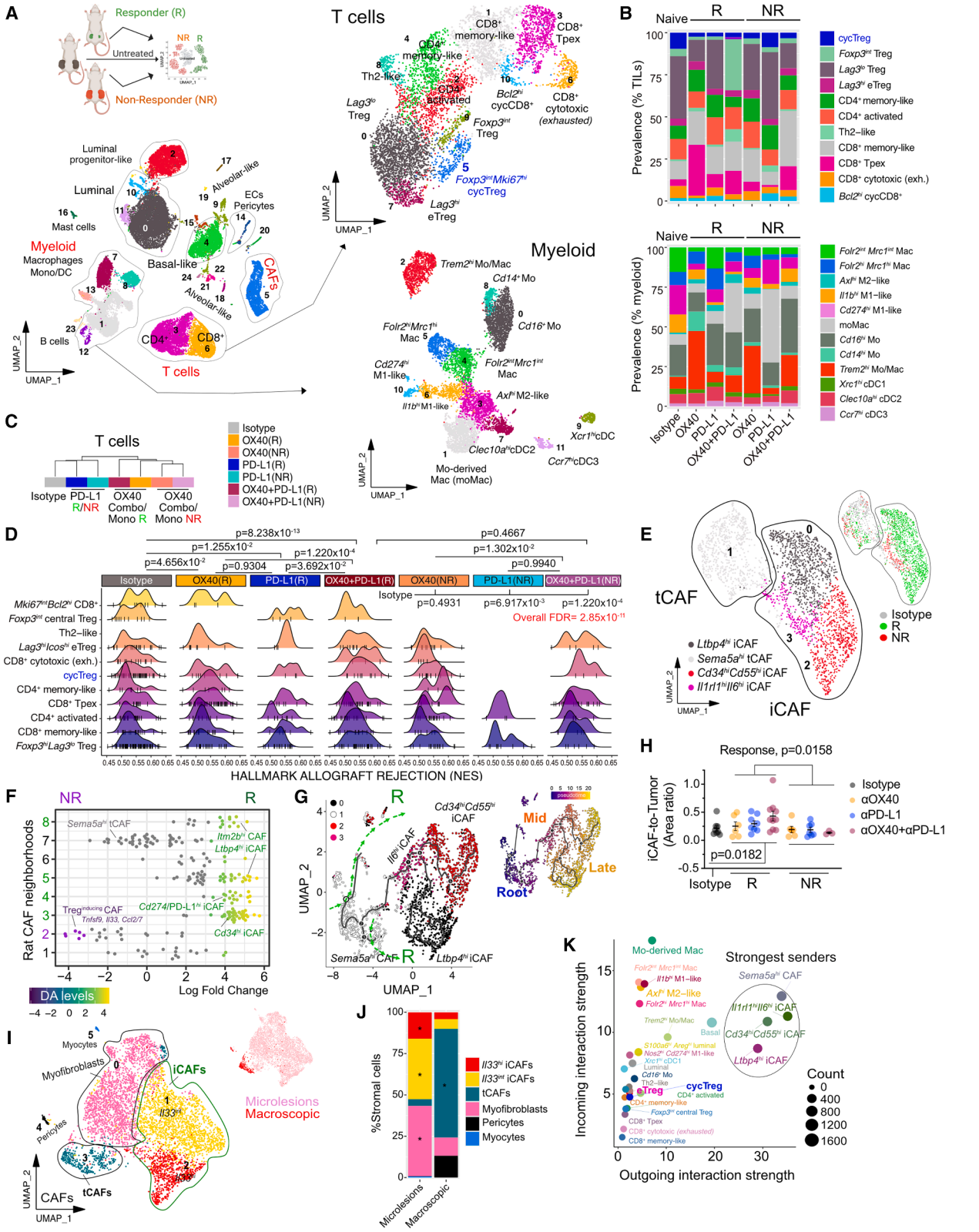

Figure 6. The effects of combined OX40 agonist and αPD-L1 on mammary tumors

(A and B) Schematic and UMAP plots (A) and stacked bar plot quantification of TILs (B, top) and myeloid cells (B, bottom) of responders (R) and non-responders (NR) (n = 2 tumors per treatment-response).

(legend continued on next page)

Please cite this article in press as: Bui et al., Identification of cycling regulatory T cell precursors as conductors of immune escape during breast carcinoma progression, Cancer Cell (2026), https://doi.org/10.1016/j.ccell.2026.03.015

confirmed superior efficacy of the dual regimens (Figures 5G and S5D–S5H). Pre-treatment tumors responded uniformly, whereas on-treatment tumors showed bi-modal responses, suggesting emerging immune resistance (Figure S5E).

Immunophenotyping revealed that all regimens reduced FOXP3$^+$ Treg and increased CD4$^+$ Tconv, but only dual-targeting enhanced CD8$^+$ infiltration (Figures S5I and S5J). OX40 agonism, alone or in combination, markedly reduced cycTreg and non-cycTreg (Figures 5H and 5I), lowering their ratios to CD8$^+$ TILs (Figure 5J). αPDL-1 monotherapy selectively reduced non-cycTreg but did not significantly affect cycTreg. Only the dual regimen increased non-cycling CD8$^+$, typically associated with immunotherapeutic responses[22] (Figures S5K and S5L). Because non-Treg CD4$^+$ TILs also expressed OX40 (Figure 5C), their phenotypes were examined. αOX40-based therapies increased memory-like CD45RC$^+$ and IRF4$^+$ effector CD4$^+$ TILs, while reducing CTLA4 and ICOS expression, consistent with effector activation (Figures S5L–S5P). Treatment response (responders [R] vs. non-responders [NR]) did not alter the suppressive effects on cycTreg or ICOS^{hi} effector-like Treg, indicating that non-response was not due to insufficient Treg targeting (Figure S5Q).

To explore the cycling kinetics of Treg subpopulations, sequential EdU/BrdU dual pulse-chase labeling was conducted to establish the cycling dynamics of Treg subpopulations and reveal how they respond to immunotherapy. The dual-labeling timeline enabled the identification of Treg cycling states: actively cycling cycTreg (BrdU$^+$), recently divided non-cycTreg derived from cycTreg (EdU$^+$), and a rare EdU$^+$/BrdU$^+$ double-positive population that persisted in cycle for five days, representing long-lasting cycling precursors (Figure 5K, gating strategy shown in Table S3). Across treatment groups, 10%–15% of Ki67$^+$FOXP3$^+$ Treg were BrdU$^+$, and 10%–20% were EdU$^+$, confirming that the cycTreg state reflects actively or recently dividing Treg (Figure 5L). Approximately 1%–2% of Ki67$^+$FOXP3$^+$ cells were EdU$^+$/BrdU$^+$. Dual OX40/PD-L1 targeting significantly reduced EdU and BrdU incorporation (Figure 5L), indicating suppressed Treg cycling kinetics. In contrast, the Ki67^{neg}FOXP3$^+$ fraction showed minimal BrdU labeling (∼1%–2%) and almost no double-positive cells; most were EdU$^+$ or double-negative (Figure 5M), suggesting that the Treg had divided prior to the initial EdU pulsing and transitioned into mature, non-cycling state.

Linear regressions demonstrated a strong inverse correlation between cycTreg abundance and both CD8$^+$ and CD4$^+$ Tconv infiltration (Figure 5N), supporting our model in which cycTreg impede Tconv trafficking and promote immune escape. Two multivariable models incorporating BrdU$^+$Ki67$^+$FOXP3$^+$ (actively dividing Treg), EdU$^+$Ki67^{neg}FOXP3$^+$ (cycTreg-derived Treg), and treatment modality showed that all three variables independently predicted overall Treg burden (Figure S5R). However, predicting more complex outcomes such as tumor growth rate (%CGR) required interaction terms, either between Ki67$^+$ Treg and EdU$^+$ Ki67^{neg} or between Ki67$^+$ Treg and treatment modality (Figure S5S), indicating that both proliferative and post-cycling Treg states jointly shape tumor progression.

Transcriptomic landscape of therapeutic immunity and resistance to αOX40 and αPD-L1

Given the differential responses to αPD-L1 blockade, agonistic αOX40, and dual-targeting therapy, scRNA-seq profiling of treatment-naïve (isotype-treated, $n = 4$) and immunotherapy-treated tumors classified as R and NR ($n = 2$ per response/treatment) was performed to define mechanisms of therapeutic immunity and resistance. Louvain clustering identified five major compartments comprising luminal-like and basal-like cancer cells, T cells, myeloid cells, and CAFs (Figure 6A and Table S2), with high-resolution analysis revealing treatment- and response-specific subtype diversity (Figures 6A, 6B, and S6A). Dual-targeting NR tumors were enriched for *Birc5*^{hi} cycling cancer cells, whereas R tumors showed expanded LP-like cancer cells (Figure S6A). T cells most strongly distinguished R from NR tumors, with therapeutic efficacy marked by reduced cycTreg population and increased naive, cytotoxic, and Tpex CD8$^+$ populations (Figures 6B and S6B). Responders also displayed elevated monocyte-derived Macs (moMacs), while other TAM and cDC subsets remained largely comparable (Figures 6A and 6B).

Unsupervised clustering segregated tumors into αPD-L1/isotype and αOX40/dual-targeting branches, each sub-divided into R and NR (Figure 6C). Treatment-naïve tumors were enriched for Treg cycling genes (*Mki67* and *Top2a*), core transcription factors (*Foxp3*, *Ikzf2/4*, and *Batf*), and co-inhibitory receptors (*Ctla4*, *Lag3*, and *Tigit*), all of which diminished following immunotherapy (Figure S6B, top). Conversely, CD8$^+$ effector genes (*Nkg7*, *Prf1*, and *Gzmm*) and transcription factors (*Rora*, *Tbx21*, and *Btg2*) were highly upregulated after dual targeting (Figure S6B, bottom). Milo analysis showed that R tumors enriched for CD8$^+$ cytotoxic effector and IFN-responsive TIL neighborhoods, whereas treatment-naïve tumors were dominated by cycTreg and non-cycTreg states (Figure S6C). Pseudotime reconstruction revealed CD4$^+$ trajectory from cycTreg to naive Treg, culminating in memory-like or Th2-like states in responders (Figure S6D), while CD8$^+$ TILs transitioned from Tex to

(C) Hierarchical clustering of samples based on top 5% TIL variable features.
(D) Normalized enrichment scores of the "allograft rejection" hallmark based on treatment responses. Significance was computed by the Kruskal-Wallis test and Tukey's multiple comparison. Missing ridges indicate hallmark absence.
(E) UMAP plot of rat CAFs, with grouping by treatment response (inset).
(F) Milo beeswarm plot of CAF neighborhoods between R ($n = 6$) and NR ($n = 6$). Color gradient indicates DA at FDR 10% significantly skewed toward R vs. NR.
(G) Trajectory of CAFs. Isotype control was set as pseudotime root. Dotted green lines show trajectory toward R phenotype.
(H) Quantified CD34$^+$-to-tumor area ratio following OX40/PD-L1 immunotherapy (n = 3–10 tumors). Significance was computed by two-way ANOVA categorized by treatment response. Comparisons among R, NR, and isotype were performed by Kruskal-Wallis test.
(I and J) UMAP plot (I) and stack bar plot (J) of rat CAFs, with grouping by DCIS progression (inset). Asterisks denote significant overrepresentation of specified subtypes.
(K) CellChat-inferred outgoing and incoming communications in treatment-naïve tumors.
See also Figure S6 and Table S2.

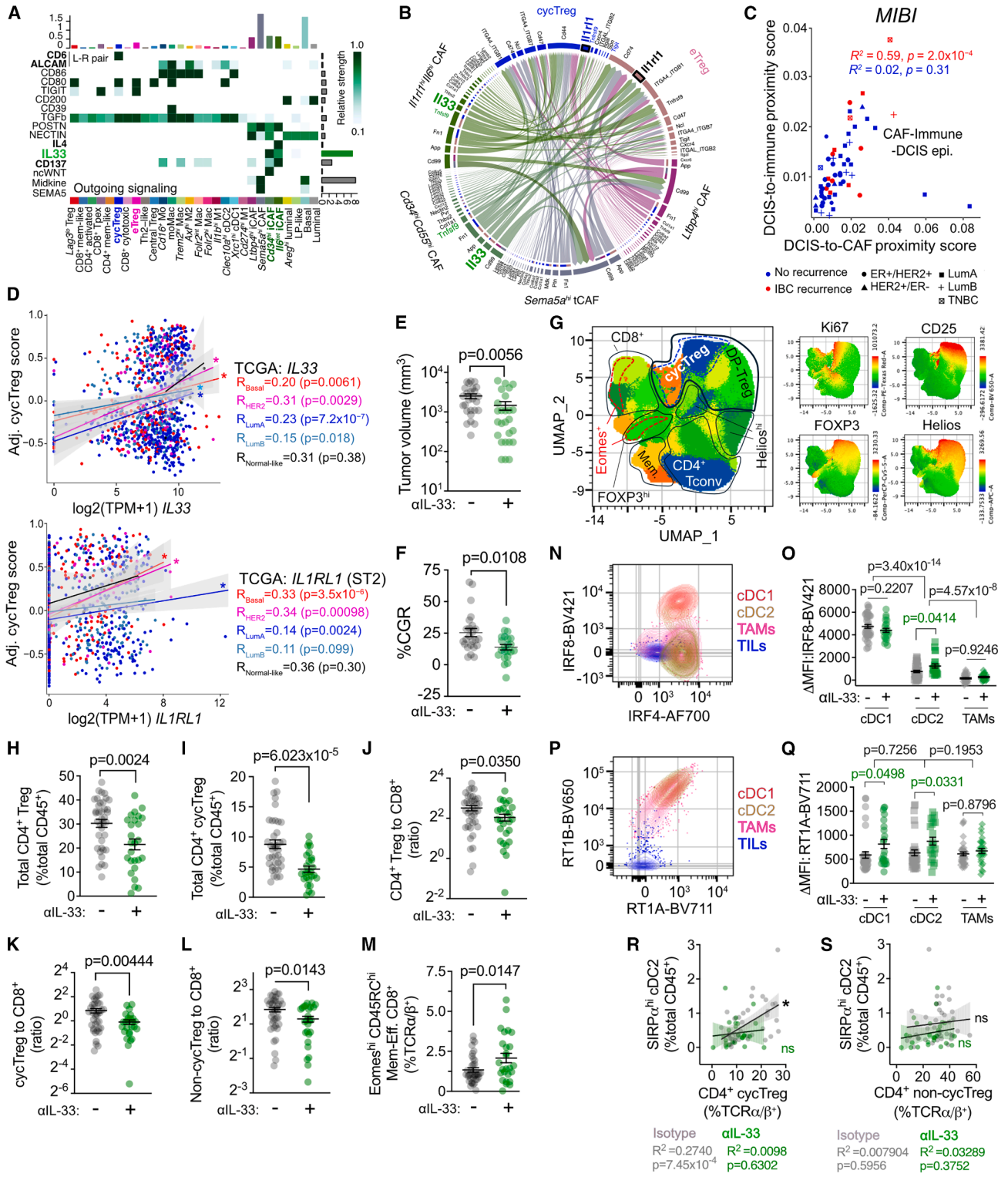

Figure 7. IL-33 and intratumoral retention of cycTreg

(A and B) CellChat heatmap of outgoing signaling in treatment-naïve tumors (A) (FDR <0.05) and chord diagram (B) inferring *Il33* (green) from CAFs to *Il1rl1* (blue, encoding ST2) on cycTreg and eTreg.

(C) Pearson's correlations of proximity scores from MIBI dataset of DCIS epithelium edge to CD45⁺ immune cells and to CAFs. Best-fit R^2 was computed based on recurrence diagnosis. Each dot represents individual DCIS patients (n = 55) with follow-up for IBC recurrence (red, n = 14) or lack thereof (blue, n = 41).

(D) Linear regression of adjusted cycTreg score with *IL33* (top) and *IL1RL1* (bottom) expression from TCGA dataset (n = 992 patients).

(legend continued on next page)

memory-like and Tpex states (Figure S6E), Given the prominence of CD8$^+$ activity, the "hallmark of allograft rejection"[23–25] was quantified, showing increased enrichment in both monotherapies and strongest induction under dual targeting (Figure 6D, all "hallmarks" in Table S2). Myeloid analysis delineated heterogeneous TAM, moMac, and cDC states (Figure S6F), with pseudotime analysis revealing branching from *Cd14*^{hi}/*Cd16*^{hi} monocytes toward terminal cDC1-3 states highly expanded in responders (Figure S6G). Milo analysis showed R-enriched *Trem2*^{hi} TAMs and *Irf8*^{hi} cDC1, whereas NR tumors contained MHC-II^{hi} TAMs, and treatment-naive tumors displayed elevated M2-like TAMs (Figure S6H).

Immunotherapeutic sensitivity is marked by inflammatory CAFs

Among all lineages, CAFs most robustly distinguished immune-responsive from immune-resistant tumors (Figure 6E). Treatment-naïve tumors contained *Sema5a*^{hi} tumor-like CAFs (tCAFs).[26,27] Immune sensitivity shifted the stroma toward *Ltbp4*^{hi} and *Cd34*^{hi} inflammatory subsets (iCAFs) (Figures S6I and S6J), whereas resistance favored *Il1rl1*^{hi} *Il6*^{hi} iCAFs (Figures 6E and S6J). Milo analysis separated iCAF-enriched R tumors from NR and naive tumors enriched for *Tnfsf9* and *Il33* (Figures 6F and S6K). Pseudotime revealed branching toward *Ltbp4*^{hi} or *Cd34*^{hi} CAFs featuring therapeutic response (Figures 6G and S6L). Multiplexed immunofluorescence confirmed increased CD34$^+$ stroma in responders (Figure 6H), and *Cd34*^{hi}*Il33*$^{hi/int}$ iCAFs in DCIS-like microlesions linked iCAF program to early tumor stages (Figures 6I and 6J).

Interleukin 33 sustains cycTreg pool and immune escape

In treatment-naïve rat tumors, spatial proximities among iCAFs, Treg, and CD8$^+$ TILs suggested dynamic interactions and potential CAF-to-TIL crosstalk (Figure S6O). To identify key signaling sources and targets within this immune-escaped hub, CellChat analysis quantified incoming and outgoing communication strengths. CAFs emerged as the dominant signal senders, whereas myeloid cells received the highest inputs (Figure 6K). Among top pathways communicated by iCAFs was interleukin 33 (IL-33), a nuclear cytokine[28] (Figure 7A). Enhanced CAF communicability was most pronounced in responders following dual targeting (Figure S7A). Additional proliferative pathways (Alcam-Cd6 and Tnfsf9/CD137), though weaker, were transmitted from myeloid cells to cycTreg (Figure 7A). Alongside Tnfsf9/CD137[29] and IL-4,[30] the IL-33/ST2 axis is well established in promoting Treg proliferation, differentiation, and immune escape.[31] IL-33 signals were predominantly sent from *Cd34*^{hi} or *Il6*^{hi} iCAFs to Treg subtypes across treatment regimens, with minimal contribution from other lineages (Figure S7B). Ligand-receptor analysis confirmed robust IL-33 signaling from these iCAFs to ST2 (*Il1rl1*) on cycTreg and eTreg (Figure 7B).

To dissect IL-33 signaling, IL-1 superfamily (IL-1α, IL-1β, IL-18, and IL-33) was quantified across a deeply annotated communication atlas of rat macroscopic tumors and microlesions (Figure S7C). In microlesions, CAF subtypes (iCAFs, tCAFs, and myofibroblasts) acted as dominant senders, whereas in macroscopic tumors, strong IL-33 transmission was restricted to *Il33*^{hi} iCAFs, and tCAFs (Figure S7D). High-intensity IL-33 output was iCAF specific, with exclusive ST2-mediated reception in cycTreg, non-cycTreg, and Th2-Treg, where ST2 expression was amplified in macroscopic tumors (Figure S7E). Innate lymphoid cell type 3 (ILC3) also exhibited ST2-mediated reception, particularly in microlesions (Figure S7E). Visium mapping revealed localized or widespread *Il33* expression in macroscopic tumors, contrasting with low, dispersed expression in normal MGs (Figure S7F and Table S3).

To assess clinical relevance, CAF-immune proximities were analyzed in pure DCIS, using the HTAN (Human Tumor Atlas Network) MIBI (Multiplex Ion Beam Imaging) dataset.[32] Across molecular subtypes, proximity between DCIS epithelium, immune cells, and FAP$^+$ CAFs strongly correlated with later IBC recurrence (Figure 7C). Similar correlations were observed for CAF and CD3$^+$ TIL proximity to DCIS epithelium (Figure S7G). High-risk DCIS showed increased proximity to FAP$^+$ CAFs, CD45$^+$, CD4$^+$ TILs, and CD11c$^+$/HLA-DR$^+$ DCs (Figure S7H). In the human scRNA-seq atlas, IL-33 enrichment was validated in tCAFs and iCAFs, with both being differentially abundant between DCIS and IBC (Figure S7I). Strong correlations between cycTreg scores and *IL33* or *IL1RL1* (ST2) expression across PAM50 subtypes of TCGA IBC reinforced IL-33's role in sustaining cycTreg burden (Figure 7D). In treatment-naïve rats, intracellular IL-33 was detected in CAFs, tumor epithelium, and immune cells as CAFs showed the highest IL-33$^+$ frequency (Figure S7J, gating in Table S3). IL-33$^+$ CAF abundance correlated specifically with cycTreg, but not non-cycTreg (Figure S7K), suggesting selective IL-33-driven expansion of cycTreg.

To define IL-33's functional role, iTreg generated from rat PBMCs or LN-sorted CD3$^+$ T cells were conditioned with escalated doses of recombinant IL-33 (rIL-33) (Figures S7L–S7Q). PBMC-derived iTreg rapidly progressed to later division across all doses (Figure S7M), whereas LN-derived iTreg showed enhanced division (D4+) at higher IL-33 concentrations (Figure S7N). Non-activated iTreg lacking CD3ε/CD28 co-stimulation failed to respond, indicating TCR-dependent IL-33 responsiveness. In human naive CD45RA$^+$ CD4$^+$ T cells

(E and F) Tumor volumes (E) and % CGR (F) computed at tumor endpoints (isotype: $n = 26$; αIL-33: $n = 26$). Tumors with < 7 days of *in vivo* growth were excluded. Significance was computed using two-tailed Mann-Whitney U test.
(G) UMAP plot of 29 TIL clusters inferred by Phenograph. Heatmap insets show scaled fluorescence values.
(H–M) Quantification of total CD4$^+$ FOXP3$^+$ Treg (H), cycTreg (I), ratios of total Treg (J), cycTreg (K), and non-cycTreg (L) to total CD8$^+$, and Eomes^{hi} CD45RC^{hi} memory-effector CD8$^+$ T cells (M).
(N–Q) Contours of IRF8/IRF4 (N) and RT1B/RT1A (P) and quantified myeloid IRF8 (O) and RT1A (MHC-I) (Q) of intratumor cDC1, cDC2, TAMs, and TILs.
(R and S) Pearson's correlations of cDC2 with cycTreg (R) and non-cycTreg (S) following αIL-33 blocking. Pearson's best-fit parameters including R^2, significance, and 95% CI are shown. For αIL-33 study, individual tumors are shown (isotype: $n = 38$; αIL-33: $n = 26$ tumors).
Significance of two-group comparisons (E, F, and H–M) was computed by two-tailed Student's *t* test. Significance of multiple group comparisons (O and Q) was computed by two-way ANOVA and Sidak's multiple comparison.
See also Figure S7 and Table S3.

Please cite this article in press as: Bui et al., Identification of cycling regulatory T cell precursors as conductors of immune escape during breast carcinoma progression, Cancer Cell (2026), https://doi.org/10.1016/j.ccell.2026.03.015

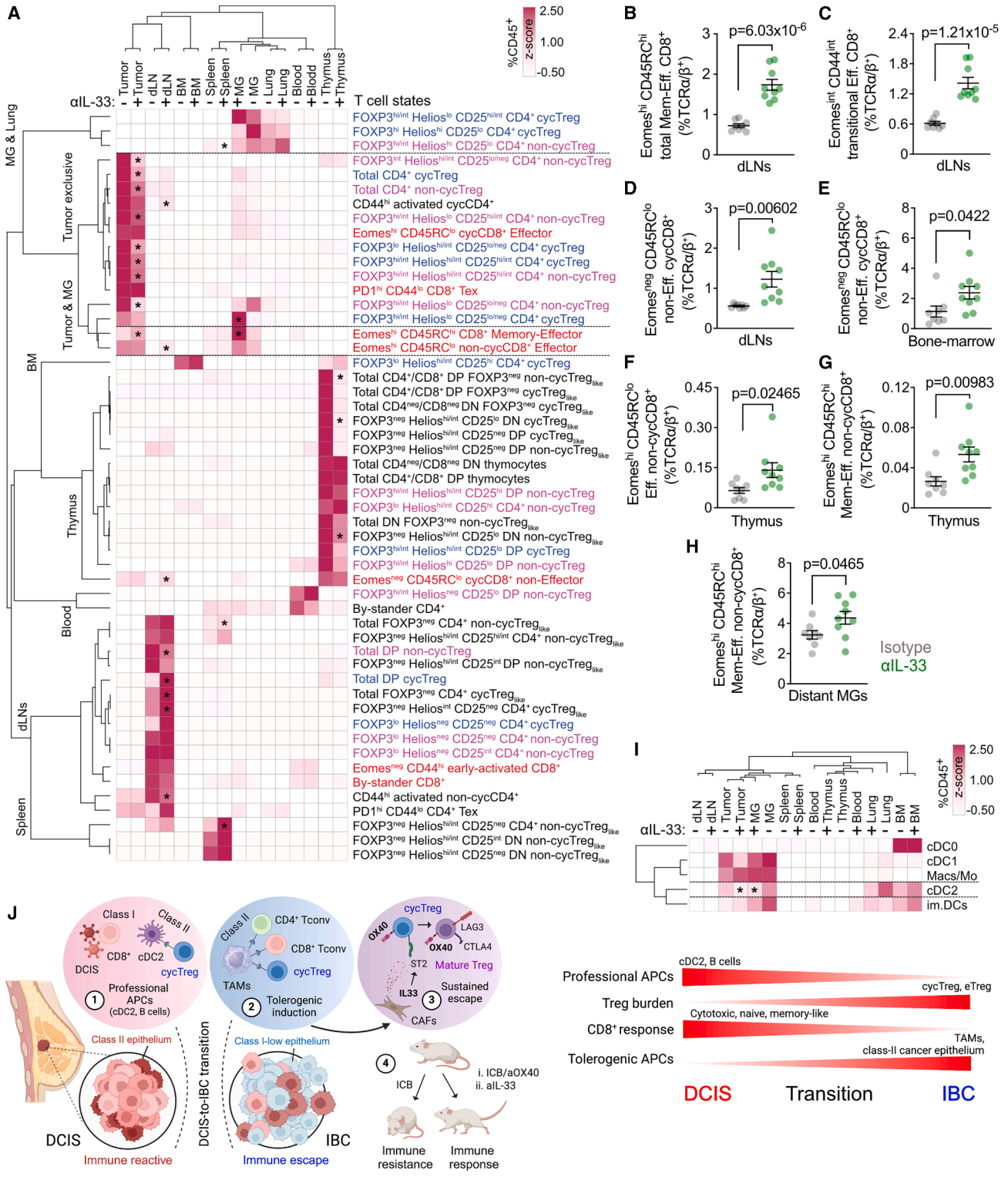

Figure 8. Local and systemic effects of IL-33 neutralization

(A) Heatmap showing hierarchical clustering of T cells with/without αIL-33 neutralization (isotype: $n = 8$; αIL-33: $n = 9$ rats). Dotted lines demarcate decreased Treg subtypes and increased memory-effector CD8$^+$ by αIL-33.

(B–H) Pairwise comparisons of total memory-effector (B), transitional effector (C), and non-effector CD8$^+$ in tumor-draining LNs (D), non-effector cycling CD8$^+$ in bone marrow (E), effector (F), and memory-effector CD8$^+$ in thymus (G), and memory-effector CD8$^+$ in distant, healthy MGs (H) (isotype: $n = 8$; αIL-33: $n = 9$ rats). Significance was computed by two-tailed Student's t test.

(legend continued on next page)

differentiated into iTreg, IL-33 increased IL-10 and suppressed TNF-α (Figures S7O–S7Q), demonstrating IL-33-mediated anti-inflammatory polarization. ST2 blockade by astegolimab reduced IL-10 and partially restored TNF-α. These effects were reversed by high-dose IL-33, confirming requirement for intact IL-33/ST2 signaling.

To mechanistically link IL-33 to cycTreg burden *in vivo*, αIL-33 monoclonal antibody (mAb)was administered at tumor onset. This mAb was shown to inhibit IL-33/ST2 signaling in rodent models.[33,34] IL-33 neutralization significantly reduced tumor burden, slowed growth, and shifted tumors toward stabilized or regressing phenotypes without altering tumor numbers per rat (Figures 7E, 7F, and S8A–S8D). Phenograph analysis[35] identified 29 TIL phenotypes (Figures 7G and S8E), where αIL-33 reduced overall TIL infiltration due to marked decreases in total Treg, while $CD8^+$ and $CD4^+$ Tconv remained unchanged (Figures 7H and S8F–S8H). cycTreg were robustly suppressed (~2-fold reduction), accompanied by modest decrease in non-cycTreg (Figures 7I and S8I). Ratios of Treg subsets to $CD8^+$ TILs were significantly reduced (Figures 7J–7L), paralleling immunoresponse achieved with αOX40/αPD-L1 dual targeting (Figure 5J). Reduced Treg subpopulations enabled the infiltration of $CD8^+$ TILs enriched for Eomes (Figure 7M), a transcription factor marking antigen-experienced effector phenotypes.[36,37] cycTreg exhibited higher IL-10 than non-cycTreg or Tconv (Figure S8J), underscoring their suppressive potency and the therapeutic benefit of reducing their abundance.

IL-33 neutralization limits cDC2 lineage and increases pan-DC's MHC class I

αIL-33 induced selective myeloid composition shifts, leaving total myeloid and mature cDC numbers unchanged (Figures S8K and S8L). cDC2 upregulated IRF8, a transcription factor marking cDC1 (Figures 7N and 7O), indicating IL-33's role in maintaining cDC2 identity. IRF4, a pan-myeloid regulator linked to moDCs[38] and M2 polarization,[39] remained stable (Figure S8M). In TAMs, both IRF4 and IL-10 were markedly reduced (Figures S8M and S8N), reflecting a shift away from M2-associated program. While MHC class II remained stable, MHC class I was elevated in cDC1 and cDC2, featuring enhanced cross-presentation potential to $CD8^+$ TILs[40] (Figures 7P, 7Q, and S8O). αIL-33 disrupted the positive cDC2-cycTreg relationship in treatment-naïve tumors with no association between cDC2 and non-cycTreg (Figures 7R and 7S). cDC2 abundance also inversely correlated with $CD8^+$ TILs (Figure S8P). cDC-based tumor stratification revealed that cDC2-low tumors were more immunologically reactive, as αIL-33 suppressed cycTreg and preferentially expanded memory-effector over early-effector states (Figures S8Q–S8S).

IL-33 neutralization invigorates local and systemic immunosurveillance

Neutralization of IL-33 produced coordinated regional and systemic immune effects across secondary and primary lymphoid organs. αIL-33 selectively inhibited intratumoral Treg subsets, with minimal impact on peripheral Treg (Figures 7I, S8I, and S8T). In tumor-dLNs and spleens, αIL-33 induced $FOXP3^{neg}$ Treg-like cells ($Helios^{int/lo}CD25^{lo/neg}$), resembling ex-Treg states observed during ICB (Immune Checkpoint Blockade) responses,[41] suggesting that αIL-33 destabilizes FOXP3 and impairs Treg differentiation (Figures S8U and S8V). High-dimensional profiling across tumors, distant MGs, lungs, and five lymphoid organs identified 35 clusters spanning Treg, memory, effector, and exhausted states (Figure S8W). Unsupervised clustering grouped T cells by the tissue of origin, indicating that organ context outweighed treatment in shaping T cell heterogeneity (Figure 8A). Five phenotypic domains emerged: tumors (cycTreg, non-cycTreg, and effector), distant MGs/lungs (memory-effector), dLNs (cycTreg-like), spleen, and thymus (non-cycTreg-like).

αIL-33 exerted its strongest effects in tumors and dLNs, reducing Treg subsets while expanding $FOXP3^{neg}$ cycTreg-like and non-cycTreg-like populations in dLNs (Figure 8A). Concurrently, αIL-33 increased $Eomes^+$ memory-effector, transitional effectors, and non-effector $CD8^+$ T cells, supporting regional immunosurveillance (Figures 8B–8D). In primary lymphoid organs, αIL-33 induced an $Eomes^{neg}$ $cycCD8^+$ response in bone marrow, while thymus showed increased production of $Eomes^+$ effector and memory-effector $CD8^+$ T cells (Figures 8E–8G). These changes coincided with surveillance of distant MGs by antigen-experienced memory-effector T cells (Figure 8H).

Systemic myeloid profiling showed that myeloid states segregated by tissues, rather than treatment (Figures 8I and S8X). However, αIL-33 reduced $SIRP\alpha^{hi}$ cDC2 in tumors and distant MGs (Figure 8I). Deep profiling of $CD103^+$ cDCs revealed strong location-based grouping, with intratumoral cDCs expressing the highest IRF8 and IRF4 levels (Figure S8Y). αIL-33 downregulated IRF4 in tumor-resident and circulating DCs, while increasing MHC class I across DCs residing in the tumors, MGs, and lungs (Figures S8Y and S8Z).

These findings demonstrated that IL-33 acts as a negative regulator of $CD8^+$ effector immunity and that its neutralization amplifies immune control across micro and macroenvironments of breast tumors. Key experimental workflow and major findings of the study are summarized in Figure S9.

DISCUSSION

The DCIS-to-IBC transition is a pivotal step in breast tumor evolution.[1] Prior work has shown extensive remodeling across epithelial and immune compartments during this progression,[42,43] with a shift from immune-reactive DCIS to immune-escaped IBC.[2,44] To resolve the mechanisms underlying this transition, we integrated four human scRNA-seq datasets (72 DCIS, IBC, and normal breast samples) alongside four single-cell and spatial transcriptomic datasets from SD rats, complemented by bulk RNA-seq and imaging-based profiling. This

(I) Heatmap showing hierarchical clustering of myeloid cells across all 8 tissue locations with/without αIL-33. Dotted lines demarcate cDC2 altered by αIL-33.
(J) Schematic of immune escape during DCIS-to-IBC transition, as created with BioRender.com.
In (A) and (I), color gradients represent *Z* score of each %T cell (A) or myeloid cell (I), scaled across 8 tissue locations. Significance was computed by two-tailed Student's *t* test and is shown on heatmap as asterisks.
See also Figures S8 and S9 and Table S3.

cross-species framework enabled high-resolution mapping of Treg heterogeneity and identification of cycTreg as a key biomarker and immuno-oncology target in DCIS and IBC.

Although cycling CD4$^+$ T cells have been previously described,[11,41,45,46] their functional roles remain poorly defined. Their proliferative phenotype likely reflects antigen-driven priming by APCs, particularly cDC2 via class II-restricted antigen presentation.[15,47] In tumors with high neoantigen loads, CD4$^+$ Tconv and Treg may be stimulated by HLA class II-expressing epithelium.[15] Pseudotime analyses revealed that cycTreg emergence coincides with cDC2 enrichment at the DCIS-to-IBC transition, suggesting a mechanistic link. This relationship is supported by spatial proximity between CLEC10A$^+$ cDC2 and cycTreg in DCIS and IBC, with the strongest association in TN IBC. Rat tumors with elevated cDC2/cDC1 ratios exhibited cycTreg enrichment, and *ex vivo* assays demonstrated that tumor-derived cDC2 uniquely promoted Treg division through immune synapse-dependent mechanisms.

We identify *TNFRSF4*/OX40 as a central regulatory node in human and rat Treg, with the highest expression in cycTreg and effector-like Treg subsets, consistent with previous characterization of OX40^{hi} GITR^{hi} Treg.[41] OX40 co-stimulation enhances memory programs in CD4$^+$ Tconv and boosts CD8$^+$ effector responses,[48–51] while destabilizing FOXP3$^+$ Treg through BATF3/BAFT-mediated recruitment to the *Foxp3* locus and Sirt1/7-dependent repression.[52] OX40 signaling also reduces IL-10 production and weakens Treg-mediated CD8$^+$ suppression.[53,54] Although OX40 agonists have shown limited monotherapy efficacy in metastatic tumors (NCT02923349),[55] our rat studies demonstrate that combining OX40 agonist with αPD-L1 attenuates cycTreg and effector-like Treg, while sparing cycling CD4$^+$ and CD8$^+$. Responding tumors exhibited a shift from the tCAF state to the inflammatory iCAF state,[26,27] indicating stromal remodeling as part of therapeutic response.

Across four clinical cohorts,[18,19,32,56,57] cycTreg signature predicted CD8$^+$ infiltration, TCR diversity, cDC1, disease-specific survival, and DCIS recurrence. cycTreg was the only immune subset associated with recurrence in grade 1 DCIS, suggesting its utility for risk stratification. In IBC, cDC2 strongly predicted cycTreg levels, consistent with cDC2-driven antigen presentation as a key driver of cycTreg expansion.

Transcriptomic analyses revealed Treg-CAF interactions and IL-33/ST2 signaling as additional axes sustaining cycTreg. Tricellular proximity among CAFs, DCIS epithelium, and TILs correlated with IL-3 signaling, a pathway known to promote Treg expansion via IL-33/ST2 engagement[33,58,59] or indirectly via AREG-EGFR[60] or canonical Wnt activation.[61]

These findings map Treg heterogeneity across human and rat breast tumors and identify cDC2-driven TIL priming and IL-33-mediated stromal signaling as central mechanisms sustaining cycTreg during DCIS-to-IBC transition (Figure 8J).

Limitations of the study

cDC2 drive Treg proliferation through TCR/MHC class II synapse.[62] Selective cDC2 depletion remains technically unachievable,[62,63] as existing DC-deficient models target cDC1 or incompletely disrupt cDC2 while affecting CD4$^+$ lineage.[64] Because cycTreg differ at the transcription factor level, viable isolation for functional studies is not feasible; therefore, proliferative dLN-derived iTreg were used as surrogates. Future transgenic rats with cell cycle tracking will define cycTreg mechanisms, and stepwise dissection of CAF-cDC2-cycTreg interactions remains an important goal.

RESOURCE AVAILABILITY

Lead contact

Further information and requests for resources and reagents should be directed to and will be fulfilled by the lead contact, Kornelia Polyak (kornelia_polyak@dfci.harvard.edu).

Materials availability

Materials and reagents are available from the lead contact upon reasonable request. This paper did not generate unique reagents.

Data and code availability

All data needed to evaluate the conclusions in the paper are present in the paper and/or its supplemental information. All raw data were deposited directly to the Sequence Read Archive (SRA) under the SuperSeries BioProject PRJNA1062792. Processed genomic data were deposited to GEO under accession number: GSE253587 with SRA accession numbers corresponding to BioProject PRJNA1062792. This study did not generate custom code.

ACKNOWLEDGMENTS

We thank R. Bhargava, G. Carter, L. Miller, C. Kline, N. Roehrig, H. Havrilla, C. Mongelli, J. Tarr, and A. Madison for collection of human samples at the UPMC Hillman Cancer Center and Tissue and Research Pathology/Pitt Biospecimen Core shared resource, supported by P30CA047904. We thank the DFCI Molecular Biology Core Facility for their sequencing service, Dr. Kun Huang of the Molecular Imaging Core Facility for her advice and support, Dr. Gordon Freeman for providing αPD-L1/αPD-1 antibodies, and the Agudo laboratory for providing protocols and reagents. This work utilized an Illumina NovaSeq X Plus that was purchased with funding from an NIH SIG grant 1S10OD036228-01. This research was supported by NCI CA17035 (E.S.H., R.B.W., K.P., G.A.C., and M.A.), CA236754 (T.M.B.), CA197623 (K.P.), CA274597 (K.A.P.), Charles King Foundation (Z.L.), Susan G. Komen Foundation (J.N.), Belgian American Educational Foundation (P.F.), Wallonie-Bruxelles International (P.F.), Télévie Foundation (P.F.), FE (P.F.), the Susan Smith Breast and Gynecologic Award GFE0005434 (T.M.B.), and the Breast Cancer Research Foundation (K.P.).

AUTHOR CONTRIBUTIONS

Conceptualization, T.M.B. and K.P.; methodology, T.M.B.; formal analysis, T.M.B., Z.L., E.R.J, A.J., L.Y., X.Q., S.C., and K.A.P.; investigation, T.M.B., J.P., E.R.J., P.F., P.Y., J.N., M.S., X.-Y.H., A.P., X.C., and O.S.; resources, C.H.M.III, D.D., R.R., S.J., J.R.M., C.B., D.D.B., S.Y.P., A.V.L., P.F.M., S.H.S., K.B., R.W., M.A., G.A.C., E.S.H., and G.D.; writing – original draft, T.M.B. and K.P.; writing – review & editing, all authors; funding acquisition, E.S.H. and K.P. All authors helped design the study and write the manuscript.

DECLARATION OF INTERESTS

K.P. serves on the Scientific Advisory Board of Ideaya Biosciences, is an adviser to Curie.Bio, holds equity in Antares Therapeutics and stock options in Ideaya Biosciences, received funding from Novartis and honoraria from Astra-Zeneca and Novartis, and received payment from Eli Lilly for Scorpion Biosciences purchase. T.M.B. is a shareholder of Merck, Eli Lilly, Novo Nordisk, AbbVie, and Johnson & Johnson. C.H.M.III. is a consultant to Grail. D.D. receives funding from Canon, Inc. M.A. is board member and shareholder in IonPath Inc. A.V.L. reports stock or other ownership/honoraria at Ocean Genomics and Almaden Genomics. G.D. reports stock ownership in Novartis. E.S.H. is a consultant to Merck, Astra Zeneca, and Beckton Dickinson and is a shareholder in Havah Therapeutics. J.P. and P.Y. are currently employees

of Glaxo Smith Klein (GSK), PA, USA, and they contributed to this work prior to employment at GSK; the perspectives expressed herein do not represent those of GSK.

STAR★METHODS

Detailed methods are provided in the online version of this paper and include the following:

- KEY RESOURCES TABLE
- EXPERIMENTAL MODEL AND STUDY PARTICIPANT DETAILS
  - Patient specimens from multiple clinical cohorts
  - Animals
- METHOD DETAILS
  - *In vivo* experiments in outbred NMU-induced Sprague-Dawley rats
  - Tissue dissociation and fluorescent-activated cell sorting (FACS)
  - *Ex vivo* induction of iTreg and co-culture with autologous DC subsets
  - *Ex vivo* conditioning of human and rat iTreg by IL-33
  - Histology evaluation
  - Immunofluorescence, wide-field scanning, and confocal microscopy
  - High-dimensional immune profiling by flow cytometry
  - scRNA-seq library construction, illumina sequencing, and 10X cell ranger outputs
  - scRNA-seq data processing pipelines
  - 10X visium spatial transcriptomic processing and data analysis
  - Public RNA-seq and proteomic analyses
- QUANTIFICATION AND STATISTICAL ANALYSIS
  - Statistical analyses

SUPPLEMENTAL INFORMATION

Supplemental information can be found online at https://doi.org/10.1016/j.ccell.2026.03.015.

Received: March 20, 2025
Revised: February 2, 2026
Accepted: March 23, 2026

REFERENCES

1. Casasent, A.K., Almekinders, M.M., Mulder, C., Bhattacharjee, P., Collyar, D., Thompson, A.M., Jonkers, J., Lips, E.H., van Rheenen, J., Hwang, E.S., et al. (2022). Learning to distinguish progressive and non-progressive ductal carcinoma in situ. Nat. Rev. Cancer *22*, 663–678. https://doi.org/10.1038/s41568-022-00512-y.
2. Gil Del Alcazar, C.R., Huh, S.J., Ekram, M.B., Trinh, A., Liu, L.L., Beca, F., Zi, X., Kwak, M., Bergholtz, H., Su, Y., et al. (2017). Immune Escape in Breast Cancer During In Situ to Invasive Carcinoma Transition. Cancer Discov. *7*, 1098–1115. https://doi.org/10.1158/2159-8290.CD-17-0222.
3. Trinh, A., Gil Del Alcazar, C.R., Shukla, S.A., Chin, K., Chang, Y.H., Thibault, G., Eng, J., Jovanović, B., Aldaz, C.M., Park, S.Y., et al. (2021). Genomic Alterations during the In Situ to Invasive Ductal Breast Carcinoma Transition Shaped by the Immune System. Mol. Cancer Res. *19*, 623–635. https://doi.org/10.1158/1541-7786.MCR-20-0949.
4. Gil Del Alcazar, C.R., Trinh, A., Alečković, M., Rojas Jimenez, E., Harper, N.W., Oliphant, M.U.J., Xie, S., Krop, E.D., Lulseged, B., Murphy, K.C., et al. (2022). Insights into Immune Escape During Tumor Evolution and Response to Immunotherapy Using a Rat Model of Breast Cancer. Cancer Immunol. Res. *10*, 680–697. https://doi.org/10.1158/2326-6066.Cir-21-0804.
5. Blanco-Heredia, J., Souza, C.A., Trincado, J.L., Gonzalez-Cao, M., Gonçalves-Ribeiro, S., Gil, S.R., Pravdyvets, D., Cedeño, S., Callari, M., Marra, A., et al. (2024). Converging and evolving immuno-genomic routes toward immune escape in breast cancer. Nat. Commun. *15*, 1302. https://doi.org/10.1038/s41467-024-45292-1.
6. Tietscher, S., Wagner, J., Anzeneder, T., Langwieder, C., Rees, M., Sobottka, B., de Souza, N., and Bodenmiller, B. (2023). A comprehensive single-cell map of T cell exhaustion-associated immune environments in human breast cancer. Nat. Commun. *14*, 98. https://doi.org/10.1038/s41467-022-35238-w.
7. Klopfenstein, Q., Derangère, V., Arnould, L., Thibaudin, M., Limagne, E., Ghiringhelli, F., Truntzer, C., and Ladoire, S. (2021). Evaluation of tumor immune contexture among intrinsic molecular subtypes helps to predict outcome in early breast cancer. J. Immunother. Cancer *9*, e002036. https://doi.org/10.1136/jitc-2020-002036.
8. Pal, B., Chen, Y., Vaillant, F., Capaldo, B.D., Joyce, R., Song, X., Bryant, V.L., Penington, J.S., Di Stefano, L., Tubau Ribera, N., et al. (2021). A single-cell RNA expression atlas of normal, preneoplastic and tumorigenic states in the human breast. EMBO J. *40*, e107333. https://doi.org/10.15252/embj.2020107333.
9. Qin, X., Strand, S.H., Lee, M.R., Saraswathibhatla, A., van lJzendoorn, D.G.P., Zhu, C., Vennam, S., Varma, S., Hall, A., Factor, R.E., et al. (2025). Single-Cell Expression Analysis of Ductal Carcinoma In Situ Identifies Complex Genotypic-Phenotypic Relationships Altering Epithelial Composition. Cancer Res. *85*, 2302–2319. https://doi.org/10.1158/0008-5472.CAN-24-3023.
10. Tokura, M., Nakayama, J., Prieto-Vila, M., Shiino, S., Yoshida, M., Yamamoto, T., Watanabe, N., Takayama, S., Suzuki, Y., Okamoto, K., et al. (2022). Single-Cell Transcriptome Profiling Reveals Intratumoral Heterogeneity and Molecular Features of Ductal Carcinoma In Situ. Cancer Res. *82*, 3236–3248. https://doi.org/10.1158/0008-5472.CAN-22-0090.
11. Chu, Y., Dai, E., Li, Y., Han, G., Pei, G., Ingram, D.R., Thakkar, K., Qin, J.J., Dang, M., Le, X., et al. (2023). Pan-cancer T cell atlas links a cellular stress response state to immunotherapy resistance. Nat. Med. *29*, 1550–1562. https://doi.org/10.1038/s41591-023-02371-y.
12. Dann, E., Henderson, N.C., Teichmann, S.A., Morgan, M.D., and Marioni, J.C. (2022). Differential abundance testing on single-cell data using k-nearest neighbor graphs. Nat. Biotechnol. *40*, 245–253. https://doi.org/10.1038/s41587-021-01033-z.
13. Yi, H., Plotkin, A., and Stanley, N. (2024). Benchmarking differential abundance methods for finding condition-specific prototypical cells in multi-sample single-cell datasets. Genome Biol. *25*, 9. https://doi.org/10.1186/s13059-023-03143-0.
14. Andreatta, M., Corria-Osorio, J., Müller, S., Cubas, R., Coukos, G., and Carmona, S.J. (2021). Interpretation of T cell states from single-cell transcriptomics data using reference atlases. Nat. Commun. *12*, 2965. https://doi.org/10.1038/s41467-021-23324-4.
15. Schuijs, M.J., Hammad, H., and Lambrecht, B.N. (2019). Professional and 'Amateur' Antigen-Presenting Cells In Type 2 Immunity. Trends Immunol. *40*, 22–34. https://doi.org/10.1016/j.it.2018.11.001.
16. Cancer Genome Atlas Network (2012). Comprehensive molecular portraits of human breast tumours. Nature *490*, 61–70. https://doi.org/10.1038/nature11412.
17. Cao, J., Spielmann, M., Qiu, X., Huang, X., Ibrahim, D.M., Hill, A.J., Zhang, F., Mundlos, S., Christiansen, L., Steemers, F.J., et al. (2019). The single-cell transcriptional landscape of mammalian organogenesis. Nature *566*, 496–502. https://doi.org/10.1038/s41586-019-0969-x.
18. Strand, S.H., Rivero-Gutiérrez, B., Houlahan, K.E., Seoane, J.A., King, L.M., Risom, T., Simpson, L.A., Vennam, S., Khan, A., Cisneros, L., et al. (2022). Molecular classification and biomarkers of clinical outcome in breast ductal carcinoma in situ: Analysis of TBCRC 038 and RAHBT cohorts. Cancer Cell *40*, 1521–1536.e7. https://doi.org/10.1016/j.ccell.2022.10.021.
19. Danenberg, E., Bardwell, H., Zanotelli, V.R.T., Provenzano, E., Chin, S.F., Rueda, O.M., Green, A., Rakha, E., Aparicio, S., Ellis, I.O., et al. (2022). Breast tumor microenvironment structures are associated with genomic

features and clinical outcome. Nat. Genet. *54*, 660–669. https://doi.org/10.1038/s41588-022-01041-y.

20. Valzasina, B., Guiducci, C., Dislich, H., Killeen, N., Weinberg, A.D., and Colombo, M.P. (2005). Triggering of OX40 (CD134) on CD4(+)CD25+ T cells blocks their inhibitory activity: a novel regulatory role for OX40 and its comparison with GITR. Blood *105*, 2845–2851. https://doi.org/10.1182/blood-2004-07-2959.
21. Talkington, A., and Durrett, R. (2015). Estimating Tumor Growth Rates In Vivo. Bull. Math. Biol. *77*, 1934–1954. https://doi.org/10.1007/s11538-015-0110-8.
22. Prokhnevska, N., Cardenas, M.A., Valanparambil, R.M., Sobierajska, E., Barwick, B.G., Jansen, C., Reyes Moon, A., Gregorova, P., delBalzo, L., Greenwald, R., et al. (2023). CD8(+) T cell activation in cancer comprises an initial activation phase in lymph nodes followed by effector differentiation within the tumor. Immunity *56*, 107–124.e5. https://doi.org/10.1016/j.immuni.2022.12.002.
23. Costa Svedman, F., Das, I., Tuominen, R., Darai Ramqvist, E., Höiom, V., and Egyhazi Brage, S. (2022). Proliferation and Immune Response Gene Signatures Associated with Clinical Outcome to Immunotherapy and Targeted Therapy in Metastatic Cutaneous Malignant Melanoma. Cancers (Basel) *14*, 3587. https://doi.org/10.3390/cancers14153587.
24. Oshi, M., Patel, A., Wu, R., Le, L., Tokumaru, Y., Yamada, A., Yan, L., Matsuyama, R., Ishikawa, T., Endo, I., and Takabe, K. (2022). Enhanced immune response outperform aggressive cancer biology and is associated with better survival in triple-negative breast cancer. npj Breast Cancer *8*, 92. https://doi.org/10.1038/s41523-022-00466-2.
25. Xu, J., Yang, J., Pan, X., and Wang, J. (2023). Prognostic and immunotherapeutic significance of immunogenic cell death-related genes in colon adenocarcinoma patients. Sci. Rep. *13*, 19188. https://doi.org/10.1038/s41598-023-46675-y.
26. Cords, L., Engler, S., Haberecker, M., Rüschoff, J.H., Moch, H., de Souza, N., and Bodenmiller, B. (2024). Cancer-associated fibroblast phenotypes are associated with patient outcome in non-small cell lung cancer. Cancer Cell *42*, 396–412.e5. https://doi.org/10.1016/j.ccell.2023.12.021.
27. Cords, L., Tietscher, S., Anzeneder, T., Langwieder, C., Rees, M., de Souza, N., and Bodenmiller, B. (2023). Cancer-associated fibroblast classification in single-cell and spatial proteomics data. Nat. Commun. *14*, 4294. https://doi.org/10.1038/s41467-023-39762-1.
28. Carriere, V., Roussel, L., Ortega, N., Lacorre, D.A., Americh, L., Aguilar, L., Bouche, G., and Girard, J.P. (2007). IL-33, the IL-1-like cytokine ligand for ST2 receptor, is a chromatin-associated nuclear factor in vivo. Proc. Natl. Acad. Sci. USA *104*, 282–287. https://doi.org/10.1073/pnas.0606854104.
29. Zhang, P., Gao, F., Wang, Q., Wang, X., Zhu, F., Ma, C., Sun, W., and Zhang, L. (2007). Agonistic anti-4-1BB antibody promotes the expansion of natural regulatory T cells while maintaining Foxp3 expression. Scand. J. Immunol. *66*, 435–440. https://doi.org/10.1111/j.1365-3083.2007.01994.x.
30. Yang, W.C., Hwang, Y.S., Chen, Y.Y., Liu, C.L., Shen, C.N., Hong, W.H., Lo, S.M., and Shen, C.R. (2017). Interleukin-4 Supports the Suppressive Immune Responses Elicited by Regulatory T Cells. Front. Immunol. *8*, 1508. https://doi.org/10.3389/fimmu.2017.01508.
31. Hatzioannou, A., Banos, A., Sakelaropoulos, T., Fedonidis, C., Vidali, M.S., Köhne, M., Händler, K., Boon, L., Henriques, A., Koliaraki, V., et al. (2020). An intrinsic role of IL-33 in T(reg) cell-mediated tumor immunoevasion. Nat. Immunol. *21*, 75–85. https://doi.org/10.1038/s41590-019-0555-2.
32. Risom, T., Glass, D.R., Averbukh, I., Liu, C.C., Baranski, A., Kagel, A., McCaffrey, E.F., Greenwald, N.F., Rivero-Gutiérrez, B., Strand, S.H., et al. (2022). Transition to invasive breast cancer is associated with progressive changes in the structure and composition of tumor stroma. Cell *185*, 299–310.e18. https://doi.org/10.1016/j.cell.2021.12.023.
33. Faustino, L.D., Griffith, J.W., Rahimi, R.A., Nepal, K., Hamilos, D.L., Cho, J.L., Medoff, B.D., Moon, J.J., Vignali, D.A.A., and Luster, A.D. (2020). Interleukin-33 activates regulatory T cells to suppress innate gammadelta T cell responses in the lung. Nat. Immunol. *21*, 1371–1383. https://doi.org/10.1038/s41590-020-0785-3.
34. Russi, A.E., Ebel, M.E., Yang, Y., and Brown, M.A. (2018). Male-specific IL-33 expression regulates sex-dimorphic EAE susceptibility. Proc. Natl. Acad. Sci. USA *115*, E1520–E1529. https://doi.org/10.1073/pnas.1710401115.
35. Levine, J.H., Simonds, E.F., Bendall, S.C., Davis, K.L., Amir, E.a.D., Tadmor, M.D., Litvin, O., Fienberg, H.G., Jager, A., Zunder, E.R., et al. (2015). Data-Driven Phenotypic Dissection of AML Reveals Progenitor-like Cells that Correlate with Prognosis. Cell *162*, 184–197. https://doi.org/10.1016/j.cell.2015.05.047.
36. Emerson, D.A., Rolig, A.S., and Redmond, W.L. (2021). Enhancing the Generation of Eomes(hi) CD8(+) T Cells Augments the Efficacy of OX40- and CTLA-4-Targeted Immunotherapy. Cancer Immunol. Res. *9*, 430–440. https://doi.org/10.1158/2326-6066.CIR-20-0338.
37. Llaó-Cid, L., Roessner, P.M., Chapaprieta, V., Öztürk, S., Roider, T., Bordas, M., Izcue, A., Colomer, D., Dietrich, S., Stilgenbauer, S., et al. (2021). EOMES is essential for antitumor activity of CD8(+) T cells in chronic lymphocytic leukemia. Leukemia *35*, 3152–3162. https://doi.org/10.1038/s41375-021-01198-1.
38. Lehtonen, A., Veckman, V., Nikula, T., Lahesmaa, R., Kinnunen, L., Matikainen, S., and Julkunen, I. (2005). Differential expression of IFN regulatory factor 4 gene in human monocyte-derived dendritic cells and macrophages. J. Immunol. *175*, 6570–6579. https://doi.org/10.4049/jimmunol.175.10.6570.
39. Satoh, T., Takeuchi, O., Vandenbon, A., Yasuda, K., Tanaka, Y., Kumagai, Y., Miyake, T., Matsushita, K., Okazaki, T., Saitoh, T., et al. (2010). The Jmjd3-Irf4 axis regulates M2 macrophage polarization and host responses against helminth infection. Nat. Immunol. *11*, 936–944. https://doi.org/10.1038/ni.1920.
40. Nopora, K., Bernhard, C.A., Ried, C., Castello, A.A., Murphy, K.M., Marconi, P., Koszinowski, U., and Brocker, T. (2012). MHC class I cross-presentation by dendritic cells counteracts viral immune evasion. Front. Immunol. *3*, 348. https://doi.org/10.3389/fimmu.2012.00348.
41. Dykema, A.G., Zhang, J., Cheung, L.S., Connor, S., Zhang, B., Zeng, Z., Cherry, C.M., Li, T., Caushi, J.X., Nishimoto, M., et al. (2023). Lung tumor-infiltrating T(reg) have divergent transcriptional profiles and function linked to checkpoint blockade response. Sci. Immunol. *8*, eadg1487. https://doi.org/10.1126/sciimmunol.adg1487.
42. Allinen, M., Beroukhim, R., Cai, L., Brennan, C., Lahti-Domenici, J., Huang, H., Porter, D., Hu, M., Chin, L., Richardson, A., et al. (2004). Molecular characterization of the tumor microenvironment in breast cancer. Cancer Cell *6*, 17–32. https://doi.org/10.1016/j.ccr.2004.06.010.
43. Hu, M., Yao, J., and Polyak, K. (2006). Methylation-Specific Digital Karyotyping. Nat. Protoc. *1*, 1621–1636.
44. Gil Del Alcazar, C.R., Alečković, M., and Polyak, K. (2020). Immune Escape during Breast Tumor Progression. Cancer Immunol. Res. *8*, 422–427. https://doi.org/10.1158/2326-6066.CIR-19-0786.
45. Plitas, G., Konopacki, C., Wu, K., Bos, P.D., Morrow, M., Putintseva, E.V., Chudakov, D.M., and Rudensky, A.Y. (2016). Regulatory T Cells Exhibit Distinct Features in Human Breast Cancer. Immunity *45*, 1122–1134. https://doi.org/10.1016/j.immuni.2016.10.032.
46. Delacher, M., Imbusch, C.D., Hotz-Wagenblatt, A., Mallm, J.P., Bauer, K., Simon, M., Riegel, D., Rendeiro, A.F., Bittner, S., Sanderink, L., et al. (2020). Precursors for Nonlymphoid-Tissue Treg Cells Reside in Secondary Lymphoid Organs and Are Programmed by the Transcription Factor BATF. Immunity *52*, 295–312.e11. https://doi.org/10.1016/j.immuni.2019.12.002.
47. Oliveira, G., Stromhaug, K., Cieri, N., Iorgulescu, J.B., Klaeger, S., Wolff, J.O., Rachimi, S., Chea, V., Krause, K., Freeman, S.S., et al. (2022). Landscape of helper and regulatory antitumour CD4(+) T cells in melanoma. Nature *605*, 532–538. https://doi.org/10.1038/s41586-022-04682-5.
48. Buchan, S.L., Rogel, A., and Al-Shamkhani, A. (2018). The immunobiology of CD27 and OX40 and their potential as targets for cancer immunotherapy. Blood *131*, 39–48. https://doi.org/10.1182/blood-2017-07-741025.

49. Evans, D.E., Prell, R.A., Thalhofer, C.J., Hurwitz, A.A., and Weinberg, A.D. (2001). Engagement of OX40 enhances antigen-specific CD4(+) T cell mobilization/memory development and humoral immunity: comparison of alphaOX-40 with alphaCTLA-4. J. Immunol. *167*, 6804–6811. https://doi.org/10.4049/jimmunol.167.12.6804.

50. Gough, M.J., Ruby, C.E., Redmond, W.L., Dhungel, B., Brown, A., and Weinberg, A.D. (2008). OX40 agonist therapy enhances CD8 infiltration and decreases immune suppression in the tumor. Cancer Res. *68*, 5206–5215. https://doi.org/10.1158/0008-5472.CAN-07-6484.

51. Pan, P.Y., Zang, Y., Weber, K., Meseck, M.L., and Chen, S.H. (2002). OX40 ligation enhances primary and memory cytotoxic T lymphocyte responses in an immunotherapy for hepatic colon metastases. Mol. Ther. *6*, 528–536. https://doi.org/10.1006/mthe.2002.0699.

52. Zhang, X., Xiao, X., Lan, P., Li, J., Dou, Y., Chen, W., Ishii, N., Chen, S., Xia, B., Chen, K., et al. (2018). OX40 Costimulation Inhibits Foxp3 Expression and Treg Induction via BATF3-Dependent and Independent Mechanisms. Cell Rep. *24*, 607–618. https://doi.org/10.1016/j.celrep.2018.06.052.

53. Burocchi, A., Pittoni, P., Gorzanelli, A., Colombo, M.P., and Piconese, S. (2011). Intratumor OX40 stimulation inhibits IRF1 expression and IL-10 production by Treg cells while enhancing CD40L expression by effector memory T cells. Eur. J. Immunol. *41*, 3615–3626. https://doi.org/10.1002/eji.201141700.

54. Ito, T., Wang, Y.H., Duramad, O., Hanabuchi, S., Perng, O.A., Gilliet, M., Qin, F.X.F., and Liu, Y.J. (2006). OX40 ligand shuts down IL-10-producing regulatory T cells. Proc. Natl. Acad. Sci. USA *103*, 13138–13143. https://doi.org/10.1073/pnas.0603107103.

55. Davis, E.J., Martin-Liberal, J., Kristeleit, R., Cho, D.C., Blagden, S.P., Berthold, D., Cardin, D.B., Vieito, M., Miller, R.E., Hari Dass, P., et al. (2022). First-in-human phase I/II, open-label study of the anti-OX40 agonist INCAGN01949 in patients with advanced solid tumors. J. Immunother. Cancer *10*, e004235. https://doi.org/10.1136/jitc-2021-004235.

56. Saltz, J., Gupta, R., Hou, L., Kurc, T., Singh, P., Nguyen, V., Samaras, D., Shroyer, K.R., Zhao, T., Batiste, R., et al. (2018). Spatial Organization and Molecular Correlation of Tumor-Infiltrating Lymphocytes Using Deep Learning on Pathology Images. Cell Rep. *23*, 181–193.e7. https://doi.org/10.1016/j.celrep.2018.03.086.

57. Curtis, C., Shah, S.P., Chin, S.-F., Turashvili, G., Rueda, O.M., Dunning, M.J., Speed, D., Lynch, A.G., Samarajiwa, S., Yuan, Y., et al. (2012). The genomic and transcriptomic architecture of 2,000 breast tumours reveals novel subgroups. Nature *486*, 346–352.

58. Ameri, A.H., Moradi Tuchayi, S., Zaalberg, A., Park, J.H., Ngo, K.H., Li, T., Lopez, E., Colonna, M., Lee, R.T., Mino-Kenudson, M., and Demehri, S. (2019). IL-33/regulatory T cell axis triggers the development of a tumor-promoting immune environment in chronic inflammation. Proc. Natl. Acad. Sci. USA *116*, 2646–2651. https://doi.org/10.1073/pnas.1815016116.

59. Pastille, E., Wasmer, M.H., Adamczyk, A., Vu, V.P., Mager, L.F., Phuong, N.N.T., Palmieri, V., Simillion, C., Hansen, W., Kasper, S., et al. (2019). The IL-33/ST2 pathway shapes the regulatory T cell phenotype to promote intestinal cancer. Mucosal Immunol. *12*, 990–1003. https://doi.org/10.1038/s41385-019-0176-y.

60. Sun, R., Zhao, H., Gao, D.S., Ni, A., Li, H., Chen, L., Lu, X., Chen, K., and Lu, B. (2023). Amphiregulin couples IL1RL1(+) regulatory T cells and cancer-associated fibroblasts to impede antitumor immunity. Sci. Adv. *9*, eadd7399. https://doi.org/10.1126/sciadv.add7399.

61. Kwon, J.W., Seok, S.H., Kim, S., An, H.W., Choudhury, A.D., Woo, S.H., Oh, J.S., Kim, J.K., Voon, D.C., Kim, D.Y., and Park, J.W. (2023). A synergistic partnership between IL-33/ST2 and Wnt pathway through Bcl-xL drives gastric cancer stemness and metastasis. Oncogene *42*, 501–515. https://doi.org/10.1038/s41388-022-02575-5.

62. Marangoni, F., Zhakyp, A., Corsini, M., Geels, S.N., Carrizosa, E., Thelen, M., Mani, V., Prüßmann, J.N., Warner, R.D., Ozga, A.J., et al. (2021). Expansion of tumor-associated Treg cells upon disruption of a CTLA-4-dependent feedback loop. Cell *184*, 3998–4015.e19. https://doi.org/10.1016/j.cell.2021.05.027.

63. Bennett, C.L., and Clausen, B.E. (2007). DC ablation in mice: promises, pitfalls, and challenges. Trends Immunol. *28*, 525–531. https://doi.org/10.1016/j.it.2007.08.011.

64. Liu, T.T., Kim, S., Desai, P., Kim, D.H., Huang, X., Ferris, S.T., Wu, R., Ou, F., Egawa, T., Van Dyken, S.J., et al. (2022). Ablation of cDC2 development by triple mutations within the Zeb2 enhancer. Nature *607*, 142–148. https://doi.org/10.1038/s41586-022-04866-z.

65. Bankhead, P., Loughrey, M.B., Fernández, J.A., Dombrowski, Y., McArt, D.G., Dunne, P.D., McQuaid, S., Gray, R.T., Murray, L.J., Coleman, H.G., et al. (2017). QuPath: Open source software for digital pathology image analysis. Sci. Rep. *7*, 16878. https://doi.org/10.1038/s41598-017-17204-5.

66. Hao, Y., Hao, S., Andersen-Nissen, E., Mauck, W.M., 3rd, Zheng, S., Butler, A., Lee, M.J., Wilk, A.J., Darby, C., Zager, M., et al. (2021). Integrated analysis of multimodal single-cell data. Cell *184*, 3573–3587.e29. https://doi.org/10.1016/j.cell.2021.04.048.

67. Villanueva, R.A.M., and Chen, Z.J. (2019). ggplot2: Elegant Graphics for Data Analysis. Meas. Interdiscip. Res. Perspect. *17*, 160–167. https://doi.org/10.1080/15366367.2019.1565254.

68. Aibar, S., González-Blas, C.B., Moerman, T., Huynh-Thu, V.A., Imrichova, H., Hulselmans, G., Rambow, F., Marine, J.C., Geurts, P., Aerts, J., et al. (2017). SCENIC: single-cell regulatory network inference and clustering. Nat. Methods *14*, 1083–1086. https://doi.org/10.1038/nmeth.4463.

69. Jin, S., Guerrero-Juarez, C.F., Zhang, L., Chang, I., Ramos, R., Kuan, C.H., Myung, P., Plikus, M.V., and Nie, Q. (2021). Inference and analysis of cell-cell communication using CellChat. Nat. Commun. *12*, 1088. https://doi.org/10.1038/s41467-021-21246-9.

70. Gu, Z., Eils, R., and Schlesner, M. (2016). Complex heatmaps reveal patterns and correlations in multidimensional genomic data. Bioinformatics *32*, 2847–2849. https://doi.org/10.1093/bioinformatics/btw313.

71. Gu, Z., Gu, L., Eils, R., Schlesner, M., and Brors, B. (2014). circlize Implements and enhances circular visualization in R. Bioinformatics *30*, 2811–2812. https://doi.org/10.1093/bioinformatics/btu393.

72. Hänzelmann, S., Castelo, R., and Guinney, J. (2013). GSVA: gene set variation analysis for microarray and RNA-seq data. BMC Bioinf. *14*, 7. https://doi.org/10.1186/1471-2105-14-7.

73. Robinson, M.D., McCarthy, D.J., and Smyth, G.K. (2010). edgeR: a Bioconductor package for differential expression analysis of digital gene expression data. Bioinformatics *26*, 139–140. https://doi.org/10.1093/bioinformatics/btp616.

74. Alečković, M., Cristea, S., Gil Del Alcazar, C.R., Yan, P., Ding, L., Krop, E.D., Harper, N.W., Rojas Jimenez, E., Lu, D., Gulvady, A.C., et al. (2022). Breast cancer prevention by short-term inhibition of TGFβ signaling. Nat. Commun. *13*, 7558. https://doi.org/10.1038/s41467-022-35043-5.

75. Egelston, C.A., Guo, W., Tan, J., Avalos, C., Simons, D.L., Lim, M.H., Huang, Y.J., Nelson, M.S., Chowdhury, A., Schmolze, D.B., et al. (2022). Tumor-infiltrating exhausted CD8+ T cells dictate reduced survival in premenopausal estrogen receptor-positive breast cancer. JCI Insight *7*, e153963. https://doi.org/10.1172/jci.insight.153963.

76. Losurdo, A., Scirgolea, C., Alvisi, G., Brummelman, J., Errico, V., Di Tommaso, L., Pilipow, K., Colombo, F.S., Fernandes, B., Peano, C., et al. (2021). Single-cell profiling defines the prognostic benefit of CD39(high) tissue resident memory CD8+ T cells in luminal-like breast cancer. Commun. Biol. *4*, 1117. https://doi.org/10.1038/s42003-021-02595-z.

77. Miragaia, R.J., Gomes, T., Chomka, A., Jardine, L., Riedel, A., Hegazy, A.N., Whibley, N., Tucci, A., Chen, X., Lindeman, I., et al. (2019). Single-Cell Transcriptomics of Regulatory T Cells Reveals Trajectories of Tissue Adaptation. Immunity *50*, 493–504.e7. https://doi.org/10.1016/j.immuni.2019.01.001.

78. Zheng, L., Qin, S., Si, W., Wang, A., Xing, B., Gao, R., Ren, X., Wang, L., Wu, X., Zhang, J., et al. (2021). Pan-cancer single-cell landscape of tumor-infiltrating T cells. Science *374*, abe6474. https://doi.org/10.1126/science.abe6474.

79. Jiao, S., Xiong, Q., Yan, M., Zhan, X., Yang, Z., Peng, C., Sun, B., Pang, D., and Liu, T. (2022). Intratumor expanded T cell clones can be non-sentinel lymph node derived in breast cancer revealed by single-cell immune profiling. J. Immunother. Cancer *10*, e003325. https://doi.org/10.1136/jitc-2021-003325.

80. Lee, Y.J., Kim, J.Y., Jeon, S.H., Nam, H., Jung, J.H., Jeon, M., Kim, E.S., Bae, S.J., Ahn, J., Yoo, T.K., et al. (2022). CD39(+) tissue-resident memory CD8(+) T cells with a clonal overlap across compartments mediate antitumor immunity in breast cancer. Sci. Immunol. *7*, eabn8390. https://doi.org/10.1126/sciimmunol.abn8390.

81. Nalio Ramos, R., Missolo-Koussou, Y., Gerber-Ferder, Y., Bromley, C.P., Bugatti, M., Núñez, N.G., Tosello Boari, J., Richer, W., Menger, L., Denizeau, J., et al. (2022). Tissue-resident FOLR2(+) macrophages associate with CD8(+) T cell infiltration in human breast cancer. Cell *185*, 1189–1207.e25. https://doi.org/10.1016/j.cell.2022.02.021.

82. Ahluwalia, P., Ahluwalia, M., Mondal, A.K., Sahajpal, N., Kota, V., Rojiani, M.V., Rojiani, A.M., and Kolhe, R. (2021). Immunogenomic Gene Signature of Cell-Death Associated Genes with Prognostic Implications in Lung Cancer. Cancers (Basel) *13*, 155. https://doi.org/10.3390/cancers13010155.

83. Azizi, E., Carr, A.J., Plitas, G., Cornish, A.E., Konopacki, C., Prabhakaran, S., Nainys, J., Wu, K., Kiseliovas, V., Setty, M., et al. (2018). Single-Cell Map of Diverse Immune Phenotypes in the Breast Tumor Microenvironment. Cell *174*, 1293–1308.e36. https://doi.org/10.1016/j.cell.2018.05.060.

84. Codarri Deak, L., Nicolini, V., Hashimoto, M., Karagianni, M., Schwalie, P.C., Lauener, L., Varypataki, E.M., Richard, M., Bommer, E., Sam, J., et al. (2022). PD-1-cis IL-2R agonism yields better effectors from stem-like CD8(+) T cells. Nature *610*, 161–172. https://doi.org/10.1038/s41586-022-05192-0.

85. Wang, M., Windgassen, D., and Papoutsakis, E.T. (2008). A global transcriptional view of apoptosis in human T-cell activation. BMC Med. Genom. *1*, 53. https://doi.org/10.1186/1755-8794-1-53.

86. Borcherding, N., Vishwakarma, A., Voigt, A.P., Bellizzi, A., Kaplan, J., Nepple, K., Salem, A.K., Jenkins, R.W., Zakharia, Y., and Zhang, W. (2021). Mapping the immune environment in clear cell renal carcinoma by single-cell genomics. Commun. Biol. *4*, 122. https://doi.org/10.1038/s42003-020-01625-6.

87. Anghel, C.V., Quon, G., Haider, S., Nguyen, F., Deshwar, A.G., Morris, Q.D., and Boutros, P.C. (2015). ISOpureR: an R implementation of a computational purification algorithm of mixed tumour profiles. BMC Bioinf. *16*, 156. https://doi.org/10.1186/s12859-015-0597-x.

88. Yoshihara, K., Shahmoradgoli, M., Martínez, E., Vegesna, R., Kim, H., Torres-Garcia, W., Treviño, V., Shen, H., Laird, P.W., Levine, D.A., et al. (2013). Inferring tumour purity and stromal and immune cell admixture from expression data. Nat. Commun. *4*, 2612. https://doi.org/10.1038/ncomms3612.

89. Keren, L., Bosse, M., Marquez, D., Angoshtari, R., Jain, S., Varma, S., Yang, S.R., Kurian, A., Van Valen, D., West, R., et al. (2018). A Structured Tumor-Immune Microenvironment in Triple Negative Breast Cancer Revealed by Multiplexed Ion Beam Imaging. Cell *174*, 1373–1387.e19. https://doi.org/10.1016/j.cell.2018.08.039.

90. Keren, L., Bosse, M., Thompson, S., Risom, T., Vijayaragavan, K., McCaffrey, E., Marquez, D., Angoshtari, R., Greenwald, N.F., Fienberg, H., et al. (2019). MIBI-TOF: A multiplexed imaging platform relates cellular phenotypes and tissue structure. Sci. Adv. *5*, eaax5851. https://doi.org/10.1126/sciadv.aax5851.

Please cite this article in press as: Bui et al., Identification of cycling regulatory T cell precursors as conductors of immune escape during breast carcinoma progression, Cancer Cell (2026), https://doi.org/10.1016/j.ccell.2026.03.015

CellPress
OPEN ACCESS

STAR★METHODS

KEY RESOURCES TABLE

REAGENT or RESOURCE	SOURCE	IDENTIFIER
Antibodies		
Anti-BrdU, FITC (3D4)	BioLegend	RRID:AB_2564480
Anti-Ki67 (SP6)	Abcam	RRID:AB_302459
Anti-Ki67, Alexa Fluor 647 (SP6)	Abcam	RRID:AB_3105924
Anti-Ki67 (SolA15)	Invitrogen	RRID:AB_10854564
Anti-CD34 (EP373Y]	Abcam	RRID:AB_1640331
Anti-GSN (893205)	R&D Systems	RRID:AB_2885051
Anti-CD163 (EPR19518)	Abcam	RRID:AB_2753196
Anti-ER (Erb455)	Abcam	RRID:AB_2757815
Anti-LAG3	Proteintech	RRID:AB_2133350
Anti-CD137 (2G1)	Invitrogen	RRID:AB_2911721
Anti-IL-33 (EPR20417)	Abcam	RRID:AB_2827630
Anti-mouse/rat IL-33 (Bondy-1-1)	AdipoGen Life Sciences	RRID:AB_2490504
Anti-rat PD-1	Gordon Freeman, DFCI	in-house (DFCI)
Anti-CD279 (PD-1) (EH12.1)	BD Bioscience	RRID:AB_2738425
Anti-alpha-SMA	Epredia	RRID:AB_64000
Anti-Alpha-SMA	Lab Vision	RRID:AB_63997
InVivoMAb anti-rat PD-L1 (368A.4H1)	BioXcell	RRID:AB_2927520
InVivoMAb anti-rat OX-40 (OX-86)	BioXcell	RRID:AB_1107592
InVivoMAb rat IgG1 isotype control (HRPN-CP167)	BioXcell	RRID:AB_1107775
InVivoMAb mouse IgG1 isotype control (MOPC-21)	BioXcell	RRID:AB_1107784
InVivoMAb mouse IgG2b isotype control (MPC-11)	BioXcell	RRID:AB_1107791
InVivoMAb anti-rat CD4 (OX-38)	BioXcell	RRID:AB_2736988
InVivoMAb anti-rat CTLA4 (9H10)	BioXcell	RRID:AB_10950184
InVivoMAb anti-rat TCR α/β (R73)	BioXcell	RRID:AB_3696137
InVivoMAb anti-mouse/rat MHC Class II (I-Ek/RT1-D) (14-4-4S/HB-32)	BioXcell	RRID:AB_10950190
InVivoMAb anti-rat CD80 (B7-1) (3H5)	BioXcell	RRID:AB_10949011
Anti-Human IL-33 (Tozorakimab)	Med Chem Express	RRID:AB_3695300
Anti-Human ST-2 (Astegolimab)	Med Chem Express	RRID:AB_3695235
Anti-OX-40, Alexa Fluor 647 (OX-40)	BioLegend	RRID:AB_2207357
Anti-CTLA4, PE (WKH203)	Invitrogen	RRID:AB_465877
Anti-CD3, FITC (1F4)	BioLegend	RRID:AB_2073344
Anti-CD3 (CD3-12)	Abcam	RRID:AB_2889189
Anti-CD3 (OKT3)	BioLegend	RRID:AB_11126166
Anti-TCRα/β, APC (R73)	BioLegend	RRID:AB_313919
Anti-TCRα/β, FITC (R73)	BioLegend	RRID:AB_313914
Anti-CD4, APC/Cyanine7 (W3/25)	BioLegend	RRID:AB_1186084
Anti-CD4, BV750 (SK3)	BioLegend	RRID:AB_2734346
Anti-ICOS, BV605 (C398.4)	BioLegend	RRID:AB_2687079
Anti-CD86, BV786 (24F)	BD Biosciences	RRID:AB_2741352
Anti-CD80, BV421 (3H5)	BD Biosciences	RRID:AB_2741816

(*Continued on next page*)

Please cite this article in press as: Bui et al., Identification of cycling regulatory T cell precursors as conductors of immune escape during breast carcinoma progression, Cancer Cell (2026), https://doi.org/10.1016/j.ccell.2026.03.015

Continued

REAGENT or RESOURCE	SOURCE	IDENTIFIER
Anti-CD11b/c, BV421 (OX-42)	BD Biosciences	RRID:AB_2741898
Anti-CD11b/c, BV750 (OX-40)	BD Biosciences	RRID:AB_2872104
Anti-CD11c, BV510 (3.9)	BioLegend	RRID:AB_2561990
Anti-CD68, PE (QA20A71)	BioLegend	RRID:AB_2936606
Anti-CD19, FITC (anti-mouse, also work for rat, MB19-1)	BioLegend	RRID:AB_312825
Anti-FOXP3 (236A/E7)	Abcam	RRID:AB_445284
Anti-FOXP3 (FJK-16s)	eBioscience/Invitrogen	RRID:AB_467576
Anti-FOXP3, eFluor450 (FJK-16s)	eBioscience/Invitrogen	RRID:AB_1518812
Anti-FOXP3, PerCP-Cyanine5.5 (FJK-16s)	eBioscience/Invitrogen	RRID:AB_914351
Anti-FOXP3, PE (FJK-16s)	eBioscience/Invitrogen	RRID:AB_465936
Anti-FOXP3, BV421 (206D)	BioLegend	RRID:AB_2561338
Anti-CD8A, BV711 (OX-8)	BD Biosciences	RRID:AB_2740402
Anti-CD8A, PerCP (OX-8)	BioLegend	RRID:AB_2075263
Anti-CD8A, BV711 (SK1)	BioLegend	RRID:AB_2565242
Anti-CD45RC, BV786 (OX-22)	BD Biosciences	RRID:AB_2740824
Anti-CD25, BV650 (OX-39)	BD Biosciences	RRID:AB_2741020
Anti-CD25, BV650 (BC96)	BioLegend	RRID:AB_11203536
Anti-Helios (anti-mouse, also work for rat), Alexa Fluor 647 (22F6)	BD Biosciences	RRID:AB_2738506
Anti-Helios (anti-mouse, also work for rat), Alexa Fluor 488 (22F6)	BD Biosciences	RRID:AB_2738505
Anti-Eomes, PE (anti-mouse, also work for rat) (W17001A)	BioLegend	RRID:AB_2888891
Anti-CD44, BV750 (OX-49)	BD Biosciences	RRID:AB_2872060
Anti-IRF4, Alexa Fluor 700 (anti-mouse, also work for rat) (3E4)	eBioscience/Invitrogen	RRID:AB_2848476
Anti-IRF8, eFluor450 (anti-mouse, also work for rat) (V3GYWCH)	eBioscience/Invitrogen	RRID:AB_2784733
Anti-RT1A, BV510 (C3)	BD Biosciences	RRID:AB_2743027
Anti-RT1A, purified (OX-18)	BioLegend	RRID:AB_1227711
Anti-CD10, RFE (SS2/36)	Agilent Dako	RRID:AB_579550
Anti-CD45, APC-eFLuor 780 (HI30)	eBioscience	RRID:AB_1944368
Anti-CD45, FITC (OX-1)	Invitrogen	RRID:AB_2572455
Anti-CD45, PE/Cyanine7 (HI30)	BioLegend	RRID:AB_314403
Anti-CD45, PE/Cyanine7 (OX-1)	BioLegend	RRID:AB_2253306
Zenon™ Rabbit IgG Labeling Kits/Alexa Fluor 594	Invitrogen	RRID:AB_2736956
Fc block: Anti-rat CD32	BD Pharmingen	RRID:AB_393568
Human TruStain FcX™ (Fc Receptor Blocking Solution)	BioLegend	RRID:AB_2818986
Anti-OX-40, Alexa Fluor 647 (OX-40)	BioLegend	RRID:AB_2207357
Anti-CTLA4, unconjugated	LSBio	RRID:AB_1648658
Anti-CD127 (IL-7α), FITC (A019D5)	BioLegend	RRID:AB_10897643
Anti-CD103, BV605 (OX-62)	BD Biosciences	RRID:AB_2742741
Anti-CD103, PE (OX-62)	Invitrogen	RRID:AB_1210757
Anti-CD103, PE/Dazzle 594 (Ber-ACT8)	BioLegend	RRID:AB_2716188
Anti-SIRPα, APC (OX-41)	eBioscience/Invitrogen	RRID:AB_2573174
Anti-SIRPα, BV786 (OX-41)	BD Biosciences	RRID:AB_2742442
Anti-SIRPα, APC (OX-41)	Invitrogen	RRID:AB_2573173

(*Continued on next page*)

Please cite this article in press as: Bui et al., Identification of cycling regulatory T cell precursors as conductors of immune escape during breast carcinoma progression, Cancer Cell (2026), https://doi.org/10.1016/j.ccell.2026.03.015

Continued

REAGENT or RESOURCE	SOURCE	IDENTIFIER
Anti-CD172α/β (SIRPα/β), PE (SE5A5)	BioLegend	RRID:AB_830704
Anti-RT1B, BV650 (OX-6)	BD Biosciences	RRID:AB_2742019
Anti-XCR1, APC/Cyanine7 (ZET)	BioLegend	RRID:AB_2783117
Anti-XCR1, APC (ZET)	BioLegend	RRID:AB_2563932
Anti-XCR1, APC/Cyanine7 (S15046E)	BioLegend	RRID:AB_2894579
Anti-rat IL-10, purified	BD Biosciences	RRID:AB_10896146
Anti-IL-10, APC (JES3-19F1)	BioLegend	RRID:AB_315457
Anti-IL-10, unconjugated (2G101H7)	eBioscience/Invitrogen	RRID:AB_1500314
Anti-TNFα, BV785 (MAb11)	BioLegend	RRID:AB_2565858
Anti-IFNγ, PerCP/Cyanine5.5 (4S.B3)	BioLegend	RRID:AB_961355
Epithelial antigen, FITC (Ber-EP4)	Agilent Dako	RRID:AB_578689
Anti-CD326 (EpCAM), Alexa Fluor 647 (10D6)	BioLegend	RRID:AB_2904313
Anti-EpCAM (polyclonal)	Abcam	RRID:AB_1603782
Anti-CD45RA, APC/Cyanine7 (HI100)	BioLegend	RRID:AB_10708880
Anti-CD45RA, PerCP/Cyanine5.5 (OX-33)	BioLegend	RRID:AB_2565945
Anti-CD45RO, Alexa Fluor 700 (UCHL1)	BioLegend	RRID:AB_493765
Anti-CD103 (ITGAE/2063)	Abcam	RRID:AB_2819069
Anti-CLEC10A (ERP27400-166)	Abcam	ab315086 (RRID not available)
Anti-Granzyme B	Abcam	RRID:AB_304251
Anti-CD8 alpha (C8/144B)	Invitrogen	RRID:AB_11000353
Anti-rat CD3 (purified Ab, functional grade)	BioLegend	RRID:AB_893302
Anti-rat CD28 (purified Ab, functional grade) (1F4)	BioLegend	RRID:AB_31389
Anti-human CD3 (pure-functional grade) (OKT3)	Miltenyi Biotec	RRID:AB_1036144
Anti-human CD28 (pure-functional grade) (15E8)	Miltenyi Biotec	RRID:AB_1036134
Anti-human EpCAM/TROP-1	R&D Systems	RRID:AB_355745
Anti-Rat IgG1 Alexa Fluor 750-conjugate Ab (clone 43414)	R&D Systems	RRID:AB_3654380
Anti-Rat IgG2a Alexa Fluor 750-conjugate Ab (clone 54447)	R&D Systems	RRID:AB_3654384
Anti-Rat IgG2a Alexa Fluor 488 (MRG2a-83)	BioLegend	RRID:AB_2910464
Anti-Rat IgG2a Alexa Fluor 647 (MRG2a-83)	BioLegend	RRID:AB_2716140
Anti-Rat IgG1 Alexa Fluor 594 (MRG1-58)	BioLegend	RRID:AB_2721399
Anti-Rabbit IgG (H + L) Cross-Adsorbed Alexa Fluor 750	Invitrogen	RRID:AB_2535710
Anti-Mouse IgG2c, Fcγ fragment-specific Alexa Fluor 647	Jackson ImmunoResearch	RRID:AB_2632547
Anti-Goat IgG (H + L) Cross-Adsorbed Biotin-conjugate	Invitrogen	RRID:AB_2534683
Anti-Mouse IgG1 Superclonal™ Alexa Fluor Plus 555	Invitrogen	RRID:AB_3709162
Biological samples		
SD Rat CD3 Pan T cells Pooled, 5M cells	iQ Biosciences	Cat#: IQB-R1-T2-5
SD Rat PBMCS, 5M cells	iQ Biosciences	Cat#: IQB-RPB101-104
SD Rat Bone Marrow Cells Pooled, 10M cells	iQ Biosciences	Cat#: IQB-RBM101-104
SD Rat Splenocytes Pooled, 25M cells	iQ Biosciences	Cat#: IQB-RSP101-104

(*Continued on next page*)

Please cite this article in press as: Bui et al., Identification of cycling regulatory T cell precursors as conductors of immune escape during breast carcinoma progression, Cancer Cell (2026), https://doi.org/10.1016/j.ccell.2026.03.015

Continued

REAGENT or RESOURCE	SOURCE	IDENTIFIER
Primary Peripheral Blood Mononuclear Cells (healthy donors from 6 different lots)	ATCC	Cat#: PCS-800-011
Chemicals, peptides, and recombinant proteins		
Phosphate Buffered Saline (PBS), pH7.4	VWR	Cat# 392-0442P
Collagenase type IV	Worthington Biochemical Corporation	Cat# LS004189 CAS# 9001-12-1
Hyaluronidase	Sigma-Aldrich	Cat# H3506 CAS# 37326-33-3
Percoll	Sigma-Aldrich	Cat# P4937
Streptavidin, Alexa Fluor 514 conjugate	Invitrogen	RRID:AB_2315383
Brefeldin A Solution (1,000X)	BioLegend	Cat# 420601
5-Bromo-2′-deoxyuridine	Sigma Aldrich	Cat# B9285-1G
EdU (5-ethynyl-2′-deoxyuridine)	Invitrogen	Cat# E10415
CellTrace™ CSFE	Invitrogen	Cat# C34554 A
AZDye 647 Azide	Click Chemistry Tools	Cat# 1299-1
AZDye 555 Azide	Click Chemistry Tools	Cat# 1287-1
Prostaglandin E2	Sigma-Aldrich	RRID:SCR_008984, CAS: 363-24-6
Poly (I:C)	Miltenyi Biotec	Cat# 130-112-562
Rapamycin	Stem Cell Technologies	Cat# 73362
All-Trans Retinoic Acid	Stem Cell Technologies	Cat# 72262
(+)-Sodium L-ascorbate	Sigma Aldrich	Cat# A7631-25G
Copper(II) sulfate penta-hydrate	Sigma Aldrich	Cat# 209198-100G
Human GM-CSF, research grade	Miltenyi Biotec	Cat# 130-095-372
Human IL-4, research grade	Miltenyi Biotec	Cat# 130-093-917
Human IL-6	PeproTech	Cat# 200-06-20UG
Human IL-1β	PeproTech	Cat# 200-01B-10UG
Human TNF-α, premium grade	Miltenyi Biotec	Cat# 130-094-014
Human IL-33	PeproTech	Cat# 200-33-50UG
Human TGF-β	PeproTech	Cat# 100-21-10UG
Human IL-15	PeproTech	Cat# 200-15-10UG
rh IL-2	Stem Cell Technologies	Cat# 78036.3
Rat GM-CSF	PeproTech	Cat# 400-23-20UG
Rat IL-4	PeproTech	Cat# 400-04-20UG
Rat IL-6	PeproTech	Cat# 400-06-10UG
Rat IL-1β	PeproTech	Cat# 400-01B-10UG
Rat TNF-α	PeproTech	Cat# 400-14-20UG
Rat IL-2	PeproTech	Cat# 400-02-50UG
Rat TGF-β	Med Chem Express	Cat# HY-P7117
Rat IL-33	BioLegend	Cat# 766404
Critical commercial assays		
EasySep™ APC Positive Selection Kit II	Stem Cell Technologies	Cat# 17681
EasySep™ PE Positive Selection Kit II	Stem Cell Technologies	Cat# 17684
CD1c (BDCA-1)+ Dendritic Cell Isolation Kit, human	Miltenyi Biotec	Cat# 130-119-475
$CD4^+CD25^+CD127dim/-$ Regulatory T cell Isolation Kit II, human	Miltenyi Biotec	Cat# 130-094-775
Naive $CD4^+$ T cell Isolation Kit II, human	Miltenyi Biotec	Cat# 130-094-131
MS Columns	Miltenyi Biotec	Cat# 130-042-201
LD Columns	Miltenyi Biotec	Cat# 130-042-901
Chromium Next GEM Single Cell 5′ HT Kit v2	10x Genomics	PN: 1000356
MidiMACS™ Separator	Miltenyi Biotec	Cat# 130-042-302

(*Continued on next page*)

Continued

REAGENT or RESOURCE	SOURCE	IDENTIFIER
µMACS™ Separator	Miltenyi Biotec	Cat# 130-042-602
OctoMACS™ Separator	Miltenyi Biotec	Cat# 130-042-109
MagniSort™ Magnet	eBioscience	Cat# MAG-4902
EasySep™ Magnet	Stem Cell Technologies	Cat# 18000
MACS BSA Stock Solution	Miltenyi Biotec	Cat# 130-091-376
autoMACS Rinsing Solution	Miltenyi Biotec	Cat# 130-091-222
2-mercaptoethanol	Gibco	Cat# 21985-023
Dynabeads™ Human T-Activator CD3/CD28	Gibco	Cat# 11131D
L-Glutamine 200mM (100X)	Gibco	Cat# 25030-081
Pen Strep	Gibco	Cat# 15140-122
ImmunoCult™ ACF Dendritic Cell Medium	Stem Cell Technologies	Cat# 10986
RPMI-1640 Medium	Cytiva	Cat# SH30027.01
Iscove's Modified Dulbecco's Medium (IMDM)	Gibco	Cat# 12440-053
Lymphocyte Serum-Free Medium KBM581	Corning/Manufactured by Kohjin Bio	Cat# 88-581-CM
LIVE/DEAD™ Fixable Aqua Dead Cell Stain Kit	Thermo Fisher Scientific	Cat# L34957
True-Nuclear™ Transcription Factor Buffer Set	BioLegend	Cat# 424401
IHC Antigen Retrieval Solution, 10X High pH	Invitrogen	Cat# 00-4956-58
IHC Antigen Retrieval Solution, 10X Low pH	Invitrogen	Cat# 00-4955-58
TheraPEAK™ ACK Lysing Buffer (1X)	Lonza	Cat# BP10-548E
Deposited data		
scRNA-seq processed data	NCBI GEO	GSE253587
scRNA-seq raw data	Sequence Read Archive	BioProject PRJNA1062792
TCGA bulk RNA-seq	dbGaP	phs000178.v11.p8
METABRIC microarray	Synapse	Syn1688369
Experimental models: Organisms/strains		
Hsd:Sprague Dawley® SD® outbred rats	Envigo	https://www.inotiv.com/research-model/hsd-sprague-dawley-sd
Recombinant DNA		
pCMV6-Entry Mammalian Expression Vector	Origene	CAT#: PS100001
Cd4 (NM_012705) Rat Tagged ORF Clone	Origene	CAT#: RR210599
Cd8a (NM_031538) Rat Tagged ORF Clone	Origene	CAT#: RR208830
Cd8b (NM_031539) Rat Tagged ORF Clone	Origene	CAT#: RR214135
Clone OTI4C5, Anti-DDK (FLAG) monoclonal antibody (100ul)	Origene	CAT#: TA50011-100
Il2ra (NM_013163) Rat Tagged ORF Clone	Origene	CAT#: RR200895
Pdcd1 (NM_001106927) Rat Tagged ORF Clone	Origene	CAT#: RR212477
Software and algorithms		
QuPath (version: 0.4.0)	Bankhead et al.[65]	https://qupath.readthedocs.io/en/0.4/index.html
GraphPadPrism (version: 10.0.3)	GraphPad Software Inc.	https://www.graphpad.com/updates/prism-900-release-notes
FlowJo (version: 10.8.2)	FlowJo, LLC	https://www.flowjo.com/
Cell Ranger (version: 7.0.1)	10x Genomics	https://support.10xgenomics.com/single-cell-gene-expression/software/pipelines/latest/what-is-cell-ranger

(*Continued on next page*)

Continued

REAGENT or RESOURCE	SOURCE	IDENTIFIER
Seurat (version: 5.0.2)	Hao et al.[66]	https://satijalab.org/seurat/
ggplot2 (version: 3.5.0)	Randle Aaron et al.[67]	https://ggplot2.tidyverse.org
SCENIC (version: 1.3.1)	Aibar et al.[68]	https://scenic.aertslab.org
CellChat (version 1.6.1)	Jin et al.[69]	https://github.com/sqjin/CellChat
ComplexHeatmap (v2.20.0)	Gu et al.[70]	https://bioconductor.org/packages/release/bioc/html/ComplexHeatmap.html
circlize (v0.4.16)	Gu et al.[71]	https://cran.r-project.org/web/packages/circlize/index.html
igraph (v2.0.3)		https://igraph.org/
GSVA (version 1.50.1)	Hänzelmann et al.[72]	https://www.bioconductor.org/packages/release/bioc/html/GSVA.html
miloR (version 1.10.0)	Dann et al.[12]	https://github.com/MarioniLab/miloR
scCustomize (version 2.1.2)	NA	https://samuel-marsh.github.io/scCustomize/
edgeR (version 4.0.16)	Robinson et al.[73]	https://bioconductor.org/packages/release/bioc/html/edgeR.html

EXPERIMENTAL MODEL AND STUDY PARTICIPANT DETAILS

Patient specimens from multiple clinical cohorts

All patient samples were collected following informed consent using protocols approved by Institutional Review Boards at Dana-Farber Cancer Institute (protocols 10–458, 93–085, and 14–400), University of Pittsburgh, PA (HCC 04–162, PRO13070490, and STUDY22060066), Sutter Roseville Medical Center (protocol # 812322-13), and Seoul National University Bundang Hospital (protocol # B-1803/450-305, informed consent was waived). Clinical information of patients included in this study are listed in Table S1. All samples were de-identified in the tissue bank prior to shipment to the laboratory. Fresh DCIS samples were resected, stored in ice-cold DMEM/F12 media supplemented with BSA and penn-strep, and shipped overnight from the University of Pittsburgh and Sutter Roseville Medical Center to the Dana-Farber Cancer Institute for immediate tissue processing upon arrival. Fresh IBC and reduction mammoplasty samples were obtained from the Brigham and Women's Hospital, Boston, MA. Fresh patient samples were dissociated as previously described,[2,4] followed by Fluorescence-Activated Cell Sorting (FACS), and construction of single-cell RNA-seq library. HTAN-Duke scRNA-seq dataset was kindly provided by Dr. Shelley Hwang and previously described.[9] Public datasets of the EMBO[8] and the Japan National Cancer Center Research Institute (NCCRI) cohort[10] were downloaded from GSE161529 and GSE195861, respectively. Selected patients from EMBO cohorts, including 6 HER2+ IBC, 6 ER+ 3+ (100%) IBC, and 4 TNBC (no BRCA2 mutation) were selected dataset integration. The scRNA-seq datasets from the HTAN Duke cohort was deposited to the Human Tumor Atlas Network dbGaP Study with the following accession phs002371.v1.p1 (https://www.ncbi.nlm.nih.gov/projects/gap/cgi-bin/study.cgi?study_id=phs002371.v1.p1). All patients from HTAN-Duke and Japan NCCRI cohorts were analyzed and integrated into the 4-center DCIS/IBC atlas, constituting 72 patients (11 normal, 30 DCIS, 31 IBC) with all three HR+, HR-/HER2+, and TNBC breast cancer subtypes. Tissue microarrays of patients diagnosed with pure DCIS with follow-up for future recurrence and survival were generated by Dr. Robert West (TMA-501, TMA-502, TMA-503, TMA-504: double-core, $n = 177$ patients analyzed out of total 196 patients, excluding missing tissues, lobular diagnosis, tonsil, or biopsies lacking paired sections for dual Treg and $CD8^+$ staining) (Table S1). Formalin fixed paraffin embedded (FFPE) slides of patients diagnosed with pure DCIS and IBC with DCIS components ($n = 56$ patients analyzed) were obtained from the Seoul National University Bundang Hospital (Seoul, Korea) by Dr. So Yeon Park. This same cohort was also used in our prior study.[2] Bulk RNA-seq dataset of DCIS patients with clinical information on recurrence from the Washington University Resource of Archival Tissues (RAHBT cohort, $n = 196$ patients, stroma regions) was accessible under the permission of the HTAN Consortium by courtesy of Drs. Shelly Hwang and Robert West.[18] The 37-plex imaging dataset of DCIS patients ($n = 58$ DCIS patients out of total 70 patients) analyzed by multiplexed ion beam imaging (MIBI) was made accessible by courtesy of Drs. Robert West and Michael Angelo.[32] Clinical information and technical quantitation of this patient cohort have been extensively described.[32] The public datasets METABRIC Mass Cytometry Imaging,[19] $n = 693$ breast cancer patients) and TCGA,[56] $n = 992$ breast cancer patients out of total 4759 patients) including patients diagnosed with more invasive phenotypes were analyzed in this study.

Animals

All animal studies were performed within an AAALAC-certified barrier-contained facility at the Dana Farber Cancer Institute in strict adherence to protocol 15-005 approved by the Dana Farber Cancer Institute Animal Care and Use Committee. For all experiments, 22-day-old female virgin rats (Hsd: Sprague-Dawley, SD) were purchased from Envigo (Inotiv) and housed in pathogen-free, ventilated, solid-bottom, polysulfone 135 sq. microisolator cages supported by the Optimice racks with automated water supply.

Temperature and humidity within the facility is controlled at 72°F and 35–55% humidity under a standard automatic light cycle (12 h light/12 h dark). For all treatment studies, age-matched SD rats were randomized to each experimental group. Maximum tumor size burden is 4cm and set as humane endpoint for any rat study. At the end of all experimental procedures, animals were euthanized via CO_2 asphyxiation followed by intracardiac blood draw and rapid cervical dislocation.

METHOD DETAILS

In vivo experiments in outbred NMU-induced Sprague-Dawley rats

To induce mammary tumors, female SD rats were housed in DFCI rodent facility until they reached 40days of age when they were injected i.p. with 50 mg/kg of N-nitroso N-methylurea (NMU, dissolved in pH6 ddH_2O) or pH6 ddH_2O alone followed by another NMU injection 7 days after. Rats were monitored daily for detection of mammary tumors. For the time-course study of macroscopic tumors and microlesions, rats were challenged with the indicated NMU dose at 40 days of age. Animals were randomized and those presenting with palpable tumors (or not) along with adjacent mammary glands were collected at 2-week intervals between 2 and 14 weeks post-NMU exposure. All harvested MGs were processed for histological detection of DCIS-like microlesions. For OX40/PD-L1 dual-targeting study, rats were randomized into four treatment regimens prior to drug administration. Each rat was injected intraperitoneally (i.p.) with either αOX40 mAb (2.5 mg/kg/injection, every 48h, clone OX86, rat IgG, BioXcell), αPD-L1 mAb (10.0 mg/kg/injection, every 7 days, clone 368.A.4H1, mouse IgG1κ, BioXcell), a combinatory regimen of both αOX40 and αPD-L1, or isotype controls for αOX40 and/or αPD-L1 (2.5 or 10.0 mg/kg/injection, BioXcell). For IL-33 neutralization study, rats were randomized into two treatment regimens prior to drug administration. Drug administration was initiated following the detection of the first tumor(s) in each rat. Each rat was injected intraperitoneally (i.p.) with either αIL33 mAb (500 μg/kg/injection, every 72h, clone Bondy1-1, mouse IgG2b, AdipoGen Life Sciences) or IgG2b isotype control (500 μg/kg/injection, BioXcell). For both experiments, the sample size was chosen based on our previous experience with the SD rat model to yield 80% statistical power.[74] Antibody administration was initiated following the detection of the first tumor(s) in each rat. These antibodies were validated to have high-affinity for rat OX40, PD-L1, and IL-33, using rat cDNA ORF-FLAG mammalian 293FT system transfected by Lipofectamin 3000 Transfection Reagent. Flow cytometric assessment of transfected cells shown in Table S3 demonstrated both FLAG and rat protein signals detected by BioXcell antibodies (used for *in vivo*) and certified anti-rat FACS antibodies. For EdU/BrdU dual pulse-chase each rat was injected i.p. with two dosages of EdU (50 mg/kg/injection, 6-h interval) and one dosage of BrdU (50 mg/kg/injection) in a chase period of 96h and 12h, respectively, prior to expected humane endpoint (tumor diameter ~40 mm) or an experimental endpoint of 50-day treatment. Tumor volumes were monitored daily by caliper and quantified as Volume = $\frac{\text{length x width}^2}{2}$. Cumulative growth rate (CGR)[21] was computed over time and quantified as: CGR = $\sum_{i=0}^{f=t(\text{sacrifice})} \frac{\text{Volume final}}{\text{Volume initial}} \left(\frac{1.303}{t} - 1\right)$ x 100% as shown in Figure S5. Rat body weights were monitored twice a week to assess drug toxicity for all studies. Tumor malignancy was confirmed by H&E and an experienced rodent pathologist.

Tissue dissociation and fluorescent-activated cell sorting (FACS)

Processing of human clinical specimens

Following transfer from tissue bank to the laboratory, up to three intact pieces of tissues were preserved in formalin-fixed cassettes prior to paraffin embedding and serial sectioning by the Brigham and Women's Hospital (BWH) Pathology Core. Simultaneously, remaining tissues were minced using fine surgical scissors and scalpel and subjected to enzymatic digestion by medium containing 2 mg/mL collagenase type IV, 2 mg/mL hyaluronidase and 2 mg/mL BSA in DMEM/F12 medium, at 37°C for 60–90 min depending on tissue size. The digested tissues were filtered through 500-μm strainers, washed, and subjected to staining with Live/Dead Aqua Dye, CD45, EPCAM, and CD10 (1:100) prior to sorting via a 4-laser high-speed BD FACSAria II cell sorter. Four cellular fractions, including immune (single-positive $CD45^+$), epithelial (single-positive $EpCAM^+$), myoepithelial ($EpCAM^+CD10^+$), or stroma (all-negative) were sorted into 5mL FACS tubes containing PBS buffer supplemented with 0.04% UltraPure BSA and immediately transferred to the DFCI Translational Immunogenomics Lab (TIGL) for single-cell library construction. *Processing of rat tissues*. Following euthanasia, tumor tissues, tumor-adjacent and distant mammary glands as well as peripheral blood, spleen, and bone marrow from hind-leg femurs were collected and tumor/spleen weights were measured as previous described.[74] For tumor and mammary tissues, up to four pieces at different locations were collected into cassettes, fixed overnight in 4% formalin, stored in 70% ethanol, followed by paraffin embedding, sectioning, and hematoxylin and eosin staining by the Rodent Pathology Core of Harvard Medical School. The remaining tissue was immediately digested in digestion medium containing 2 mg/mL collagenase type IV, 2 mg/mL hyaluronidase and 2 mg/mL BSA in DMEM/F12 medium, at 37°C for 60 min (mammary glands and small tumor tissues) or 90 min (large tumor tissues), serially filtered through 500- and 100-μm strainers frozen in freezing medium (90% FBS+10% DMSO), and cryopreserved in liquid nitrogen for future usage. Bone marrow was collected by flushing the femurs and spleen was mechanically pressed through 100 μm-strainers, lysed with ACK buffer, fixed with 4% formaldehyde prior to cryopreservation in liquid nitrogen. Blood was extracted via intracardiac route using 16-cc syringe, collected into K2EDTA-coated tubes (BD Microtainer#365974), lysed for red blood cells by ACK buffer, washed twice, and immediately stained for FACS immune profiling. Similar to human tissues, tumor and mammary tissues from selected rats were for staining with Live/Dead Aqua Dye, CD45, and EpCAM for FACS and scRNA-seq library construction. For rat tissues, three cellular fractions, including immune (single-positive $CD45^+$), epithelial (single-positive $EpCAM^+$), or stroma

(double-negative) were directly sorted via BD FACSAria II into PBS buffer supplemented with 0.04% UltraPure BSA prior to single-cell library construction. All flow gating schemes can be found in Table S3.

Ex vivo induction of iTreg and co-culture with autologous DC subsets

Isolation and differentiation of autologous T cells and DCs

At the time of tissue collection, rats bearing macroscopic tumors and matched NMU-treated rats with no palpable tumors were euthanized, where tumors, all mammary glands, tumor-draining LNs, peripheral blood and bone marrow were harvested. Single-cell suspension from LNs and peripheral blood mononuclear cells (PBMCs) were plated directly onto 6-well plates pre-coated with αCD3 (1μg/mL) and αCD28 (5μg/mL) and cultured in Rat iTreg Differentiation Media containing low-dose IL-2 and TGFβ (RPMI-1640 supplemented with 10%FBS, 1%ps, 1% Glutamax, 0.05mM β-mercaptoethanol, 5 ng/mL IL-2, 1 ng/mL TGFβ, 5 μg/mL αCD28, 50 nM retinoic acid, and 100 nM rapamycin). After 48 h, an equal volume of high-dose IL-2 and TGFβ (30 ng/mL IL-2 and 5 ng/mL TGFβ) was supplemented, and cultures were maintained until day 7 for complete and uniform iTreg differentiation prior to co-cultures with autologous DCs. In parallel, moDCs were generated from bone marrow and peripheral blood of the same animals using standard GM-CSF/IL-4 supplemented DC Medium (IMDM with 10%FBS, 1%ps, 1% Glutamax. 0.05mM β-mercaptoethanol, 100 ng/mL GM-CSF, and 50 ng/mL IL-4) for 5 days. After that, DC maturation was induced by culturing cells for an additional 48 h in Maturation Medium (IMDM with 10%FBS, 1%ps, 1% Glutamax, 0.05mM β-mercaptoethanol. 10 ng/mL TNFα, 10 ng/mL IL-1β, 10 ng/mL IL-6, 1μg/mL PGE, and 25μg/mL polyI:C).

RapidSphere enrichment of cDC2 and cDC1 subsets

cDC subsets were enriched using EasySep-based positive selection for PE- and APC-conjugate markers. Single-cell suspensions from digested macroscopic tumors or microlesions were incubated with rat Fc blocks (3μg/mL) followed by staining with CD103-PE (3μg/mL, 15 min). Cells were then incubated with anti-PE reagent from the PE Positive Selection Kit II (100μL/mL, 15 min) followed by RapidSpheres.v1 (10 min) and magnetically enriched to isolate $CD103^+$ tissue DCs. Enriched $CD103^+$ cells were divided into two equal fractions and stained with either SIRPα-APC (3 μg/mL, 15 min) or XCR1-APC (3 μg/mL, 15 min). Each fraction was subsequently incubated with anti-APC reagent from the APC Positive Selection Kit II (100μL/mL, 15 min) and RapidSpheres.v2 followed by magnetic enrichment. This sequential PE/APC dual selection yielded highly purified $CD103^+$ $SIRP\alpha^+$ cDC2 and $CD103^+$ $XCR1^+$ cDC1 populations (see Figure S3A; Table S3).

Co-culture of iTreg with autologous cDCs or moDCs

On day 7 of differentiation, iTreg were labeled with CellTrace-CSFE (5μM, 1:1000, 20min at 37°C) seeded at 1×10^5 cells in 96-well plates. For immune synapse blocking experiments, iTreg were pre-incubated with equimolar mix of isotype controls (mouse IgG1 and IgG2a, 5μg/mL each) αTCRα/β, αCTLA4, and αCD4 (10μg/mL each) during CSFE labeling, while DCs were pre-incubated with equimolar isotype controls (mouse IgG1 and IgG2a, 5μg/mL each), αMHC-II (RT-1D) and αCD80 (10μg/mL each). CSFE-negative cDC1, cDC2 or moDCs derived from PBMCs or bone marrow were added at 1:1 ratio with iTreg. At baseline, 10% of iTreg and DCs were immediately fixed and stained as baseline quality control (Figures S3A and S3B). Monocultures of DCs or iTreg, as well as co-cultures of DCs and iTreg derived from dLNs or PBMCs were maintained for 5 days in the presence of isotype controls or blocking antibodies. All condition were performed in duplicates. At experimental endpoint, cells were fixed, permeabilized, stained, and analyzed by flow cytometry. CSFE dilution was used to quantify iTreg proliferation, and a Treg division index was calculated as the ratio of cells reaching division 4 or higher (D4+) to those in division 2 (D2).

Ex vivo conditioning of human and rat iTreg by IL-33

Human iTreg differentiation

Peripheral blood mononuclear cells (PBMCs) were obtained from apheresis products of six healthy donors (ATCC). Naive $CD45RA^+$ $CD25^{neg}$ $CD4^+$ and natural Treg (nTreg, $CD127^{neg}$ $CD25^+$ $CD4^+$) were enriched using Miltenyi Naive $CD4^+$ T cell Isolation Kit II (Human) and $CD4^+CD25^+CD127dim/-$ Regulatory T cell Isolation Kit II (Human), respectively. Briefly, naive $CD4^+$ isolation was performed by labeling non-$CD4^+$ T cells with Biotin-Antibody Cocktail II (10μL/10^7 cells) followed by Microbead Cocktail II (20μL/10^7 cells) and magnetic depletion using LD columns, yielding unlabeled $CD4^+$ naive cells. $CD127^{neg}$ $CD25^+$ $CD4^+$ nTreg isolation involved a two-step procedure: (1) negative selection of non-$CD4^+$ and $CD127^{hi}$ cells using Biotin-Antibody Cocktail II (10μL/10^7 cells) and Anti-Biotin Microbeads (30μL/10^7 cells) with LD column depletion; (2) positive selection for $CD4^+CD25^+CD127^{neg}$ cells using $CD25^+$ MicroBeads II (10μL per enriched sample) and two rounds of MS-column purification. For both enrichment workflows, 10% of enriched fractions, all column-depleted fractions and flowthroughs were collected for flow cytometric quality control. Remaining enriched naive $CD4^+$ or nTreg cells were stimulated with pre-cleaned Human T-Activator CD3/CD28 Dynabeads (25μL beads/10^6 T cells) and plated onto 6-well plates pre-coated with αCD3 (1μg/mL) and αCD28 (5μg/mL). Cells were cultured in Human Lymphocyte Serum-Free Medium KBM581 Media formulated either for Inducible Treg (iTreg: 10%FBS, 1%ps, 1% Glutamax, 0.05mM β-mercaptoethanol, 5 ng/mL IL-2, 1 ng/mL TGFβ, 5 μg/mL αCD28, 50 nM retinoic acid, 100 nM rapamycin) or for nTreg maintenance (10%FBS, 1%ps, 1% Glutamax, 0.05mM β-mercaptoethanol, 20 ng/mL IL-15, 30 ng/mL IL-2, 1 μg/mL αCD28, 50 nM retinoic acid, 100 nM rapamycin). For iTreg differentiation, an equal volume of high-dose IL-2/TGFβ supplement (30 ng/mL IL-2, 5 ng/mL TGFβ) was added after 48 h, and cultures were maintained for an additional ~5 days until uniform iTreg phenotype ($FOXP3^{lo/int}$ $CD25^+$ $CD4^+$) was achieved. Because nTreg yields from apheresis samples were low (~2,000–5,000 cells/donor) and insufficient for all experimental conditions, extended IL-33 conditioning experiments were performed exclusively using naive $CD4^+$-derived iTreg. Enrichment of human DC2 from human PBMCs using the Human CD1c (BDCA-1) Dendritic Cell Isolation Kit consistently yielded <1,000 cells per

donor. Moreover, subsequent differentiation of these with GM-CSF (1000 U/mL) and IL-4 (1000 U/mL) did not expand their cell numbers sufficient for co-culture setups.

Rat iTreg differentiation

$CD3^+$ T cells, PBMCs, splenocytes, and bone marrow cells from outbred SD rats were obtained from iQ Biosciences. Purified T cells and PBMCs exhibited superior viability and iTreg differentiation potential and were therefore used for rat iTreg generation. Because no commercial rat $CD4^+$ enrichment kits are available, iTreg differentiation (as described above for rat T cells) was performed directly on $CD3^+$ pan-T cells and PBMCs. iTreg populations were subsequently identified by flow cytometric gating for downstream CellTrace-based proliferation analyses.

Extended ex vivo IL-33 stimulation

Prior to IL-33 stimulation, rat iTreg and TGFβ-conditioned PBMCs were labeled with CellTrace-CSFE (5μM, 1:1000, 20min at 37°C). Human iTreg were not CSFE-labeled due to high sensitivity to the dye at concentration required for long-term tracking. On day 7 of differentiation, CFSE-labeled rat iTreg were plated onto αCD3/αCD28-coated plates (1μg/mL and 5μg/mL, respectively) and cultured in TGFβ-free, IL2-free, serum-free RPMI medium in the presence of escalating doses of recombinant rat IL-33 (0.1, 1, 5, 25, 50, 100ng/mL), rat IgG1, or no cytokine for additional 7 days. Human iTreg were plated in TGFβ-free, IL2-free, serum-free KBM581 medium and stimulated with escalating doses of recombinant human IL-33 (0.1, 1, 5, 25, 50, 100ng/mL), with/without IL-33 blockade using Tozorakimab (αIL-33 mAb, 3.54 ng/mL or 25.2μM) or Astegolimab (αST2 mAb, 8.56 ng/mL or 59μM) for additional 5 days. Corresponding human IgG1λ2 and IgG2κ isotype controls were included at matched molar concentrations as isotype controls for Tozorakimab and Astegolimab, respectively. To ensure constant exposure of newly divided iTreg to IL-33, recombinant IL-33 and blocking antibodies were replenished every 72 h. At experimental endpoints (day 5 for human iTreg; day 7 for rat iTreg), cells were pre-treated with Brefeldin A (5μg/mL, 4 h, 37°C), fixed, permeabilized, and stained for flow-cytometric assessment of cytokine profiles (human) or CSFE dilution (rat).

Histology evaluation

Formalin-fixed tissues were submitted for processing at the Rodent Pathology Core of Harvard Medical School and the BWH Pathology Core. Briefly, FFPE sections were deparaffinized and stained with hematoxylin and eosin (H&E) followed standard protocol previously described. Histology of malignant vs. normal mammary tissues in SD rats was determined by an experienced rodent pathologist at the facility. H&E slides were then imaged using the Olympus VS120 Virtual Slide Microscope and scanned using Nikon Eclipse Ti2 in Nikon NIS Element AR software. Representative histology of rat mammary glands and tumors can be found in Table S3.

Immunofluorescence, wide-field scanning, and confocal microscopy

Immunostaining

For both human and rat specimens, histology and multicolor immunofluorescence were performed on 5-μm sections of FFPE tissues as previously described. Briefly, tissue sections were pre-incubated overnight at 60°C, deparaffinized in xylene and serial EtOH immersion, and antigen retrieval was performed using Target Retrieval Solution, pH9 (Dako) for 60 min in an in-house steamer. Slides were cooled to room temperature (RT), permeabilized with 0.25–0.5% Triton for 5 min, and blocked for 30 min with normal goat serum solution (NGS10% in 2% BSA). Incubation with primary antibodies (CD3, 1:100 dilution in 10%NGS; FOXP3, 1:100; Ki67, 1:600, EPCAM, 1:100; SMA, 1:400; ER, 1:100, CD163, 1:100, GSN, 1:100; CD34, 1:100; CD8A, 1:100) were performed overnight at 4°C in a humidified chamber. After washing in Tris-Buffered Saline (TBS)-Tween, fluorophore-conjugated secondary antibodies (1:100 dilution in 10%NGS) were applied for 1 h at RT followed by serial TBS-Tween washing. To allow multiplexing of two rat and two rabbit IgG antibodies in 5-plex staining procedure, conjugated rabbit Ki67-AlexaFluor488 were applied at this step (2 h, RT). Slides were counterstained with Hoechst for 15 min and mounted with VECTASHIELD Vibrance Antifade Mounting Medium (Vector Laboratories).

Wide-field microscopy

All imaging procedures in this study were performed at the DFCI Molecular Imaging Core. The fluorescence images shown in the paper were scanned at 10X using a high-speed wide-field THUNDER Leica Imager with an HC PL FLUOTAR 10x/0.32 objective and DFT5 for DAPI/FITC/TRITC/Cy5 detector operated in Leica LAS X Software. For each slide, the entire tumor and stroma region were visualized fluorescently under 'Spiral' option, demarcated, tile-adjusted for z-step with best-fitted focal plane membranous CD3 signal, and scanned at specified x, y, z coordinates under four excitation wavelengths of 405nm, 488nm, 555nm, and 647nm. Following adaptive tile stitching, Integrated Computational Clearing (ICC) algorithm was applied across all tiles to eliminate out-of-focus interfering signals and render shade correction to generate near-confocal resolution.

Confocal microscopy

Selected tumors from patients and rats were further imaged using a Zeiss 980 Confocal System (LSM980 model) equipped with solid-state diode lasers with laser lines for 405nm, 445nm, 514nm, 561nm, 594nm, 639nm, and 750nm. All confocal imaging was assisted by the Zeiss Airyscan-2 detector that enables up to 90nm-resolution and high-speed confocal scanning. For 5-color imaging of fibroblast and cycTreg, the options for 405nm, 514nm, 561nm, 594nm, and 639nm wavelength were selected. For 7-color imaging of cDC2 and cycTreg, all 7 colors were used. *Airyscan* was performed with a Z-piezo scanning stage for tissue scanning at confocal resolution in a 3 × 5 tile dimension with a 0.5μm z-step (5 steps for tile) using a 25x- or 63×-oil-immersion objective (1.4 numerical aperture). The captured images underwent AiryScan Processing in a ZEISS ZEN.3.7 Blue operating software and processed with Stitching, z stack Projection, and ROI in a ZEN Desk software. For all multiplexed confocal images, linear spectral unmixing was performed based on positive fluorescence from each channel to minimize leaking signals.

Please cite this article in press as: Bui et al., Identification of cycling regulatory T cell precursors as conductors of immune escape during breast carcinoma progression, Cancer Cell (2026), https://doi.org/10.1016/j.ccell.2026.03.015

Image quantification

All image analyses were performed in QuPath. DCIS/IBC tumor regions and the surrounding regions were manually selected to comprise where $CD3^+$ existed. The number of total $CD3^+$, $FOXP3^+CD3^+$ Treg, $Ki67^+FOXP3^+CD3^+$ cycTreg, conventional T cells, $CLEC10^+$ cDC2, $CD103^+$ tissue DCs, and total $Hoechst^+$ nuclei were counted by automated cell counter under a Random Forest algorithm. For quantification, QuPath-generated counts of T cells or cDC2 were normalized to the total number of nuclei detected (%-total cells) or alternatively to the analyzed areas (cells/mm^2).

High-dimensional immune profiling by flow cytometry

Tissues from SD rats were harvested, processed, and cryopreserved in liquid nitrogen as described above. *Immune profiling.* Single-cell suspension was cryo-recovered quickly in water bath at 37°C, washed with FACS buffer (0.5%BSA, 4mM EDTA, 0.1% Azide, 1% FBS), stained with Live/Dead Aqua dye (1:400) and Fc-blocked with anti-rat CD32 (clone D34-485, 1:200, 20 min, 4°C) prior to 1-h staining with the panel-tailored fluorophore-conjugated surface markers: CD3ε-FITC (1:50), TCRα/β-APC (1:100), CD45-PEcy.7 (1:100), CD4-APC.cy7 (1:100), CD8α-BV711 (1:100), CD45RA-PerCP.cy5.5 (1:100), CD45RC-BV786 (1:100), CD25-BV650 (1:100), ICOS-BV605 (1:100), CD134/OX40 (1:100), CTLA4-PE (1:100), CD103-BV605 (1:100), SIRPα-APC (1:100), SIRPα-BV786 (1:100), RT1B-BV650 (1:100), RT1A-BV711, CD86-BV786 (1:100), CD11b/c-BV421 (1:100), CD11b/c-BV750 (1:100), XCR1-APC.cy7 (1:100), CD44-BV750 (1:100). For non-conjugated surface antibodies, including SMA (1:200), IL-33 (1:100), CD137/4-1BB (1:100), LAG3 (1:100), and PD-1 (1:200), primary antibody staining was followed by staining with secondary antibodies (1:400, 30 min). After surface marker staining, cells were washed with FACS buffer and fixed at RT with the Perm/Fix solution (1:4 with Fix Diluent) from the TrueNuclear Permeabilization Kit (BioLegend) and serially washed and permeabilized with the Perm/Wash solution (1:10 dilution). Nuclear factor and cytokine staining with FOXP3-eFluor450 (1:100), FOXP3-PE (1:100), FOXP3-PerCPcy5.5 (1:100), EOMES-PE (1:100), Helios-AF647 (1:100), IRF4-AF700 (1:100), IRF8-BV421 (1:100), Ki67 (clone SP6, 1:100), IL-10 (1:100), and IL-33 (1:200), was performed overnight at 4°C, followed by serial washing with Perm/Wash solution and secondary anti-rabbit antibody staining for Ki67 (clone SP6). The stained cell suspension was filtered in 5mL FACS tubes and analyzed by a 4-laser and 17-parameter BD LSR Fortessa Cell Analyzer following spectral overlap compensation based on single-color controls. Fluorescence-Minus-One (FMO) controls were prepared as gating control for positive and negative signals. FlowJo (Becton Dickinson, version 10.8.2) was used for analysis and population graphing and GraphPad Prism was used for quantification graphing and statistical analysis. FlowJo v10 Plugins including FlowAI, Downsample, Phenograph, UMAP, and ClusterExplorer were used for quality control, high-dimensional grouping and unbiased cluster generation of T cells and myeloid cells in rat tumors and across tissues.

BrdU staining and EdU-Click reactions

EdU and BrdU were used to evaluate frequency of S-phase cycling cells and the transition of cycling status among Treg population. Samples used for EdU/BrdU detection were carried out and analyzed in a separate panel. Similar Fc blocking, viability and surface marker staining steps were performed, except for the use of antibodies conjugated to PE and PE-related tandem dye (PE.cy7) prior to the Click reaction. Stained cells were similarly fixed and permeabilized using the TrueNuclear Permeabilization Kit (BioLegend). An additional step of DNase I treatment at 0.02U was performed to allow liberation of BrdU epitope (20 min, 37°C). Staining of nuclear factors including BrdU (1:50) was performed overnight at 4°C, followed by serial washing with Perm/Wash solution and secondary anti-rabbit antibody staining for Ki67. A working solution of Click reaction was prepared by mixing stepwise solutions of $CuSO_4$, Azide-647, and sodium ascorbate in TBS buffer. Cells were stained in Click solution for 7min at RT, washed with Perm/Wash buffer, and stained with PE or PE.cy7-conjugated antibodies prior to analysis on BD LSR Fortessa Cell Analyzer. Antibodies used in flow cytometry were listed in key resources table.

scRNA-seq library construction, illumina sequencing, and 10X cell ranger outputs

For scRNA-Seq analysis, samples from tumor and mammary gland tissues were prepared either freshly from FACS enrichment of cellular fractions (Datasets 1 and 2) or after recovery of cryopreserved cell suspension of immunotherapy-treated rat tumors (Dataset 3) or time-course macroscopic tumors/microlesions (Dataset 5). Briefly, cell suspension was counted for viable cells and diluted at a concentration of 1000 cells/μL in at least 40μL of PBS solution with 0.04% UltraPure BSA (Sigma Alrich), accounting for a loading of 5000-10,000 cells onto the 10X Genomics Chromium Single-Cell Chip in the presence of reverse transcription mix and single-cell 3′ or 5′ gel bead-in-emulsion (GEM). Specific to FACS-enriched cells from Dataset 1 (human DCIS/IBC) or Dataset 2 (rat MG/Tumor), cell and library preparation was carried out according to the 10X Chromium NEXT GEM Single Cell 3′ HT v3 protocol (10X Genomics) targeting 5000 cells per sample. Specific to cells from Dataset 3 (immunotherapy-treated rats) and Dataset 5 (time-course macro/microlesions), cell and library preparation was carried out according to the 10X Chromium NEXT GEM Single Cell 5′ HT v2 protocol (10X Genomics) targeting 10000 cells per sample. The quality of amplified cDNA libraries was assessed using the BioAnalyzer High Sensitivity DNA Kit (Agilent) on an Agilent Bioanalyzer. Libraries with equivalent molar ratio were sequenced on an Illumina NovaSeq 6000 at the DFCI Molecular Biology Core targeting ~25,000 reads per cells. The raw sequenced reads were aligned to either the human reference genome hg18 (Dataset 1) or the rat reference genome Rnor_6 (Rn6, Datasets 2, 3, and 5) via the 10X Genomics Cell Ranger 7.0.1 (https://www.10xgenomics.com/), processed with *bcltofastq* to generate FASTQ files, demultiplexed and group-aggregated via Cell Ranger Aggr. v7.0.1 on 10X Cloud (https://cloud.10xgenomics.com/), excluding the option to include *intron*. The resulting filtered count-matrix files with assigned barcodes and gene features were downloaded and imported into R 4.4.0 for more stringent quality-control and downstream analysis using R package *Seurat* (v5.1.0). Package version, R environment, and base dependencies are listed in **Supplementary Methods**.

scRNA-seq data processing pipelines

Low quality reads were removed out after data filtering under stringent quality-control parameter: 2,000 < nCount <60,000 & percent.mt < 25 & percent.ribo <40. Cell doublets were identified and removed using DoubletFinder R package v2.0.4. Within the DFCI dataset, all cellular fractions including immune, (myo)epithelial, and stroma of Datasets 1 and 2 were combined using merge() prior to normalization by SCTransform().

Multi-cohort integration and batch correction

For integration of our scRNA-seq data with three published datasets,[8–10] all cells across conditions were merged and subsequently integrated with Harmony package v1.2.0 (https://github.com/immunogenomics/harmony) using RunHarmony() with 'Batch' as the main variant regressor. The integrated dataset was then decomposed into a standard 30-dimension PCA before Louvain clustering and dimensional reduction by UMAP under Louvain algorithm with a 0.2 resolution. Subclusters of immune, epithelial, stroma and subsequent T cells, myeloid, and fibroblast clusters were analyzed with greater resolution by sub-setting based on cell identities and re-clustering at the same 1:30 dimension with an increased resolution (0.4–0.5 for Seurat-based, and 0.8 for Monocle3-based analysis). FindMarkers() under the default Wilcoxon rank-sum statistical test was used to compute differentially expressed genes (DEGs) specific for each Seurat cluster, which were curated manually with adjusted p values < 0.05, 0.7<$\log_2$ fold change (LFC) < 1.5 and pct.1 > 0.5 & pct.2 < 0.1 cutoffs. Library-based methods of annotation using Cell Typist (celltypist 1.1.0 Python package) and the Human Primary Cell Atlast (SingleR R package) platforms were performed in parallel. The R package scCustomize v2.1.2 (https://github.com/samuel-marsh/scCustomize) was used for stylistic visualization of Seurat plots. DEGs used to annotate Seurat cell type clusters, DEGs between histology conditions (FDR<0.05), or pseudotime DEGs (FDR<0.01) are listed in Table S1 (human) and S2 (rat).

Gene module scoring and ProjecTILs

For in-depth annotation of T cells, myeloid, and fibroblast clusters, gene modules reported in 14 studies related to breast cancers and pan-cancers were applied using *AddModuleScore()* to identify well-documented or novel cell states. All gene modules used in this study are listed together with relevant ref.[14,26,27,45,75–85] in Table S3. In addition, the human and rat T cell datasets 1–2 were projected onto a reference T cell atlas using the *ProjecTILs* R package v3.1.0[14] https://github.com/carmonalab/ProjecTILs) to estimate the proportion of six major T cell states (effector, Treg, exhausted and progenitor exhausted) and their fluctuations among breast cancer conditions.

MILO neighborhood and differential abundance testing

To calculate the differential abundances (DA) of cell states across experimental conditions, Milo neighborhood analysis[12] (*miloR* R package v2.0.0, https://github.com/MarioniLab/miloR) was performed to minimize forced Seurat clustering under Louvain method, thus considering data point continuity within a flexible k-nearest neighbor (KNN) and generalized linearized model (GLM) framework. To construct a Milo KNN graph, cells with unique identifiers were scaled by sequencing depth, log transformed, and their expression matrices were projected onto major principal components using *buildGraph()* with k = 30 and d = 30 as parameters. Cell neighborhoods and neighboring connectivity were constructed using a sum of neighborhood indices and their connections to individual KNN graph edges, creating a 'Neighborhood x Sample' matrix using *makeNhoods(), buildNhoodGraph(),* and *calcNhoodDistance()* functions assuming proportion = 0.1. To assess DA of neighborhoods across conditions, a quasi-likelihood (QL) F-statistics method with trimmed mean of M-values (TMM) normalization was implemented from *edgeR* and *Cydar* and applied along with *annotateNhood()* to contrast cell counts and compute corresponding p value of each cell neighborhood. A weighted Benjamini-Hochberg method was applied to adjust for p values based on the reciprocal of the neighborhood connectivity. In KNN graph, each node represents neighborhoods where its size represents the cell numbers within each hood. The edges represent the common number of cells overlapping among neighborhoods. The coordinates of the nodes are determined by the indexed single cells distributed on the UMAP cell embedding. To determine neighborhood homogeneity, DA between two compared conditions was calculated, and neighborhoods with a unique cell fraction <70% was considered as 'Mixed'. The distribution of DA fold-change of each neighbor, significantly skewed toward either condition, can then be plotted as beeswarm plots using *plotDAbeeswarm()*. *FindNhoodGroupMarkers()* was used to extract neighborhood DA expression markers, from which the neighborhood identities could be derived.

Monocle3 pseudotime inference

Monocle3 (v1.3.7)[17] was performed to organize cells into discontinued trajectories with statistical testing to identify gene expression variations over these trajectories (https://cole-trapnell-lab.github.io/monocle3). The well-annotated datasets of individual cell types were converted into cell dataset (CDS) format and projected via *reduce_dimension()*. DEGs were computed by KNN *graph_test* (k = 20) with Moran's I statistics >0.01 and q value < 0.05, and cells were then re-clustered as partitions to enable separate trajectories. Cell communities within each partition were set to learn a trajectory graph via *learn_graph()*, where cells were ordered onto a cell-wise pseudotime constructed based on each cell's Euclidean distance to its nearest principal point ψ within the embedding UMAP. Given ψ distances and an algorithm-selected root derived from *principal_graph_aux()*, each cell can be assigned with a pseudotime value via *order_cells()*. For pseudotime computation in this study, roots were always specified within the non-cancer or isotype-treated experimental conditions, and the later pseudotime bins were inferred as derivative trajectory nodes originating from these root states. Branch points were decision-making nodes where a trajectory was separated into two or more ψ values leading to distinct cell states or partitions known as branch leaves. Genes differentially expressed over different pseudotime values, or pseudotime genes, were identified by Moran's I auto-correlation test which accounts for the spatial relationships among data points within a weighted KNN graph. Regression coefficients under a Moran's residual model were computed to identify co-regulated gene modules for each pseudotime region (early, mid, late) and plotted via *plot_genes_in_pseudotime()*.

Please cite this article in press as: Bui et al., Identification of cycling regulatory T cell precursors as conductors of immune escape during breast carcinoma progression, Cancer Cell (2026), https://doi.org/10.1016/j.ccell.2026.03.015

High dimensional weighted-gene co-expression network analysis (hdWGCNA)

The R package *hdWGCNA* (v0.3.03) employs bootstrapped, sparsity-based expression matrix to building metacell data construction and compute weighted co-expression networks from aggregated single-cell expression profiles of our scRNA-Seq datasets. Co-expression network was analyzed for human and rat cycling/non-cycling Treg as well as other T cell types using standard *hdWGCNA* pipeline. Specifically, the metacells for Treg clusters were constructed on integrated T cell dataset for each cell type cluster using aggregate function *MetacellsbyGroups()* with the maximum number of 10 shared cells between a pair of metacell at k-nearest neighbor distance of 25. Soft-power was calculated by *TestSoftPowers()* under 'signed' network type to determine the numbers of co-expression via correlation under β power, specified for each module for a given Seurat cluster or experimental condition. Following data scaling and regression by *ScaleData()*, hdWGCNA framework assigned Module Eigengenes (MEs) via *ConstructNetwork()*, *Module Eigengenes()*, and *ModuleConnectivity()* to discretize, summarize, and visualize co-expression of genes by eigene values within a given module. A correlation threshold of 0.2 is set for a module specified by minimal size of 100 genes where intramodular genes are defined using kME connectivity parameter. Any module with >0.8 correlation is merged to avoid excessive module generation. Harmony algorithm is used by default for batch-correction of ME values. To represent co-expression relationship within each gene module, gene network visualization was performed using *ModuleNetworkPlot()*, where top network genes were placed in the center and remaining supporting network nodes were outlined as outer circle. To show gene nodes across all gene modules, the numbers of edges were reduced to keep only the top 10% strongest connections and displayed as interconnected frames colored by individual gene modules. Gene Ontology list from EnrichR website (version 2023) was further loaded via *fgsea* package to illustratate gene nodes involved in specific immune response and T cell pathways. Stepwise instruction can be found at: https://smorabit.github.io/hdWGCNA/articles/basic_tutorial.html.

Single-sample GSEA

Gene set enrichment analysis (GSEA) at single cell levels was performed by R package *escape*[86] (v2.0.0, https://github.com/ncborcherding/escape) with access to the Molecular Signature Database (MsigDB). The GSEA reference used in this paper was derived from the MsigDB Hallmark library via getGeneSets(library = "H"). The enrichment step was performed under ssGSEA method (Barbie et al. 2009) via *escape.matrix()* and *runEscape()* directly from the scRNA count matrix, using sets of 2000 cells and run 4 times with parallel calculation via SnowParam back-end (workers = 4, tasks = 100). The ssGSEA scores for 50 hallmark gene sets were estimated, ranked, and returned onto the Seurat objects via *AddMetaData().* The R package *dittoSeq* was used as a primary source for graph visualization of GSEA outputs. For human dataset, all 50 Hallmarks or "Interferon Gamma and Alpha Response" were constructed as Geyser plot and/or row-scaled enrichment heatmap using *geyserEnrichment()* and *heatmapEnrichment()* with either progression stage or cell clusters as variables. For rat immunotherapy study, the "*Allograft Rejection*" hallmark gene set was plotted as ridge plots using *ridgeEnrichment()* to incorporate categorical variables such as treatment response or cell subtypes for the visualization of enrichment score distribution with higher granularity. Statistical significance of enrichment scores between variable groups such as treatment response was computed via *getSignificance()* under ANOVA fit model and returned as FDR values following Bonferroni's correction.

CellChat intercellular communication

Cell state-specific communications were assessed based on ligand-receptor respective expression on sender and receiver cells using the later version of the R package *CellChat*[69] v2.1.2 (https://github.com/jinworks/CellChat) with an updated library of >3,300 validated Ligand-Receptor pairs consisting of 229 signaling pathways. Prior to *CellChat* pipeline, a master Seurat object annotated for identities of all subtype cell states (T cells, myeloid, cancer epithelium, fibroblasts) was constructed by recalling and joining the unique cell idents with annotated identities from each sub-clustered Seurat object. To avoid confounding signals, sub-clusters with <100 cells, including B cells, endothelial cells, certain subsets of myeloid and cancer cells, were not included in *CellChat* analysis. To compare immunotherapy treatment groups with different cell type compositions, *CellChat* was set to 'lift up' cell groups with similar cell labels using *liftCellChat().* The *CellChat* objects of all treatment-response groups from rat tumors were processed separately to identify enriched genes and interactions using Wilcoxon rank-sum test ($p < 0.05$) via the functions *identifiyOverExpressedGenes()* and *identifiyOverExpressedInteractions()*, compute communication probabilities by 'triMean' method via *computeCommnProb()* and infer probable communication pathways by summation of all associated Ligand-Receptor pairs. All processed *CellChat* objects with lifted numbers of cell types were combined via *mergeCellChat()*. Differential cell-cell interactomes between two conditions were computed using permutation test (100 permutations by default). Outgoing and incoming patterns based on Ligand-Receptor pairs sent or received by each cell states were computed as summation of all weighted communication probabilities. Prioritized pathways altered between two conditions were ranked by *rankNet()*. All interactome analyses by *CellChat* were shown as average strength of interaction weighted by total cell numbers within a cell type and visualized by chord diagrams, circle plots, or heatmaps supported by *circlize* (v0.4.16), *igraph* (v2.0.3), and *ComplexHeatmap* (v2.20.0) dependencies.

10X visium spatial transcriptomic processing and data analysis

Spatial transcriptomics was prepared and processed by the Hope Babette Tang Histology Facility at the Koch Institute for Integrative Cancer Research at MIT. Snap frozen samples from rat mammary glands and tumors were cryosectioned at 10μm thickness onto 10X Genomics Spatial Gene Expression slides (Visium Gene Expression Slide & Reagents Kit cat#1000187, Pleasanton, CA), using the demonstrated protocol "Methanol Fixation, H&E staining &Imaging for Visium Spatial Protocols" (CG000160) and user guide "Visium Spatial Gene Expression Reagent Kits" (CG000239). These steps were optimized according to the "Visium Spatial Tissue Optimization Slide and Reagent Kit" (#PN-1000193) and "Visium Spatial Gene Expression Reagent Kit-Optimization Guide"

(CG000238). Briefly, the middle sections with the best morphology were fixed and permeabilized for 30 min using standard protocol and processed via the 10X Visium Spatial Gene Expression Reagent Kits (Dual-Index Kit TT, PN-1000184). The sections were mounted onto eight 6.5 mm × 6.5 mm capture areas surrounding by 8 mm × 8 mm fiducial frame, enabling at least 2000 × 2000 pixel portion total and ~5000 gene expression per spot. Image for each sample was captured on a brightfield Zeiss Axio microscope, and these images were used later to map gene expression patterns back onto tissues. Afterward, more permeabilization was performed and capturing was enabled by 30nt poly(dT) probes in the presence of nucleotides, spatial barcodes, and 12nt UMIs as 'Read 1'. Reverse transcription was allowed to occur *in situ* on the slide followed by template-switching Oligo via the Second Strand Mix and cDNA was amplified together with the spatial barcodes. Visium spatial library construction was initiated following enzymatic fragmentation and end-repair with P5 and P7 sample indices and TruSeq 'Read 2', enabling Illumina sequencing via HiSeq4000. The sequenced reads were processed via the 10X Space Ranger to obtain FASTQ files. The sequences were aligned to the rat reference genome Rn6 to generate gene expression counts using the default settings to generate Dataset 4. Expression level of the rat coding genes was quantified in Space Ranger. Downstream analyses including cell filtering, integration, clustering and UMAP were performed in R. Briefly, samples were individually filtered for percent.Hb and percent.mito and mapped with spatial information. For integrated analysis, samples were integrated and regressed by *SCTransform(…, assay = "Spatial")* prior to PCA and neighbor clustering at 0.8 resolution. DEGs were calculated using FindAllMarkers() and spatial clusters were annotated by most prevalent DEG markers. Module scores were added, visualized per sample, and quantified by ggplot2 across all samples. All Visium expression spots and mapping can be found in Table S3.

Public RNA-seq and proteomic analyses

TCGA

RNA-seq data and clinical information from TCGA[16] were obtained from GDC data portal and ER+, ER-/HER2+ and TNBC were defined based on IHC data. Tumor and stromal portion deconvolution were conducted using *ISOpureR* package.[87] Briefly, normalized tumor and normal mRNA abundance profiles in TPM format were used as inputs. Patient profile estimation mode was utilized to predict the mRNA abundances in tumor and stromal portions for each individual patient. Quality validation was done by unsupervised clustering and segregation of tumor, but not stromal components based on PAM50 subtypes was confirmed. Only the deconvoluted non-tumor portion transcriptomic data were used for downstream immune signature analysis. Immune infiltration score of TCGA samples were pre-calculated using *ESTIMATE* R package,[88] based on normalized gene expression in Log2 (TPM+1) format from whole tumors. "Illumina" mode was selected for the platform option. TCGA biospecimen immune profile data including pathological lymphocyte counts were downloaded from published dataset[56] (n = 4,759 TCGA patients across 13 cancer types; n = 992 breast cancer patients). For estimation of Tumor Mutational Burden (TMB), mutation annotation files from 982 patients were downloaded from FireBrowse and mutation subtypes were summarized using "maftool" package (Version 2.6.0). Mutation subtypes were classified into truncated (nonsense, frameshift deletion, frameshift insertion, splice-site) and non-truncated mutations (missense, in-frame deletion, in-frame insertion, nonstop). TMB was calculated as 2× Truncating mutation numbers + non-truncating mutation numbers.

HTAN-RAHBT

RNA-seq raw read counts matrix of RAHBT DCIS dataset was obtained from published HTAN bulk RNA-seq dataset.[18] Briefly, the stroma transcriptomic data from 196 samples after laser capture microdissection was used for downstream analysis. Only 165 DCIS patients out of 196 laser-micro-dissected patients were included in the gene module analysis. We excluded 31 patients without DCIS grade information. The specimens were graded as grade 1–3 with differential recurrence status (Yes/No) (grade 1, No: n = 22; Yes: n = 7; grade 2, No: n = 42, Yes = 25; grade 3: No = 53, Yes = 16). The gene-level counts from all studies were then normalized using TMM with *edgeR*.[73] Log2 transformed TMM-normalized counts per million [log2(TMM-CPM +1)] were used for analysis. For immune signature analysis in TCGA and RAHBT cohorts, enrichment level of each signature was scored using *GSVA* R package.[72] Individual signatures can be found in Table S3. Ratios of cycling to non-cycling Treg was referred by the delta value of GSVA scores of cycling to non-cycling Treg.

METABRIC

For the imaging mass cytometry data analysis, cell level raw quantification files were downloaded from published dataset.[19] To define cycTreg, we used Ki67 intensity in the pre-defined "Ki67+ epithelial cells" as a reference. CycTreg was defined if a given Treg (defined in original study) harboring Ki67 signaling intensity higher the median level of $Ki67^+$ epithelial cells. t-SNE plot was used to cluster all Tregs using the "Rtsne" R package. $CD8^+$ T cell ratio was calculated using $CD8^+$ T cell number dividing to total T cell number from the imaging mass cytometry quantification. Survival analysis was performed using Cox proportional hazards regression models using *survminer* package and censored to 9,000 days.

MIBI

This multiplexed imaging dataset was obtained as part of the HTAN retrospective cohort from the RABHT study,[18] which includes 70 patients with median age of diagnosis at 54-year-old collected from 1987 to 2017. Out of 58 patients, 44 had recurrence status classified as non-progressors and the remaining 14 as progressors with median time to recurrent event of 9.1 years. All IBC recurrences in the MIBI cohort were ipsilateral events. The average follow-up period for future events was 132 months. Clinical information and cohort composition of RABHT and MIBI cohorts were previously published.[18,32] The analyses in the current study focused on DCIS patients with recurrence status (non-progressors, n = 44; progressors, n = 14) already analyzed across 433 parameters quantified by 37-plex MIBI and random forest classifiers. The single-cell phenotyping matrix and patient information were downloaded

from the original paper,[32] integrated, and analyzed using R package *ggplot2*. Five major cell lineages were defined by a number of markers, including epithelial cells (PanCK+, ECAD+, $CD45^{-}$, $CK7^{+/-}$, $VIM^{+/-}$), myoepithelial cells (SMA+, $CD45^{-}$, $PanCK^{+/-}$, $ECAD^{+/-}$, $CK5^{+/-}$, $VIM^{+/-}$), CAFs (VIM+, PanCK-, ECAD-, CK7-, $CD45^{-}$, $SMA^{+/-}$, $FAP^{+/-}$, $CD36^{+/-}$), endothelial cells ($CD31^{+}$, VIM+, PanCK-, ECAD-, CK7-, $CD45^{-}$, $SMA^{+/-}$), and immune cells ($CD45^{+}$, PanCK-, ECAD-). The proximity scores were reported as spatial enrichment scores and quantified by described methods.[89,90] Pearson's linear regression was performed with recurrence status 'Diagnostic_Group' (non-progressors/non-recurrence vs. progressors/IBC recurrence) and cancer subtypes 'SUBTYPE' as covariates using values of 'Epiedge_'celltype'_distance' as independent and dependent variables. Spatial information of immune cells and CAFs was assess relative to the DCIS epithelium edge as spatial enrichment scores. Higher enrichment values indicate higher average numbers of cells closer the epithelium with a value of 1 representing all cells localized to the epithelial edge.

QUANTIFICATION AND STATISTICAL ANALYSIS

Statistical analyses

Normal distribution was first determined by Shapiro-Wilk test and normally distributed data were subjected to non-paired, two-sided Student's *t* test (2-sample) or one-way ANOVA ($\geq$3-sample). Otherwise, non-parametric options including Mann-Whitney (2-sample) or Kruskal-Wallis ($\geq$3-sample) tests will be used to compute *p* values. Grouped comparisons for greater than 2 conditions were conducted in two-way ANOVA test and/or Mixed Model assuming potential interaction between covariate terms. For contingency calculation, Fisher's exact test was used to assess direct outcome differences between two conditions, whereas chi-square test was applied for greater than 2 conditions. To consider direct linear relationship between two variables, a simple linear regression with Pearson's correlation coefficient R was performed, and linear correlation is assumed when $R > 0.4$ and $p < 0.05$. To consider multiple covariates during patient IF analyses or immune profiling, multi-covariate linear regression models were performed under single- or two-factor effects to compute individual and combined covariate term interactions in predicting the dependent immune or tumor outcomes via F's statistics with *p* values < 0.05. Simple logistic regression was performed to predict binary outcome and the log likelihood ratio of an event happening. Since statistical tests were performed with low numbers of parameter testing, FDR-corrected for multiple hypotheses were not computed. Unless otherwise stated, statistical tests were performed in GraphPad Prism v.10 considering 95% confidence intervals and were presented as means ± SEM with an α threshold of 0.05.